Dissertation

submitted to the

Combined Faculties of the Natural Sciences and Mathematics

of the Ruperto-Carola-University of Heidelberg. Germany

for the degree of

Doctor of Natural Sciences

Put forward by

Karl Simon Alexander Hansson

born in: Eksjö, Sweden

Oral examination: February 3, 2012

The dependence of present-day galaxy properties on environment and mass

Referees: Dr. T. Lisker   Examiners: Prof. Dr. Eva K. Grebel
     Prof. Dr. Cornelis P. Dullemond   Prof. Dr. Ulrich Platt

Abstract

In this thesis I show that only some of the commonly used stellar populations models can account for observed broad-band colors of the local galaxy population. Through a stellar population synthesis modeling, including the effects of dust, I show that a galaxy's star formation history, stellar mass, chemical enrichment and dust extinction can be constrained over a large part of the parameter space using optical broad band photometry. An essentially volume complete sample of nearby ($\leq$50Mpc) galaxies in the Sloan Digital Sky Survey are selected and u,g,r,i,z-band photometry for these galaxies are measured from the survey images. Using my stellar population synthesis modeling I obtain the aforementioned properties and study how these, along with galaxy sizes and shapes, depend on galaxy stellar mass and environment. In addition, these galaxy properties are related to the mass functions of galaxy groups providing further insight into galaxy assembly. Moreover, I have performed an imaging study of the Abell 569 cluster core revealing signs of galaxy interactions as well as a galaxy luminosity function with a flat faint end slope.

Zusammenfassung

In dieser Doktorarbeit zeige ich, dass nur einige der am häufigsten genutzten Modelle stellarer Populationen die beobachteten Breitbandfarben lokaler Galaxiepopulationen reproduzieren können. Mittels eines Synthesemodells für stellare Populationen, einschließlich der Wirkung von Staub, zeige ich, dass die Sternbildungsgeschichte, die stellare Masse, die chemische Entwicklung und die Staubextinktion einer Galaxie über einen Großteil des Parameterbereichs bestimmt werden können, indem optische Breitband-Photometrie angewandt wird. Ein vollständiger Datensatz benachbarter Galaxien ($\leq$50 Mpc) aus dem Sloan Digital Sky Survey wurde ausgewählt und die u,g,r,i,z Photometrie dieser Galaxien wurde von dessen Aufnahmen gemessen. Indem wir das Synthesemodell für stellare Populationen nutzen, erhalten wir die oben erwähnten Eigenschaften und untersuchen, wie diese, ebenso wie die Größe und Form der Galaxien, abhängig von der stellaren Masse und der Umgebung der Galaxien sind. Ferner stehen diese Galaxieneigenschaften in Bezug zu den Massenfunktionen von Galaxiengruppen und liefern einen tieferen Einblick in den Galaxienaufbau. Darüberhinaus wurde eine auf optischen Bilddaten basierende Studie des Zentralbereichs des Abell 569 Galaxienhaufens durchgeführt, die Zeichen von Galaxienwechselwirkungen ebenso wie eine flache Leuchtkraftfunktion der Galaxien am leuchtschwachen Ende erkennen lässt.

Declaration

This thesis contains no material that has been accepted for the award of any other degree or diploma.

_____

Karl Simon Alexander Hansson

Contents

Chapter 1   Introduction

The scope of this chapter is twofold. First it should give the reader a general overview of the very active research topic usually referred to as galaxy formation and evolution. The text is meant to put the thesis into a broader context. Moreover, the chapter is intended to introduce a few concepts needed for being able to fully comprehend the following chapters.

1.1   Galaxies, what are those?

Galaxies are often illustrated as pretty pictures you every once in a while stumble upon in a newspaper. Moving on the sky in a similar manner as stars do, but exhibiting a great variety of morphologies and colors, galaxies have long fascinated people. So what are these intriguing objects? According to a dictionary[1] a galaxy is *"a large system of stars held together by mutual gravitation and isolated from similar systems by vast regions of space."*. It is worth adding two comments regarding this definition. First, stars are usually not the only constituent of galaxies. Dark matter is thought to be the dominant component in terms of mass for most galaxies. Many galaxies also contain large amounts of gas appearing in a variety of phases. Massive galaxies have some hot and ionized gas (Kereš et al., 2005) while star forming galaxies also have considerable amounts of the neutral gas (Walter et al., 2008) and molecular gas at even higher densities, reflecting the correlation between gas surface density and star formation rate (Kennicutt, 1998). Dust, even though it contributes only very little to mass, is another important component of galaxies, responsible for altering their appearance by scattering and absorption of optical radiation. Galaxies spans a vast range in stellar mass[2] from $10^3 M_\odot$-$10^{12} M_\odot$ (Misgeld and Hilker, 2011) going from ultra faint dwarfs (Willman et al., 2005) to monstrous giant ellipticals. Throughout this work we mainly focus on galaxies with a stellar mass greater than about $10^{8.6} M_\odot$. Given the break in galaxy structure at a stellar mass of around $10^{9.6} M_\odot$ (Kormendy, 1985; Boselli et al., 2008) we thus include galaxies roughly an order of magnitude in mass into the classical regime of dwarf galaxies. Fig. 1.1 displays optical images of a few example galaxies, illustrating the diversity displayed by these objects. My second comment on the quoted definition of galaxies regards their isolation from each other. From an observer's point of view, although somewhat subjective, a line is drawn between a single and a pair of galaxies when the two stellar bodies have merged, a definition which disregards the merging of the dark matter haloes. This comment, bringing us into the topic of galaxy mergers, leads us towards the question of how galaxies form and evolve, the subject of the following section.

---

[1] http://dictionary.reference.com/browse/galaxy

[2] Reliable measurements of the total mass of galaxies are rare and it is therefore oft convenient to make use of the total stellar mass which can be derived from the light emitted by the galaxy (Bell and de Jong, 2001).
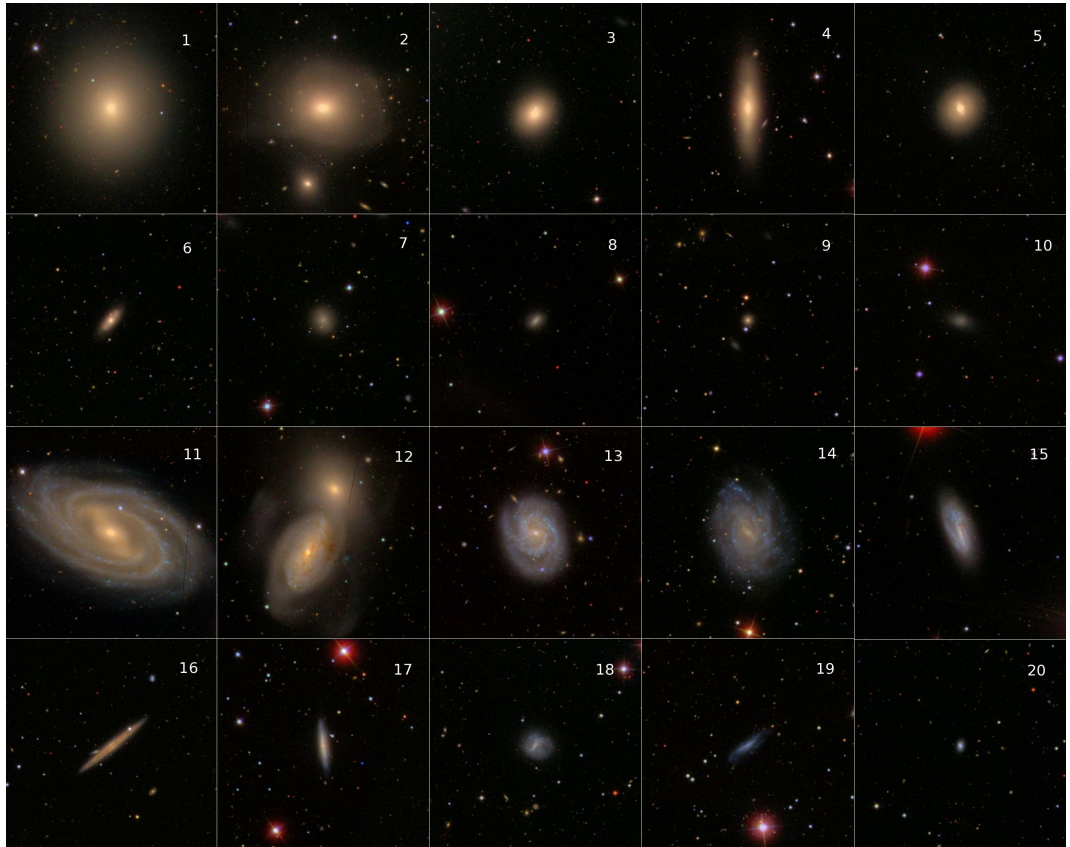
Figure 1.1: Optical multicolor images of a selected sample of galaxies in the redshift range 1300-1400km/s. Given the limited redshift range and the constant image size of 7x7' the various galaxies are shown roughly to scale. Upper 10 panels: galaxies with little or no star formation classified as early type including ellipticals (1,2,3,9), lenticular (4,5,6) and early-type dwarfs (7,8,10). Lower 10 panels: galaxies with ongoing star formation classified as late type including spirals (11,12,13,14,15,16,17,18,19) and a blue compact dwarf (20). Note the blue regions with young stellar populations as well as the dust lanes (dark), most clearly visible in the highly inclined systems. A system ongoing a merger (12) as well as post merger system (2) identified by the disturbed isophotes are included. The images are taken from http://cas.sdss.org.

1.2 Galaxy formation and evolution

Everything started with the Big Bang about 13.8Gyr ago (Komatsu et al., 2011). The baryonic matter, which makes up the visible part of what we call galaxies, decoupled from the electromagnetic radiation around $3 \cdot 10^5$yr later. Thereafter, density fluctuations, as can be seen in the cosmic microwave background radiation (Spergel et al., 2003), grew due to gravitational interaction forming increasingly dense collections of primordial gas. After some time the density reached levels at which a gravitational collapse could occur leading to the first stars (Abel et al., 2002). As galaxies are defined as *stellar systems*, galaxy formation and evolution is largely a theory about star formation and how this process is regulated over time. Gravity obviously plays a major role as it is the force through which material are pulled together and which consequently is behind star formation as well as stellar assembly. Mass is therefore a crucial parameter in determining galaxy evolution. Primordial gas clouds will likely have some net angular momentum due to tidal torques from neighbors (Schäfer, 2009). During the collapse the gas dissipates energy, which along with the conservation of angular momentum, leads to formation of disk structures (Larson, 1976; Fall and Efstathiou, 1980). Galaxy-galaxy interactions and mergers on the other hand tend to remove angular momentum which cause further gravitational collapse that leads to spheroidal components[3]. Over time galaxies grow through smooth accretion of gas (Kereš et al., 2005) which tends to preserve and enhance disk structures, or through mergers, which rather destroy disks and creates spheroids. These processes thus link a galaxy's structure to its formation history.

Galaxy formation and evolution is also a story about nucleosynthesis in the Universe. Stellar cores having densities and temperatures high enough for thermonuclear fusion are the main production sites of elements heavier than helium, hereafter metals. After having depleted their thermonuclear fuel massive stars explode as supernovae and metals are redistributed from the stars into the interstellar (or intergalactic) medium and can thereafter be incorporated in new generations of stars. Observational results suggest that more massive galaxies have stars with a higher metal content in their atmospheres (Panter et al., 2008). Massive galaxies, which have a higher binding energy, can more easily retain the gas expelled by supernovae explosions. This provides a possible explanation for the mass-metallicity relation (Tremonti et al., 2004), but other explanations are possible as well (Yates et al., 2011).

Supernovae are also a very important mechanism behind regulation of star formation over time. The enormous amount of energy released in supernove explosions leads to a heating of the surrounding gas and can furthermore completely expel gas from the system (Larson, 1974). As the heating leads to an increase in pressure support, supernovae feedback works against star formation. The effect is especially prominent for systems with moderate mass where the escape velocity is small. Supernovae feedback thus regulates star formation and more so for less massive systems (Governato et al., 2010). An additional mechanism that regulates star formation is feedback from active galactic nuclei (AGN). All massive galaxies are thought to possess central supermassive black holes (Häring and Rix, 2004). As these objects accrete material, tremendous amounts of potential energy is released which can heat the gas reservoir and thereby work against star formation. AGN feedback, which is expected to be most important for massive galaxies, has to some extent been observed where jets originating from the black hole are chock heating the large scale gas reservoir (Allen et al., 2006; Smolčić et al., 2007). AGN and supernovae feedback are thought to be the main mechanism shaping the abundance of galaxies as a function of mass with respect to the expected underlying distribution of dark matter haloes (Guo et al., 2010).

Several external processes can effect galaxies and their evolution. The most obvious case is ram-pressure stripping that occurs when a galaxy moves through an intergalactic medium (Gunn and Gott, 1972; Roediger and Hensler, 2005). Gas is stripped from the galaxies due

---

[3]Note that the commonly used term spheroidal is misconceiving, since these kind of structures usually are triaxial (Binney, 1985) and many have rotational support (Emsellem et al., 2007).
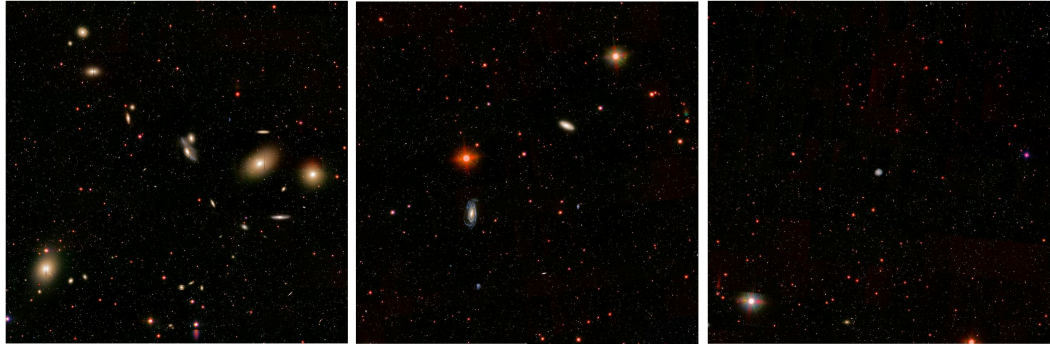
Figure 1.2: Illustration of galaxy environments from the dense Virgo cluster core (left), through a group environment (middle) to a relatively isolated galaxy (right). The color composite images are taken from http://cas.sdss.org. All images are 1x1' and the galaxies reside roughly at the same distance.

to the pressure exerted by the head wind. The phenomenon is not only predicted by theory but HI observations of galaxies in the Virgo cluster have actually revealed gas stripping in action (Kenney et al., 2004; Chung et al., 2007, 2009). The scenario is also backed up by Hα observations revealing galaxies with tails of ionized gas (Gavazzi et al., 2001; Sun et al., 2007; Smith et al., 2010b). Any extended gas reservoir which reaches much further than the visible part of the galaxy will also be affected by the intergalactic medium (Larson et al., 1980), preventing the galaxy from acquiring new gas. Tidal interaction with neighboring galaxies (Mayer et al., 2001) as well as the potential of the galaxy group/cluster (Moore et al., 1996) is another way in which galaxy properties can be affected by the environment in which the galaxy resides. Such tidal forces can remove gaseous material or stars from the objects as well as heat them dynamically. The latter also influences star formation due to a lowering of the density in the disk where the gas resides (e.g., Martig et al., 2009). Furthermore, it was recently shown that even the ionizing radiation from the first stars can have a strong environmental impact even on a scale much larger than galaxy clusters (Iliev et al., 2011).

Galaxies are certainly found in the most diverse places ranging from in complete isolation over groups of a few galaxies to very rich clusters containing thousands of members (see Fig. 1.2). Interestingly, most of the baryons in clusters, and in the Universe as a whole, are not contained in galaxies but rather in the intergalactic medium. For clusters and some galaxy groups the gas is warm and dense enough to be revealed by X-ray observations. The high gas densities make these regions ideal for ram pressure stripping.

To summarize, galaxy properties are shaped by galaxy mass and the environment in which the galaxy resides. Even though mass and environment seem fundamentally different it is not obvious to separate the two. For example, the number of mergers a galaxy has experienced certainly depends on the abundance and orbital characteristics of it's neighbors in the past, a property which very well can correlate with the present environment.

1.3 Studying galaxies with optical imaging

Observational studies of galaxies are done using imaging and spectroscopic observations. Spectra have a much larger information content concerning the spectral energy distribution with respect to images, but are on the other hand harder to obtain and have therefore usually limited spacial information. Broad band imaging data are easy to obtain and can efficiently probe the entire spacial extent of a galaxy. A challenge of multiwavelength imaging studies is to make full use of the rather limited spectral information in colors in order to provide as

much information about the galaxy as possible. The optical emission from a galaxy stems from a combination of light emitted by stars and gas which on the way to the observer can be altered by dust extinction. Through a modelling of these components it is possible to obtain valuable information about a galaxy's stellar population such as its total stellar mass (Bell and de Jong, 2001), chemical enrichment (Panter et al., 2008) and star formation history (Heavens et al., 2004), all of which are key properties for understanding the galaxy's formation and evolution as we saw in the previous section. In chapter 2 we test several stellar population models available in the literature and evaluate which one is most successful in reproducing optical broad band colors of nearby galaxies. The stellar population models are complemented with a treatment of emission lines and dust extinction resulting in *realistic* galaxy models with the aim of being able to extract as much and as detailed information as possible from photometry alone.

Observational studies often quantify environment using local galaxy number densities (Park et al., 2007) or cluster/group membership (Yang et al., 2007; Cava et al., 2009). Both properties are not perfect as the observations typically can not completely differentiate distances and velocities along the line of sight. Nevertheless, such studies have revealed important correlations between galaxy properties and environment such as e.g the morphology-density relation (Dressler, 1980) and the color-density relation (Park et al., 2007). Many recent studies have focused on the effect of the environment at *a fixed galaxy mass*, thereby adding a missing piece with respect to previous studies. Some information concerning the history of galaxy growth is contained in the local galaxy mass function. In chapter 3 we investigate correlations between galaxy properties and the local galaxy mass function, at fixed galaxy mass and group mass, and thereby look at galaxy formation and evolution from a new perspective.

1.4 Basic concepts

Abundance of galaxies The overall galaxy population is often characterized using the mass (or luminosity) function, describing the number of galaxies with mass M per unit volume. This function is often described using the Schechter (1976) formalism

$$\frac{\mathrm{d}n}{\mathrm{d}M} = \frac{\varphi^*}{M^*} e^{-M/M^*} \left(\frac{M}{M^*} \right)^{\alpha} \tag{1.1}$$

where M^* is a characteristic mass determining where the number of massive galaxies start to become rare, φ^* is a normalization related to the galaxy number density and α, often referred to as the faint end slope, is the power law exponent characterizing the behavior at low masses. The results of Bell et al. (2003) suggest that the constants take values of $\alpha \sim -1.0$, $M^* \sim 10^{11} \mathrm{M}_{\odot}$ and $\varphi^* \sim 0.004 \mathrm{Mpc}^{-3} \log_{10} M^{-1}$.

Distance measurements Distance in astronomy is measured with techniques that are calibrated with one another to be as accurate as possible for large distances. Distances to nearby stars are measured through their apparent motion with respect to more distant stars as the earth revolves around the sun. Such *trigonometric parallaxes* for distance determination made it possible to establish certain variable stars as *standard candles*, i.e., as sources of known luminosity for which distances can be determined through a comparison between observed and intrinsic brightness (Feast and Catchpole, 1997; Marconi et al., 2005). Using such *standard candles* Lemaître (1927) and Hubble (1929) discovered the relation between radial velocity and distance reflecting the expansion of the Universe. The Distance, d, to a remote source can thus be estimated based on the radial velocity, v, as measured from the Doppler shift of spectral lines

$$d = v/H_0 \tag{1.2}$$
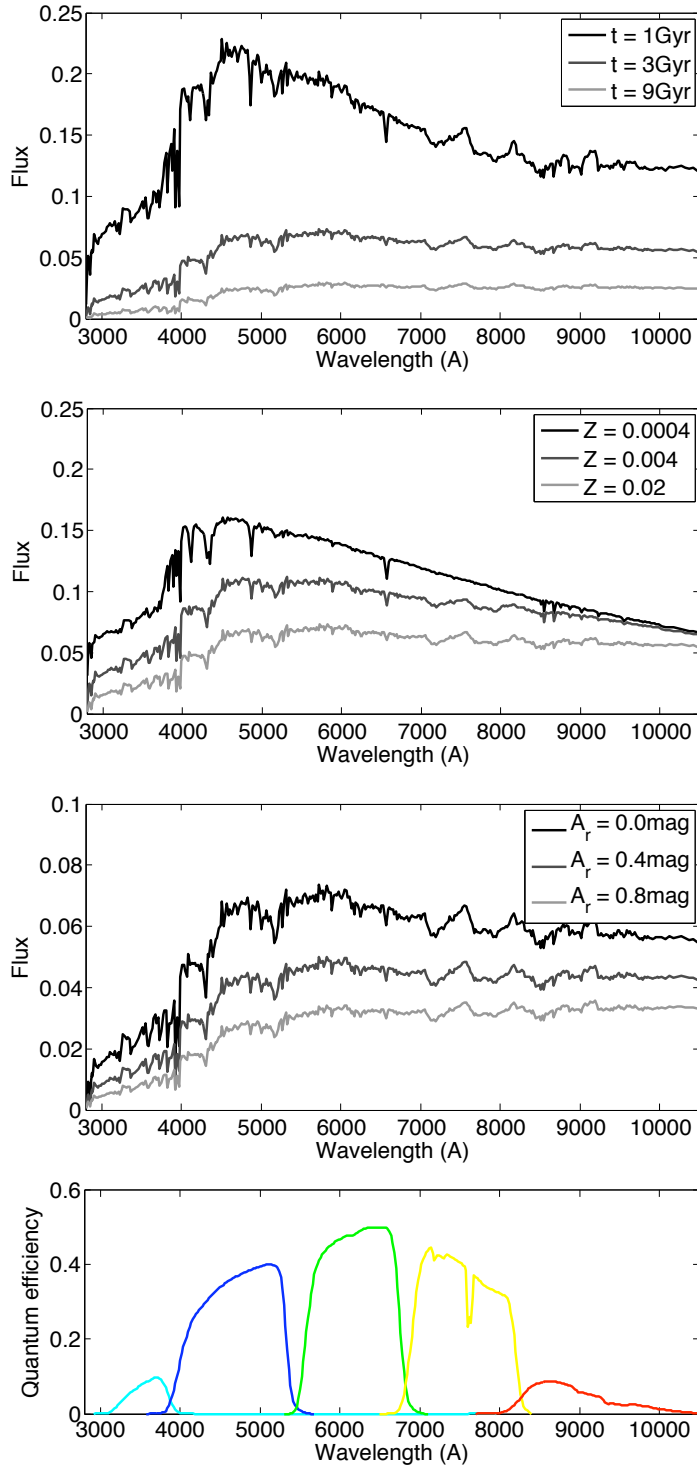
Figure 1.3: **Top panels:** Model fluxes (in arbitrary units) for single age, t, single metallicity, Z, stellar populations from Kotulla et al. (2009) are shown with black and grey lines. Fluxes are also shown for populations with various amount of r-band dust extinction, A_r, using a power law extinction curve of $A_\lambda \propto \lambda^{-0.7}$. The figure illustrates that fluxes and the spectral energy distributions change with stellar population age, metallicity and dust extinction. **Bottom panel:** Filter responses of the u (cyan), g (blue), r (green), i (yellow) and z (red) bands at an airmass of 1.3 as a function of wavelength.

where H_0 is the Hubble constant[4]. Not only the distance but of course also the difference in line of sight velocity contributes to v. This further complicates the estimate of d and we discuss it in chapter 3.

As the Doppler effect causes a redshift dependence of the observed spectral energy distribution, colors of galaxies change with distance. It is therefore possible to measure large scale distances to galaxies based on their colors (Bolzonella et al., 2000). Moreover, as galaxy structure changes with mass (and luminosity), distances to galaxies can also be estimated based on the observed galaxy structure (Binggeli et al., 1985) using the galaxy itself as a *standard candle*. In chapter 4 we combine galaxy photometry and structural properties which, complemented with a modelling of the galaxy population, allow us to determine galaxy distances with an improved accuracy.

Stellar population models Stars are gas spheres that spend most of their lives in hydrodynamical equilibrium supported from gravitational collapse by pressure upheld by thermonuclear fusion in the stellar core. Nuclear reaction rates can be computed for known temperatures, pressures and chemical compositions and the structure of the star can be computed by solving a set of coupled differential equations. The evolution of a star is determined by its mass and chemical composition. Effective surface gravities, temperatures and atmospheric chemical composition can be estimated for stars of known age, mass and initial chemical composition. This allows us to estimate the stellar luminosity and spectral energy distribution, either using stellar atmosphere models (see e.g., Lejeune et al., 1997) or empirical libraries of spectra (e.g., Le Borgne et al., 2003). A single stellar population model, hereafter SSP, describes the properties of an ensemble of stars with the same age and chemical composition. An important property of the stellar population is the mass distribution of stars at the time of formation, a property which is referred to as the initial mass function (IMF). From observations we know that the IMF can be described as e.g. a power law (Salpeter, 1955)

$$\frac{\mathrm{d}n}{\mathrm{d}M} \propto M^{-\alpha} \tag{1.3}$$

where $\mathrm{d}n/\mathrm{d}M$ is the number of stars in the mass interval from M to $M + \mathrm{d}M$ and where α is a constant. Stellar populations can thus be modelled as a function of IMF, age, chemical composition and total mass resulting in luminosities and spectral energy distributions.

1.5 Sources of data

The two main sources of data, both observational and from models, which are used in this thesis are described below.

The Sloan Digital Sky Survey The Sloan Digital Sky Survey (York et al., 2000), hereafter SDSS, is a dedicated imaging and spectroscopic survey using the 2.5m telescope at the Apache Point Observatory in New Mexico, USA, (Gunn et al., 2006) to observe a large part of the visible sky ($11663\deg^2$, data release 7 Abazajian et al. (2009)). The telescope operates in drift scan mode and collects images in the u,g,r,i and z-band (see Fig. 1.3 (Gunn et al., 1998)) almost simultaneously resulting in very accurate photometric measurements. The CCD detector has a pixel scale of 0.396". With the effective exposure of 54s the images reach an rms noise level of 24.2 mag arcsec^2 in the u band, 24.7 in g, 24.4 in r, 23.9 in i, and 22.4 in z as estimated in Lisker et al. (2008). The spectroscopic sample of SDSS (Strauss et al., 2002) includes all extended sources brighter than $m_r = 17.77$ with only $\sim 4\%$ incompleteness[5]. For these objects spectra have been obtained using optical fibers with a diameter of

---

[4]Throughout this work we adopt H_0=71km s^{-1} Mpc^{-1}
[5]In chapter 3 we show that the incompleteness is much larger for nearby galaxies.

3". The spectra cover a wavelength range from 3000-7000Å at a resolution ($\delta\lambda/\lambda$) of about 2000. The SDSS has turned out to be one of the most successful projects in the history of astronomy.

Semi-analytic galaxy catalogs Large numerical simulations such as the Millennium simulations (Springel et al., 2005; Boylan-Kolchin et al., 2009) operating under the framework of the most successful cosmological model, ΛCDM, predicts structure growth on scales from galaxy clusters to dwarf galaxies from the early Universe to the present day. A few groups have applied recipes for the physical processes behind galaxy formation onto the simulated dark matter structures thereby creating so called semi-analytic galaxy formation models. Even though many assumptions are made the models are able to produced galaxy catalogues that matches, e.g., the observed abundance and large scale clustering of galaxies (Bower et al., 2006; De Lucia et al., 2006; Guo et al., 2011). These models provide physically motivated galaxy distribution and velocities in three dimensions and therefore have the ability to be directly compared with observations. The model of Guo et al. (2011) is especially valuable considering that it further predicts many galaxy properties including luminosities, star formation histories, metallicities, bulge to disk ratios, colors and sizes.

1.6   Thesis outline

The rest of the thesis is structured as follows. Chapter 2 presents a detailed analysis of the performance of existing stellar population models in terms of their ability to reproduce u,g,r,i,z-band photometry of the local galaxy population considering a large range of star formation histories, chemical enrichments and dust extinctions. Chapter 3 describes a study of an essentially volume complete sample of nearby galaxies (<50Mpc) using imaging data and velocity measurements to probe how galaxy properties in terms of star formation histories, chemical enrichments, sizes and shapes depend on galaxy stellar mass and the environment in which the galaxy resides. In chapter 4 a study of the Abell 569 cluster core is presented where deep imaging in combination with semi analytic galaxy formation models have been used to probe the cluster luminosity function down to $M_R = -14$, and this study has revealed signs of galaxy interactions in several cluster members. Finally, chapter 5 provides some conclusions and an outlook.

Chapter 2 How well do stellar population models reproduce u,g,r,i,z-band photometry of the local galaxy population?

We test how well available stellar populations models can reproduce observed u,g,r,i,z-band photometry of the local galaxy population (0.02 ≤ z ≤ 0.03) as probed by the SDSS. Stellar population models for galaxies are created by synthesizing star formations histories and chemical enrichments using single stellar populations from several groups (Starburst99, GALEXEV, Maraston2005, GALEV). The role of dust is addressed through a simplistic, but observationally motivated, dust model that couples the amplitude of the extinction to the star formation history, metallicity and the viewing angle. Moreover, the influence of emission lines is considered (for the subset of models for which this component is included). The performance of the models are investigated by: 1) comparing their prediction with the observed galaxy population in the SDSS using the (u-g)-(r-i) and (g-r)-(i-z) color planes, 2) comparing predicted stellar mass and luminosity weighted ages and metallicities, specific star formation rates, mass to light ratios and total extinctions with literature values from studies based on spectroscopy. Strong differences between the various models are seen with several models occupying regions in the color-color diagrams where no galaxies are observed. We would therefore like to emphasize the importance of the choice of model. Using our preferred model we find that the star formation history, metallicity and also dust content can be constrained over a large part of the parameter space through the use of u,g,r,i,z-band photometry. However, strong local degeneracies are present due to overlap of models with high and low extinction in certain parts of color space.

2.1 INTRODUCTION

Optical broad band colors have proven to be a powerful tool in studying galaxies. Their dependence on luminosity and environment have greatly increased our knowledge of these systems (Visvanathan and Sandage, 1977; Park et al., 2007; Lisker et al., 2008). Colors are also used to derive quantities such as star formation histories and stellar masses (Tinsley, 1968; Searle et al., 1973; Charlot and Bruzual, 1991; Bell and de Jong, 2001; Bruzual and Charlot, 2003; Blanton and Roweis, 2007), both of which are key properties for understanding galaxy formation and evolution. For example, strong correlations between stellar mass and galaxy structure (Kauffmann et al., 2003b), star formation history (Panter et al., 2007), chemical enrichment (Panter et al., 2008) and gas content (Zhang et al., 2009) have been presented suggesting that mass is the main driver behind galaxy evolution. These relations reflect the importance of gravity on galactic scales and, moreover, provide further evidence concerning the expected connection between stellar mass and dark matter (cf. Moster et al., 2010). The derivation of star formation histories and stellar masses are made through a

modelling of the light emission from the galaxy and, if necessary, modelling of obscuration by dust. The method enables a comparison between observational quantities and galaxy formation models (e.g. De Lucia et al., 2006; Bower et al., 2006; Guo et al., 2011). The quality of the derivation of star formation histories and stellar masses from colors naturally depends on the quality of the models. A straightforward test is to check how well the models can reproduce the ensemble of observables. In this chapter we therefore take a closer look at how successful various models are in reproducing u,g,r,i,z-band photometry of the *local*[1] galaxy population.

The base ingredient of stellar population models of galaxies are single stellar populations (SSPs), which are combined into star formation histories by linear combinations (Tinsley, 1968; Searle et al., 1973). SSPs can consequently be seen as a basic ingredient of the models having a great impact on the emergent spectral energy distribution. A large number of single stellar populations models are available in the literature, including those of Leitherer et al. (1999); Bruzual and Charlot (2003); Maraston (2005); Kotulla et al. (2009), which we use in this chapter. We do not aim at being complete considering the numerous options available. However, we intend to cover some of the most widely used models predicting u,g,r,i,z-band photometry.

We treat dust obscuration in a simple way. The amplitude of the extinction is coupled to a galaxy's star formation history, metallicity and viewing angle, as motivated by works of (Cid Fernandes et al., 2005; Engelbracht et al., 2008; da Cunha et al., 2010; Masters et al., 2010), and a power law form of the the wavelength dependence of the extinction is assumed (see, e.g., Charlot and Fall, 2000). This method can be seen as an easy, but simplistic, approach with respect to detailed modelling of dust (e.g Tuffs et al., 2004; Popescu et al., 2011), though it has the nice feature that it only requires the axis ratio apart from colors.

As spectroscopic data carry a lot more information than u,g,r,i,z-band photometry a comparison with these kinds of data can serve as an important test. We therefore carry out a detailed comparison between literature data based on spectroscopy and our photometric model in order to validate that latter.

We note that a different approach to the testing of stellar populations models has been performed by Conroy et al. (2009, 2010) and Conroy and Gunn (2010). We refer the reader to this series of papers if they are interested in more details on the impact and uncertainties of various model ingredients rather than overall performance for optical broad band photometry.

This chapter is organized as follows. In Section 4.2 the observational sample used for the model evaluation is presented. The SSPs are introduced in Section 2.3 and how these are combined into star formation histories is described in Section 2.4. How we treat dust is described in Section 2.5. The performance of the models is presented in Section 2.6. The results are discussed in Section 2.7, and summarized in Section 4.10.

2.2 OBSERVATIONAL SAMPLE

Our source of observational **imaging** data is the Sloan Digital Sky Survey (SDSS) data release 7 (DR7 Abazajian et al., 2009). Galaxies with measured spectroscopic redshifts from the SDSS in the range $0.02 < z < 0.03$ are chosen to minimize the shifts in the spectral energy distribution caused by redshifts, while keeping a large sample with photometry of sufficient quality (note that, in particular, nearby galaxies have inaccurate photometric measurements from the SDSS pipeline (Blanton et al., 2005; Lauer et al., 2007; Bernardi et al., 2007; Lisker et al., 2007; Blanton et al., 2011).) Our sample consists of 24120 galaxies. We downloaded model magnitudes (modelMag) for these galaxies, which have been corrected for Galactic extinction using the maps of Schlegel et al. (1998). The sample spans an absolute magnitude

---

[1]By focusing on local galaxies ($0.02 < z < 0.03$) we circumvent the shift in the spectral energy distribution caused by redshift.

range of $-17 \geq M_r \geq -23$, and thus only the brightest of the dwarf galaxies are included. The photometry is k-corrected using the code of Chilingarian et al. (2010b), but the small amplitude of the corrections (≤ 0.1) suggests that the errors introduced in this step are negligible. In this chapter we only make use of magnitudes in the AB system, including the SDSS to AB conversion factors[2] of $u_{AB} = u_{SDSS} - 0.04$mag and $z_{AB} = z_{SDSS} + 0.02$mag. A quality assessment of the galaxy colors, as described in the Appendix 2.9.1, shows that the distribution of colors for the sample appears to be consistent with independent measurements.

Information about galaxy structure can aid in the interpretation of the modelling and is therefore of interest. Fig. 2.1 illustrates the properties of our galaxy sample, relying on structural parameters from the SDSS pipeline and the Galaxy Zoo project (Lintott et al., 2008). The SDSS pipeline (Stoughton et al., 2002) models galaxy light profiles through a best fit linear combination of a de Vaucouleurs and an exponential profile. The de Vaucouleurs fractions, $fracDeV$, is a measure of the fraction of light in the de Vaucouleurs profile of the two component fit. We further make use of the ratio of the semi major, a, and semi minor axis, b, at the object's 25mag/arcsec^2 isophote which we denote as a/b. From the Galaxy Zoo project (Lintott et al., 2011) we obtain P_{ell} which gives the probability that the objects are assigned elliptical morphology through a visual classification. We chose the values that were debiased from resolution effects (see Bamford et al. (2009)). Moreover, we make use of absolute r-band magnitudes, M_r, computed from the SDSS modelMags and redshifts using H_0=71km/s.

To test the performance of the photometric modelling we compare the outcome with results based on spectroscopic data from the SDSS. As the spectra are obtained using optical fibers with a diameter of 3" only a fraction of the light from each galaxy is sampled. Stellar mass weighted ages and metallicities as well as total V-band extinctions, A_V, are taken from the SEAGal/STARLIGHT project (Cid Fernandes et al., 2005). These data have been derived from the SDSS fiber spectra using a spectral synthesis technique in which dust is treated as a foreground screen with a Cardelli et al. (1989) extinction law for R_V=3.1. Luminosity weighted ages and metallicities are compiled from Gallazzi et al. (2005), who derived ages also by a spectral synthesis technique, while metallicities are instead derived through an analysis of absorption line indices, see (Worthey, 1994; Bruzual and Charlot, 2003; Thomas et al., 2003). We moreover make use of specific star formation rates based on Brinchmann et al. (2004) with an improved aperture correction (Salim et al., 2007). All data are based on SDSS DR7 except those compiled from Gallazzi et al. (2005) which are based on SDSS data release 4 (Adelman-McCarthy et al., 2006). For convenience we only use spectroscopic data for galaxies in common between these studies. The spectroscopic sample used throughout is therefore smaller than the photometric sample and contains 7542 galaxies in the range $0.02 < z < 0.03$. To allow a fair comparison with properties derived from photometry we make use of magnitudes measured within the spectroscopic fibers when comparing with the data from Cid Fernandes et al. (2005) and Gallazzi et al. (2005), while the modelMags are used for the specific star formation rates, since aperture corrections based on integrated SDSS photometry have been applied to these.

2.3 SINGLE STELLAR POPULATION MODELS

The stellar population models we test in this chapter are summarized in Table 2.1. We retrieve SSPs for each of these models which we combine into star formation histories as described in the following section. As most of the models have several options regarding specific model ingredients we decided to constrain the choice to avoid ending up with an impractical number of models. Details of the model sub-selection are given in Table 2.1 and the model ingredients are briefly commented below. The total amount of spectral information

---

[2]See www.sdss.org/dr7/algorithms/fluxcal
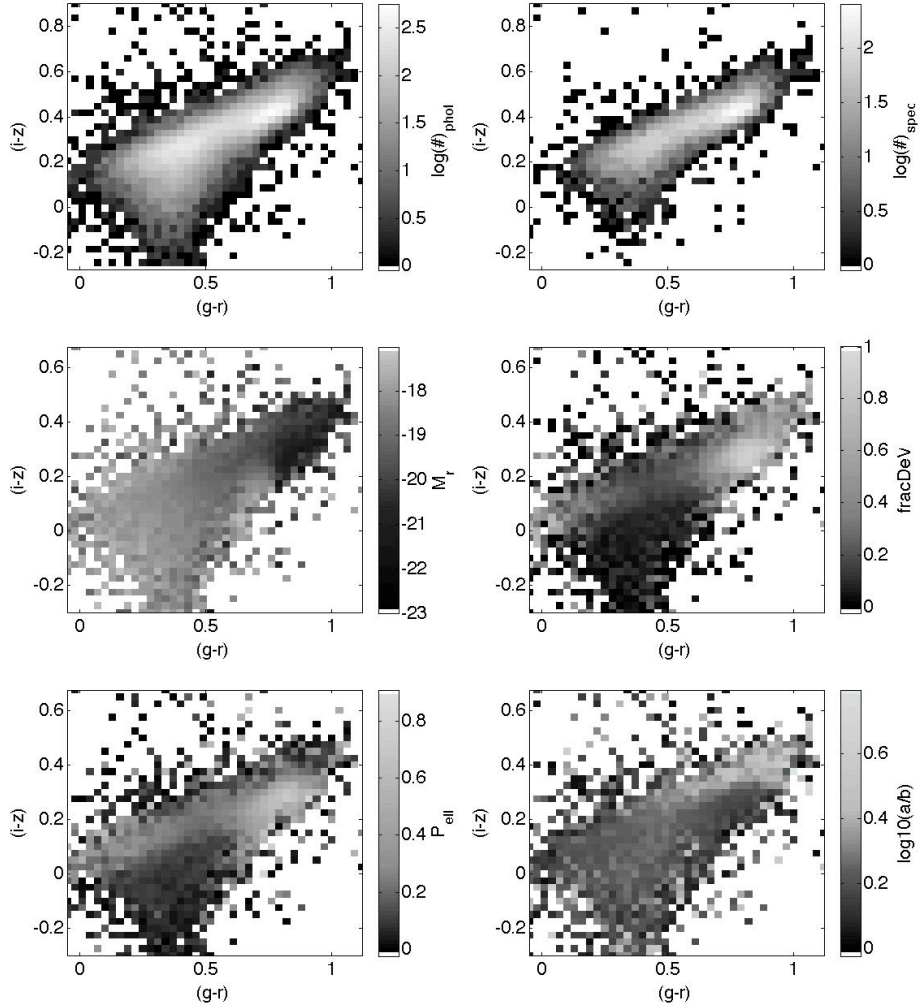
Figure 2.1: Properties of the galaxy samples used in this work. **Top panels:** 2D histograms in the (i-z) vs. (g-r) plane of the number of galaxies in the full sample selected from SDSS imaging data (left) and the spectroscopic subsample (right). **Middle and bottom panels:** Average values of absolute r-band magnitudes, M_r, r-band de Vaucouleur fractions, $fracDeV$, debiased probabilities of having elliptical morphology, P_{ell}, and axis ratios, a/b, for the full sample in bins of (i-z) vs. (g-r). Note that P_{ell} is only available for about 90% of the full sample.

contained in u,g,r,i,z-band photometry can be fully represented in four dimensions by, e.g., the $(u\text{-}r)$, $(g\text{-}r)$, $(i\text{-}r)$ and $(z\text{-}r)$ colors. However, for practical reasons we make use of 2D projections in the form of color-color diagrams, and for simplicity we constrain ourselves to the use of the $(u\text{-}g)\text{-}(r\text{-}i)$ and $(g\text{-}r)\text{-}(i\text{-}z)$ planes. Note that these projections alone can not capture all available information, though they ought to include the majority since they contain information from all five bands.

2.3.1 Stellar emission

The models fall in two different categories regarding how the stellar spectra are generated: theoretical models based on stellar atmosphere models (Lejeune et al., 1997) and models based on libraries of observed stellar spectra (Le Borgne et al., 2003).

2.3.2 Stellar evolution

In terms of stellar evolution several different sets of models are used, including Schaller et al. (1992); Bertelli et al. (1994); Cassisi et al. (2000); Girardi et al. (2000); Marigo and Girardi (2007); Bertelli et al. (2008); Marigo et al. (2008).

2.3.3 Initial mass function

In a recent review Bastian et al. (2010) conclude that there is no clear evidence that the initial mass function (IMF) varies strongly and systematically, and that the majority of systems on galactic scales are consistent with having a Kroupa (2001) or Chabrier (2003) initial mass function. However, an IMF that evolves with time cannot be excluded and recent studies do suggest a steeper IMF in massive elliptical galaxies (van Dokkum and Conroy, 2010, 2011; Spiniello et al., 2011). Here we investigate the the behavior of our models with respect to single slope IMFs. The Leitherer et al. (1999) model (S99) has the option of freely choosing the IMF. Figure 2.2 shows the behavior of the model boundaries as a function of IMF slope. As expected, the colors only change mildly with the IMF and we therefore chose to apply either a Kroupa (2001) or a Chabrier (2003) IMF. For each of the models one can choose between one of these two IMF prescriptions.

2.3.4 Emission lines

Emission lines are prominent features in optical spectra of star forming galaxies. It is therefore desirable to include emission lines in the modelling of photometric properties. Two of the models we use incorporate gas emission, namely S99 and GALEV (Kotulla et al., 2009). The former predicts the strength of $H\alpha$ and $H\beta$ while the latter predicts several other lines in the optical, which are expected to be important in star forming galaxies (Anders and Fritze-v. Alvensleben, 2003). Modelling of line emission from SSPs inevitably suffers from some uncertainty, but can be sufficiently accurate for predicting broad-band colors (Győry et al., 2011). From the color evolution of the SSPs it is clear that gas emission in the models only has a significant effect on the colors at ages of about 10^7yr or younger. Fig. 2.3 shows how the outlines of the model grids shift with the inclusion of emission line modelling. Modelling of line emission as in S99 or GALEV can be included in any of the models we consider by adding the corresponding change in the colors of S99 or GALEV. This can only be done for SSPs of the same age and metallicity under the assumption that the stellar emission in u,g,r,i and z are similar in the two models.
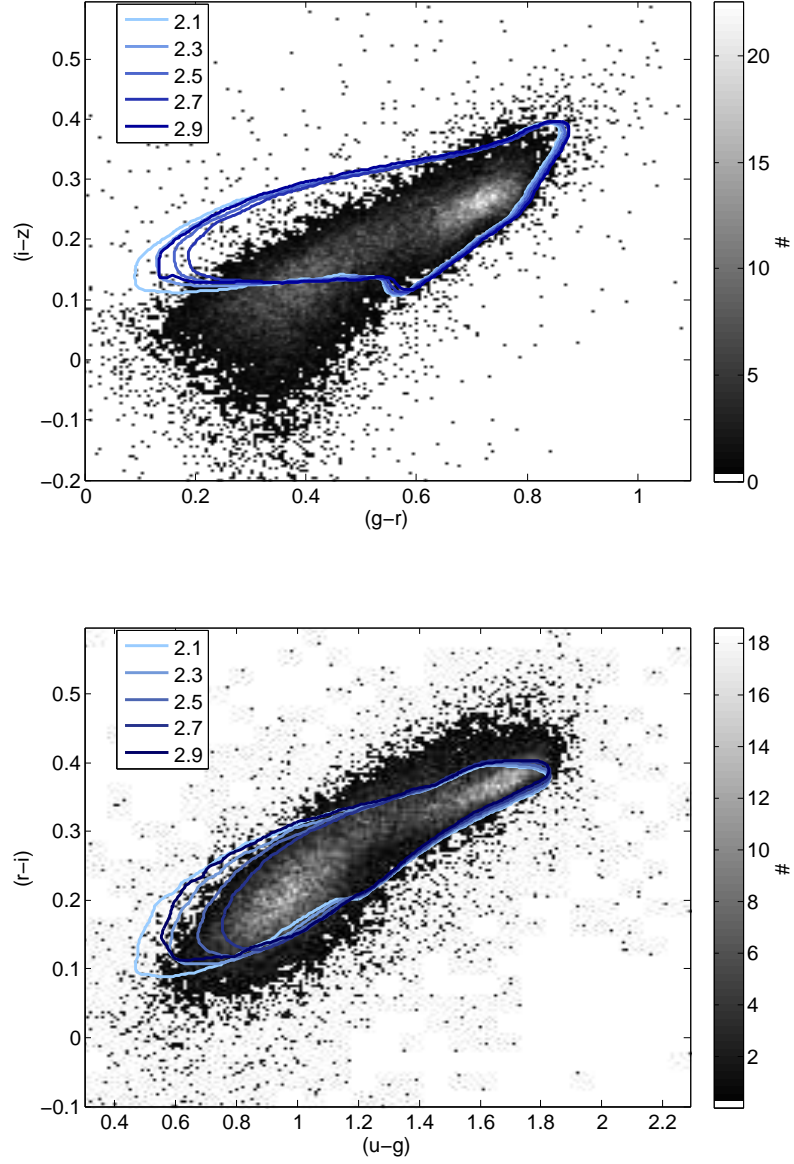
Figure 2.2: Top panel: (i-z) versus (g-r) for our sample of SDSS galaxies (number density map) along with model boundary contours (blue lines) for the S99P models with various IMF slopes, α (see. 1.3), from 2.1-2.9 (Salpeter=2.35). Bottom panel: Same as above but for (r-i) versus (u-g).
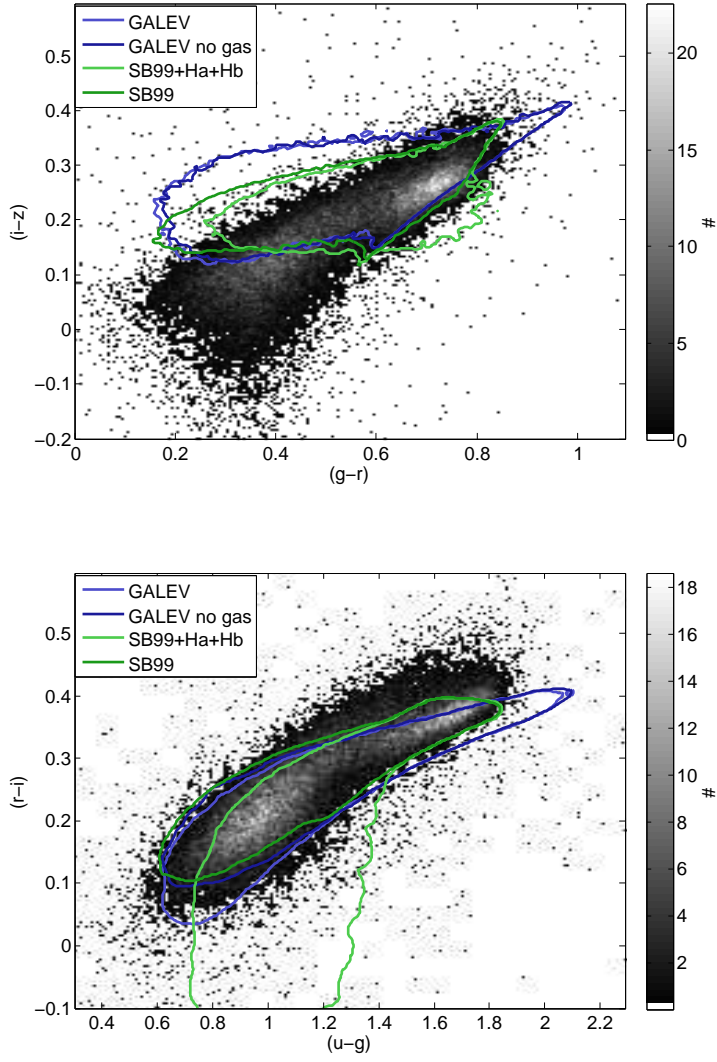
Figure 2.3: Top panel: (i-z) versus (g-r) for our sample of SDSS galaxies (number density map) along with model boundary contours for the GALEV (blue lines) and the SB99 (green lines) models, with and without the inclusion of emission line fluxes. Bottom panel: Same as above but for (r-i) versus (u-g).

Model ID	reference	stellar spectra	stellar evolution	IMF	line emission
BC03hr	Bruzual and Charlot (2003)	Le Borgne et al. (2003)	Bertelli et al. (1994)	Chabrier (2003)	no
BC03lr	Bruzual and Charlot (2003)	Lejeune et al. (1997)	Bertelli et al. (1994)	Chabrier (2003)	no
CB11hr	in prep.[c]	Le Borgne et al. (2003)	Bertelli et al. (2008)[a]	Chabrier (2003)	no
CB11lr	in prep.[c]	Lejeune et al. (1997)	Bertelli et al. (2008)[a]	Chabrier (2003)	no
S99P[f]	Vázquez and Leitherer (2005)	Lejeune et al. (1997)	Girardi et al. (2000)	Kroupa (2001)	yes
S99G[f]	Leitherer et al. (1999)	Lejeune et al. (1997)	Schaller et al. (1992)	Kroupa (2001)	yes
GALEV[d]	Kottulla et al. (2009)	Lejeune et al. (1997)	Bertelli et al. (1994)[e]	Kroupa (2001)	yes
M05	Maraston (2005)	Lejeune et al. (1997)	Cassisi et al. (2000)[ab]	Kroupa (2001)	no

[a] [b] [c] [d] [e] [f]

[a]Additional references left out, see model reference.
[b]These models have the option of choosing between populations with or without blue horizontal branch. We chose the latter.
[c]See González-Lópezlira et al. (2010) for a description.
[d]Updated SDSS filter responses from Doi et al. (2010) used.
[e]GALEV uses the 1999 version of isocrones from the Padova group.
[f]Magnitudes obtained by convolving the low resolution spectra with the updated SDSS filter response from Doi et al. (2010).

Table 2.1: Sources of SSP models

2.4 STAR FORMATION HISTORY

We synthesize star formation histories from the SSPs through the use of smooth models to which some stochastic sampling has been added. Such Monte Carlo libraries of star formation histories have previously been employed by several authors (Kauffmann et al., 2003b; da Cunha et al., 2008; Zibetti et al., 2009) and have proven versatile in modelling stellar population properties. The stellar population synthesis method we employ is thus not new, but the details differ between our and these previous works. The addition of some random component in the modelling is motivated by the knowledge that star formation to some extent occurs stochastically. Processes such as galaxy merging (Di Matteo et al., 2007) and ram pressure stripping (Gunn and Gott, 1972) often occur on short timescales and can strongly influence a galaxy's star formation history.

Gavazzi et al. (2002), inspired by the work of Sandage (1986), showed that a "delayed exponential" star formation history does a better job in reproducing colors of Virgo cluster galaxies than the classical exponential model. We therefore use this model as a starting point for our star formation histories

$$SFR = \frac{T}{\psi^2} \exp\left(-\frac{T^2}{2\psi^2}\right) \tag{2.1}$$

where SFR is the star formation rate, T is the time from the initial onset of star formation and ψ is a parameter governing the decline of star formation over time. We take the galaxy formation time to be 13.5Gyr ago. The exact starting point is not crucial due to the slow evolution of spectral properties at old ages, but it is to some extent motivated by current estimates of the onset of reionization in the Universe (Fan et al., 2006).

Star formation histories are created through a sampling of Eq. 1 using SSPs for values of ψ in the range 1Gyr to 20Gyr. The sampling is done logarithmically, since the color evolution is roughly proportional to the logarithm of the age. Thus, the age of each SSP, t_i, is randomly drawn from the following distribution

$$\frac{T^2}{\psi^2} \exp\left(-\frac{T^2}{2\psi^2}\right) \tag{2.2}$$

To compensate for the *logarithmic* sampling the strength, i.e. mass, of each SSP is multiplied by its age. In total 5ψ SSPs are used for each star formation history (more SSPs are needed to sample the larger range in log(age) spanned by models with higher values of ψ.). Stochasticity is introduced in the model through the sampling and by further modifying the strength of each SSP by multiplying with a random component. The random component is drawn from a distribution which is taken to be the absolute value of a normal distribution with ($\mu = 0, \sigma = 1$). To include many different metallicity configurations the SSPs constituting each SFH are randomly divided into five groups and each of these groups is assigned a random metallicity from the options available for that particular SSP.

The chosen input SSPs limit the lowest ages that can be included. However, note that in the model by Charlot and Fall (2000) the light from populations younger than 10^7yr is heavily obscured by the dust in the birth clouds and does not contribute significantly to the integrated light at optical wavelengths. We do therefore not need to consider these missing models at young ages.

Using optical spectral energy distributions the resolution in terms of the age of a stellar population seems to be limited to at least $\sim 10\%$ (González Delgado and Cid Fernandes, 2010). Any gaps introduced by a discrete sampling of a star formation history can thus safely be neglected if they are smaller than about 10%.

For a range of values[3] we generate 1000 models each of with results in 50000 models for

---

[3] $\psi = 1.0, 1.5, ...3.0, 3.25, ..., 9.0, 10.0, ..., 20.0$ in ψ. A variation in step size turned out to be useful for better coverage in the (u-g)-(r-i) and (g-r)-(i-z) planes.
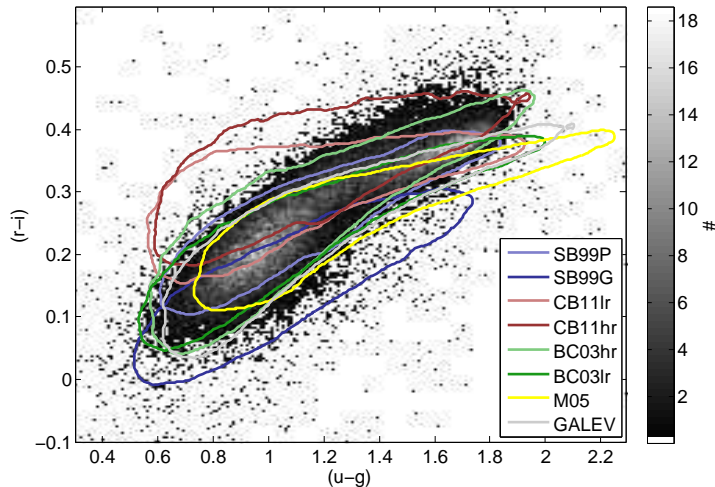
Figure 2.4: $(r\text{-}i)$ versus $(u\text{-}g)$ for our sample of SDSS galaxies (number density map) along with model boundary contours for eight different sets of stellar population models (color coded contours). Details of the models are summarized in Table 2.1 and described in Sect. 2.3 and 2.4.

each set of SSPs. Contours of the model boundaries in color-color space are created in the following way. 2D-histograms in $(g\text{-}r)$-$(i\text{-}z)$ and $(u\text{-}g)$-$(r\text{-}i)$ are made with bin sizes of 0.0055, 0.0040, 0.0100 and 0.0035 for $(g\text{-}r)$, $(i\text{-}z)$, $(u\text{-}g)$, and $(r\text{-}i)$, respectively. These histograms are convolved with a Gaussian kernel ($\sigma = 3$pixel) to remove the noise at the edges after which contours are drawn at a density of 0.2 models/pixel[4]. Figure 2.4 and 2.5 shows the outlines of these stellar population models (as summarized in Table 2.1) in the $(u\text{-}g)$-$(r\text{-}i)$ and $(g\text{-}r)$-$(i\text{-}z)$ planes.

2.5 DUST

In this chapter we employ a simplistic model for dust extinction in galaxies that has, by construction, no free parameters. Although several assumptions are made we expect our model to work reasonably well since it is constructed to capture the most important features of dust extinction in galaxies. It is motivated by:

1) The connection between the presence of dust and star formation/young stellar populations. da Cunha et al. (2010) showed that the dust mass in galaxies can be estimated remarkably well using the average star formation rate during the last 10^8yr (both quantities are determined from a model fit to photometry over a large wavelength range, $\sim 0.1-100\mu$m). They use a relation in the form of a power law with index 1.1 and find a scatter of about 0.5dex over at least three orders of magnitude in star formation rate. If this relation is normalized by the stellar mass, then the mass fraction of the dust is proportional to a power of the recent specific star formation rate, a property that can be constrained by optical colors alone (Brinchmann et al., 2004).

---

[4]The model boundaries in Fig. 2.2-2.6 are created in the same way.
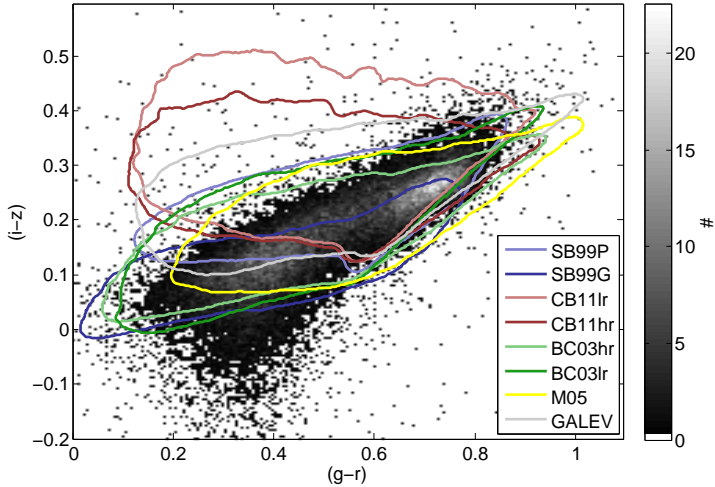
Figure 2.5: $(i\text{-}z)$ versus $(g\text{-}r)$ for our sample of SDSS galaxies (number density map) along with model boundary contours for eight different sets of stellar population models (color coded contours). Details of the models are summarized in Table 2.1 and described in Sect. 2.3 and 2.4.

We take the effective r-band extinction, A_r, to be

$$\tau_r = A_0 \left(\frac{\sum\limits_{i=0}^{n} s_i \mathrm{e}^{-(t_i/t_0)} / \sum\limits_{i=0}^{n} s_i}{\int_0^{13.5 Gyr} \mathrm{e}^{-(t/t_0)}\mathrm{d}t} \right)^{1.1} \tag{2.3}$$

where A_0 and t_0 are constants, t_i is the age of the ith SSP, s_i is the strength of the ith SSP, the summation is done over all n SSPs in the star formation history and the power index of 1.1 is taken directly from da Cunha et al. (2010). This equation makes A_r dependent on the fraction of young stars by comparing the strengths of the SSPs weighted by the factor $\mathrm{e}^{-(t_i/t_0)}$ (numerator) with the corresponding value for a constant star formation history (denominator). This is essentially a smoother version of the 10^8yr cut adopted by da Cunha et al. (2010) assuming that A_r is proportional to the dust to stellar mass ratio.

2) An observed correlation exists between metallicity and dust to gas mass ratio. We base the metallicity dependence of our dust models on the observational results of Engelbracht et al. (2008). Their relation between the nebular metallicity, Z, and HI to dust mass fraction ($M_{\mathrm{HI}}/M_{\mathrm{dust}}$) can be rather well fitted by a power law (the fit has a scatter of 0.5dex of which at least half can be explained by measurement errors) with low metallicity galaxies having higher $M_{\mathrm{HI}}/M_{\mathrm{dust}}$. Assuming that the nebular metallicity is the same as the average metallicity of the stellar populations contributing to the dust (see Eq. 2.3), z, this leads to a modification of A_r according to

$$A_r = A_r(z/z_\odot)^m \tag{2.4}$$

where m is a constant. Here we have further assumed that the metallicity is the only parameter governing $M_{\mathrm{HI}}/M_{\mathrm{dust}}$ for a fixed star formation history and that $M_{\mathrm{HI}}/M_{\mathrm{dust}}$ is proportional to A_r. We note that De Lucia and Blaizot (2007) also use a power law to model the metallicity dependence of the effective extinction with a power law index very similar to the one we adopt (see below).

3) At optical wavelengths, the wavelength dependence of the extinction appears to be rather well modelled by a power law of index k (Charlot and Fall, 2000)

$$A_\lambda \propto \lambda^k \qquad (2.5)$$

where A_λ is the effective extinction at a wavelength λ. Charlot and Fall (2000) use a different proportionality constant for stellar populations older and younger than 10^7yr. However, the contribution of optical light from young populations ($< 10^7$yr) is small due to obscuration from the dust clouds in which the stars were born. We therefore apply a single power law to model the wavelength dependence of the extinction. The effective extinction in u,g,r,i and z are computed using the effective wavelength of these filters. The use of effective wavelengths rather than a flux weighted average only introduce errors in A of a few percent (see Appendix 2.9.2).

4) The extinction is dependent on the angle under which the galaxy is seen. Empirical relations between colors and inclination for spiral galaxies in the SDSS were studied by Masters et al. (2010). Here we adopt a similar functional form to express how the effective r-band extinction is modified depending on the isophotal axis ratio, a/b,

$$A_r = A_r + \gamma_r \log_{10}(a/b) \qquad (2.6)$$

where γ_r is a constant. To determine γ_r we select spiral galaxies ($P_{ell} < 0.2$) from our spectroscopic sample and plot A_V from Cid Fernandes et al. (2005) versus $\log_{10}(a/b)$. For four bins in $fracDeV_r$ we determine γ_V (in analogy to γ_r) through least square fits. The bins were chosen such that they contain an equal number of galaxies and we find ($fracDeV_r$,γ_V) = (0.44-1.00,0.51),(0.17-0.44,0.58),(0.02-0.17,0.57) and (0.00-0.02,0.58). Given the small bin to bin variations we adopt γ_r=0.47 (i.e. γ_V=0.55) and apply Eq. 2.6 for all galaxies having $A_r > 0.05$mag according to Eq. 2.3 and 2.4. The extinction for galaxies with little or no dust are thus assumed to be inclination independent while dusty galaxies are treated as spirals.

We have constructed our model so that it does not have any free parameters. The constants included, A_0, t_0, m and k have values that can be inferred from previous studies. However, the constants can to some extent be adjusted in order to produce as realistic an ensemble of models as possible. We follow the latter approach and adjust A_0 and k to improve the agreement between models and the observations (see Appendix 2.9.3 for more details). We adopt $A_0 = 0.40$, $t_0 = 0.30$Gyr, $m = 1.7$ and $k = -1.1$.

2.6 PERFORMANCE

We test the models described above using an observational sample of galaxies from the Sloan Digital Sky Survey DR7 (Abazajian et al., 2009) as described in Sect. 4.2. Given the boundaries of the model cloud for dust free models in Fig. 2.4 and 2.5 in comparison with the observations we see large differences between the various models. In particular the models of Charlot and Bruzual in preparation (CB11) and GALEV occupy a large region in (g-r)-(i-z) where no galaxies are found to reside and the same is true for CB11 in (u-g)-(r-i). The overall best agreement between observations and models is shown by the Bruzual and Charlot (2003) models based on observed stellar spectra (BC03hr) and spectra from stellar atmosphere models (BC03lr). Of these two BC03hr performs significantly better in the reddest region of both color-color diagrams. In the following we have therefore adopted BC03hr as our preferred model. A missing ingredient in this model is the line emission. As we showed in Fig. 2.3 inclusion of line emission from GALEV only changes the model track slightly. We can therefore safely include line emission from GALEV into the BC03hr models as discussed in Sect. 2.3.4. Moreover, we apply our dust models to BC03hr. The resulting change in the model boundaries is shown in Fig. 2.6. Considering the photometric errors the

model performs very well in reproducing the colors of the galaxy sample, except at about $(g\text{-}r,i\text{-}z)=(0.4,0.0)$, where models appear to be missing.

2.6.1 Derived parameters

To illustrate the predictions of the models in terms of galaxy properties Fig. 2.7-2.9 show the stellar mass weighted[5] ages, metallicities and total r-band extinction in the color-color planes along with their standard deviations. This is shown for the BC03hr models with dust and line emission which are in good agreement with the observations (Fig. 2.4 and 2.5). A strong, rather orthogonal dependence is seen between age and metallicity. However, for a region of color space roughly from $(u\text{-}g,r\text{-}i)=(1.1,0.2)$ to $(u\text{-}g,r\text{-}i)=(1.6,0.4)$ and $(g\text{-}r,i\text{-}z)=(0.5,0.2)$ to $(g\text{-}r,i\text{-}z)=(0.8,0.3)$ all properties are rather poorly constrained due to a mix of models with high and low dust extinction. The model library was constructed to cover the $(u\text{-}g,r\text{-}i)$ and $(u\text{-}g,r\text{-}i)$ diagrams and does not tell anything about the probability that a specific model is a good representation of the observations. Further improvement can be achieved using a Bayesian approach. With help from the semi-analytic galaxy formation models of Guo et al. (2011) we compute model weights to match the distribution of stellar population models with semi-analytic galaxies in terms of density in stellar mass weighted age versus stellar mass weighted metallicity, see Appendix 2.9.5. For 10 randomly chosen example galaxies we show the SDSS color composite image[6] along with with a star formation history derived through a Bayesian maximum likelihood for the BC03hr models with emission lines and dust, see Fig. 2.10.

2.6.2 Visual checks

As a test we selected random samples of galaxies for three different parts in $(g\text{-}r)\text{-}(i\text{-}z)$ space, which according to our models have certain special characteristics. The first group contains galaxies that belong to a well populated region around $(g\text{-}r,i\text{-}z)=(0.4,0.0)$ that can not be reached by any models (Fig. 2.11, yellow dots). This group seems to be populated by star forming galaxies that in many cases exhibit Sm type morphology. The second group at $(g\text{-}r,i\text{-}z)\sim(0.8,0.3)$ contains galaxies that, according to our model, are expected to have strong extinction by dust (Fig. 2.11, green dots). This group contains many edge on or highly inclined disk galaxies. The last group at $(g\text{-}r,i\text{-}z)\sim(0.8,0.2)$ is expected to contain dust free galaxies (Fig. 2.11, grey dots). With a few exceptions this group contains early-type galaxies with little or no visible dust and star formation. SDSS multicolor composites of individual representative galaxies are shown in Fig. 2.11.

2.6.3 Comparison with spectroscopic studies

There is no question about the superior information content of optical spectra with respect to broad band photometry. Photometry is nevertheless an important probe of stellar populations of galaxies as it is easy to obtain and because spectroscopic data often suffer from aperture bias. As mentioned in Sect. 4.2 we compiled spectroscopically determined galaxy parameters from the literature for testing the performance of our photometric model. The parameters considered are stellar mass weighted ages, age_{mass}, luminosity weighted ages, age_r, stellar mass weighted metallicities, z_{mass}, luminosity weighted metallicities, z_{lum}, specific star formation rates, $SSFR$[7], r-band mass to light ratios, M/L_r, and V-band extinctions,

---

[5]In this work stellar masses are derived using a Chabrier (2003) IMF and the stellar mass are taken to be the mass in present day stars and remnants.

[6]Images are taken from http://cas.sdss.org/dr5/en/tools/chart/list.asp

[7]Specific star formation rates are taken as the ratio of the average star formation rate during the last 10^8yr and the galaxy's stellar mass. An average star formation rate over the last 10^8yr as determined from the stellar continuum has proven to be successful in reproducing star formation rates as estimated from emission lines (Asari et al., 2007).
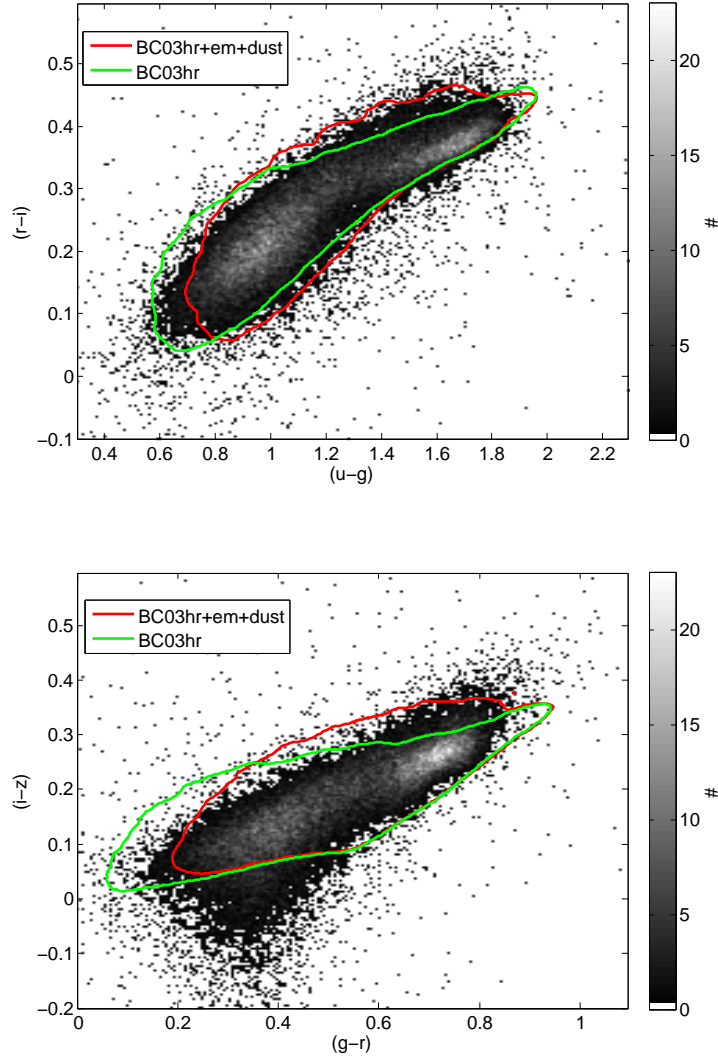
Figure 2.6: (*i-z*) versus (*g-r*), upper panel, and (*r-i*) versus (*u-g*), lower panel, for our sample of SDSS galaxies (number density map) along with model boundary contours for the BC03hr model (green) and the BC03hr model with dust and line emission (red).
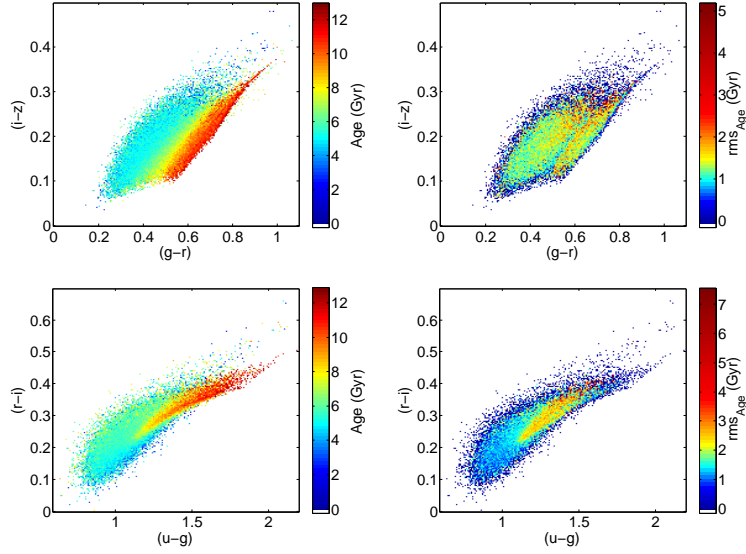
Figure 2.7: Left panels: stellar mass weighted age (color coded pixels) as a function of (i-z) versus (g-r), as well as (r-i) versus (u-g) for our 50000 models based on BC03hr with dust. Right panels: standard deviation in stellar mass weighted age (color coded pixels) as a function of (i-z) versus (g-r), as well as (r-i) versus (u-g) for our 50000 models based on BC03hr with dust.
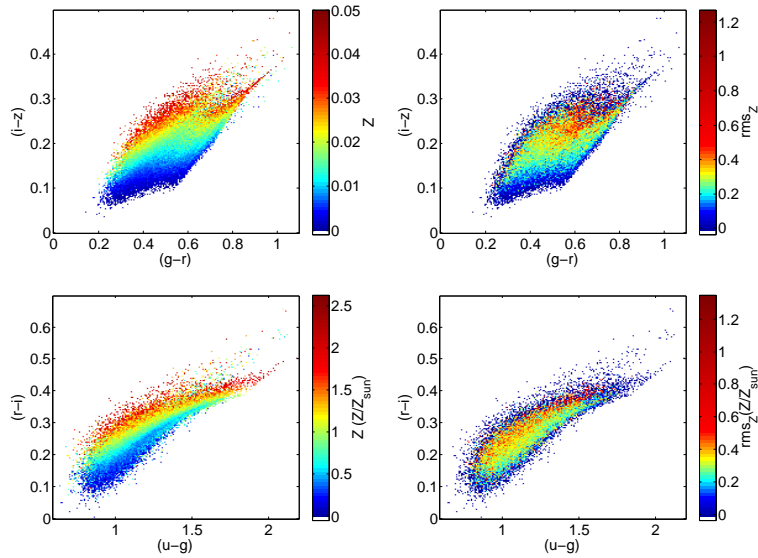
Figure 2.8: Left panels: stellar mass weighted metallicity (color coded pixels) as a function of (i-z) versus (g-r), as well as (r-i) versus (u-g) for our 50000 models based on BC03hr with dust. Right panels: standard deviation in stellar mass weighted metallicity (color coded pixels) as a function of (i-z) versus (g-r), as well as (r-i) versus (u-g) for our 50000 models based on BC03hr with dust.
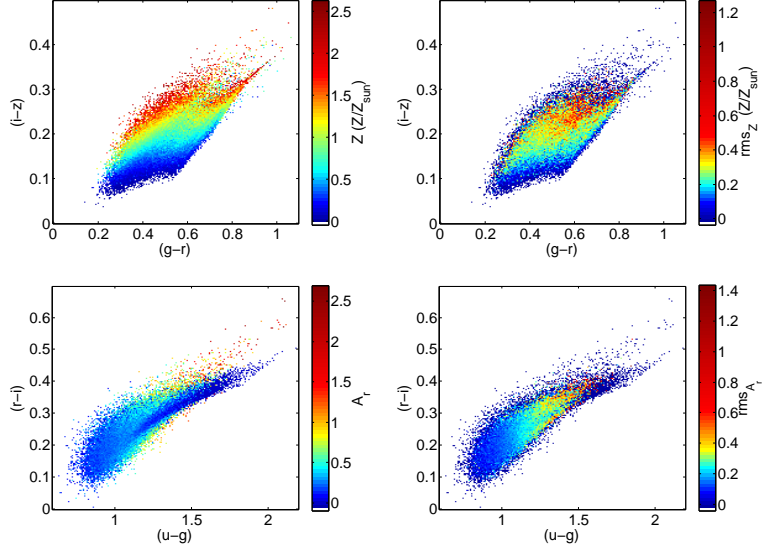
Figure 2.9: Left panels: total r-band extinction (color coded pixels) as a function of $(i\text{-}z)$ versus $(g\text{-}r)$, as well as $(r\text{-}i)$ versus $(u\text{-}g)$ for our 50000 models based on BC03hr with dust. Right panels: standard deviation in total r-band extinction (color coded pixels) as a function of $(i\text{-}z)$ versus $(g\text{-}r)$, as well as $(r\text{-}i)$ versus $(u\text{-}g)$ for our 50000 models based on BC03hr with dust.

A_V. To be able to make a fairer comparison between photometrically and spectroscopically derived quantities we set the maximum of age_{mass} and minimum of A_V from Cid Fernandes et al. (2005) to 13.5Gyr and 0.0mag, respectively, as opposed to 18Gyr and -0.9mag in the catalogue. Note, however, that age_{mass} derived from spectroscopy may still be systematically older as the star formation histories from which age_{mass} is derived include SSPs with ages up to 20Gyr. Additionally, we set the minimum $SSFR$ to -3 in $\log 10(M_{sun}/(10^{10}\text{Gyr}))$ as non star forming galaxies in our photometric model have $SSFR$=-Inf in $\log 10(M_{sun}/(10^{10}\text{Gyr}))$. Fig. 2.12 shows a comparison of derived parameters in the $(i\text{-}z)$ vs. $(g\text{-}r)$ diagram. The overall agreement between the spectroscopically and the photometrically determined quantities appears to be rather good. The main differences in the behavior in $(i\text{-}z)$ vs. $(g\text{-}r)$ are that: 1) photometric metallicities increase with $(i\text{-}z)$ and are almost independent of $(g\text{-}r)$, while spectroscopic metallicities also depend on the latter; 2) very young objects, as determined from photometry, are present at $(g\text{-}r,i\text{-}z)$=(1.0,0.5), but these are not seen if spectroscopic ages are used. A direct comparison between the derived parameters, see Fig. 2.13, does show a significant scatter as well as some systematic differences. As the differences are rather "irregular" we refrain from an attempt to parameterize them.

Under the assumption that the spectroscopically derived quantities are of higher accuracy than those derived from photometry we can probe the quality of the parameters included in the fitting. Results of such a test are shown in Table 2.2 in terms of the σ in the spectroscopically derived quantity at fixed photometrically derived values. The use of u,g,r,i,z-band photometry alone leads to a low σ in all properties except the SSFR. This problem is solved if a prior as a function of M_r is introduced and additionally a slight improvement can be achieved by introducing a/b in the fitting. Note however that M_r can be estimated using u,g,r,i,z-band photometry with an accuracy of about 1mag, a sufficiently good estimate to reach almost the same accuracy as if M_r itself is used. Using only M_r, or M_r and a/b, we can still constrain several quantities as the model galaxy properties have a strong mass/luminosity dependence as well as some structural dependences (Guo et al., 2011), but the σ is consider-

24

Figure 2.10: Images (left): 50'x50' SDSS u,g,r,i,z color composite images (Szalay et al., 2002) of 10 randomly selected galaxies from our sample. Diagrams (middle): $(i$-$z)$ vs. $(g$-$r)$ colors for the galaxies (red dots) and the model boundaries (black lines). Diagrams (right): Normalized star formation rates (red lines) with errors (shaded region) for the corresponding galaxies as a function of stellar age. These star formation histories have been derived through a Bayesian maximum likelihood using all 10 colors and our models based on BC03hr with emission lines and dust (see Appendix 2.9.5). Stellar mass weighted ages and metallicities, z, as well as effective r-band optical depths are indicated above each image+diagram pair along with absolute r-band magnitudes, M_r, and Hα equivalent widths from the SDSS (positive values indicate emission and negative values absorption).
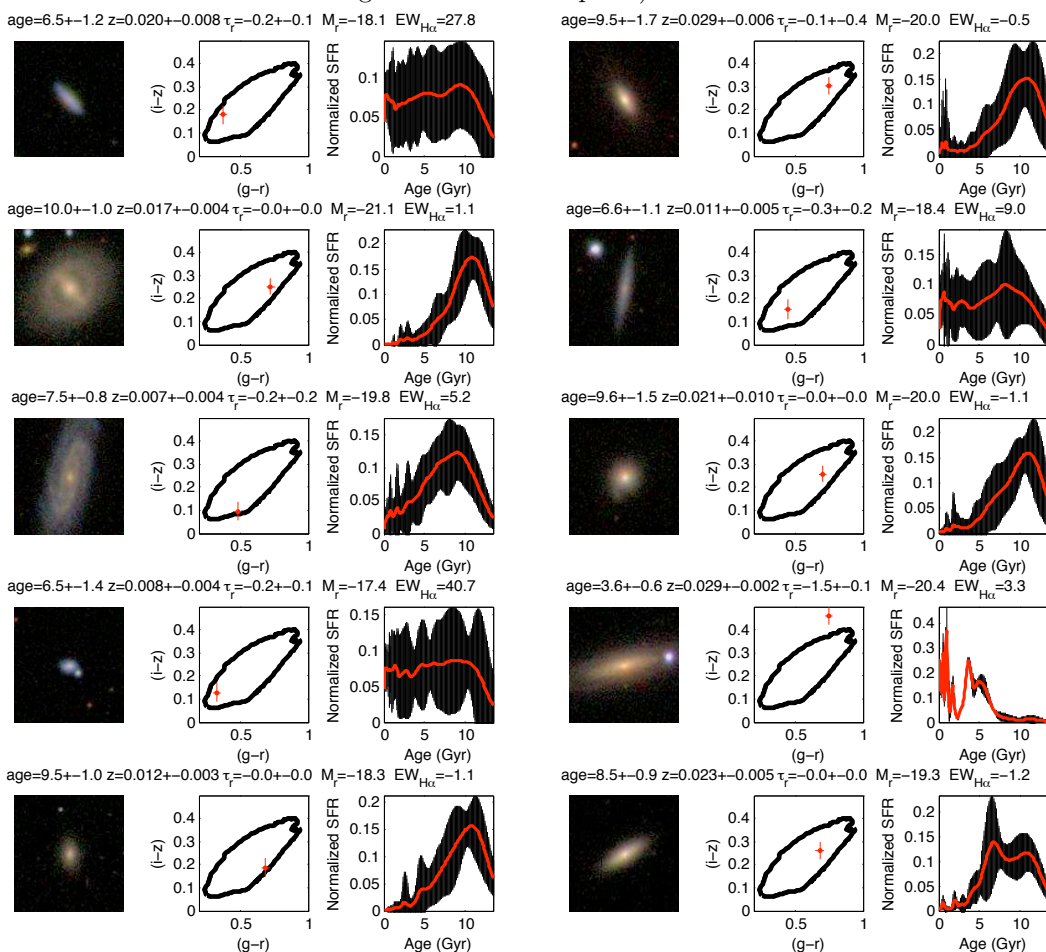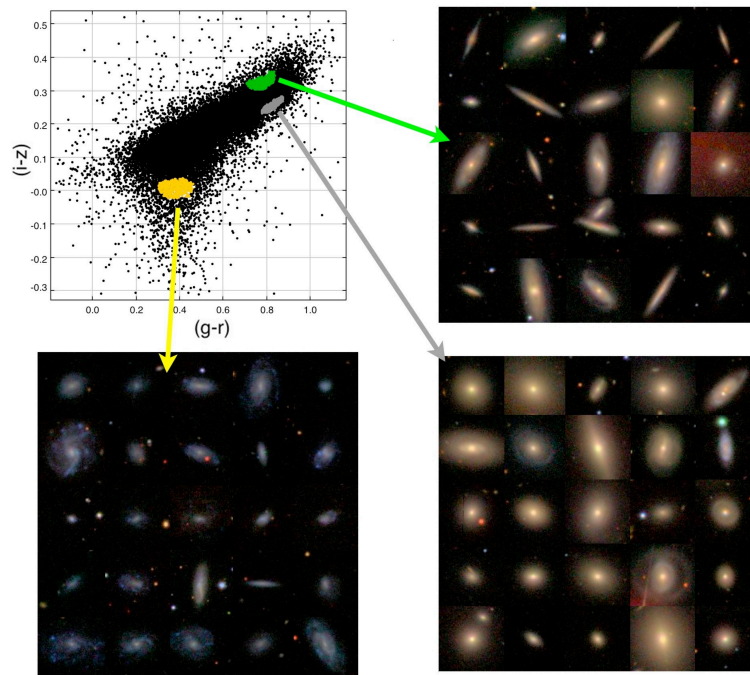
Figure 2.11: Illustration of galaxies with special characteristics according to our BC03hr model with dust extinction. From all galaxies (black dots) objects with high expected extinction (green dots), low expected extinction (grey dots) and galaxies falling off the model grid (yellow dots) are selected. SDSS color composites are shown for randomly chosen examples from each group. Note the high frequency of highly inclined disks in the high extinction sample.
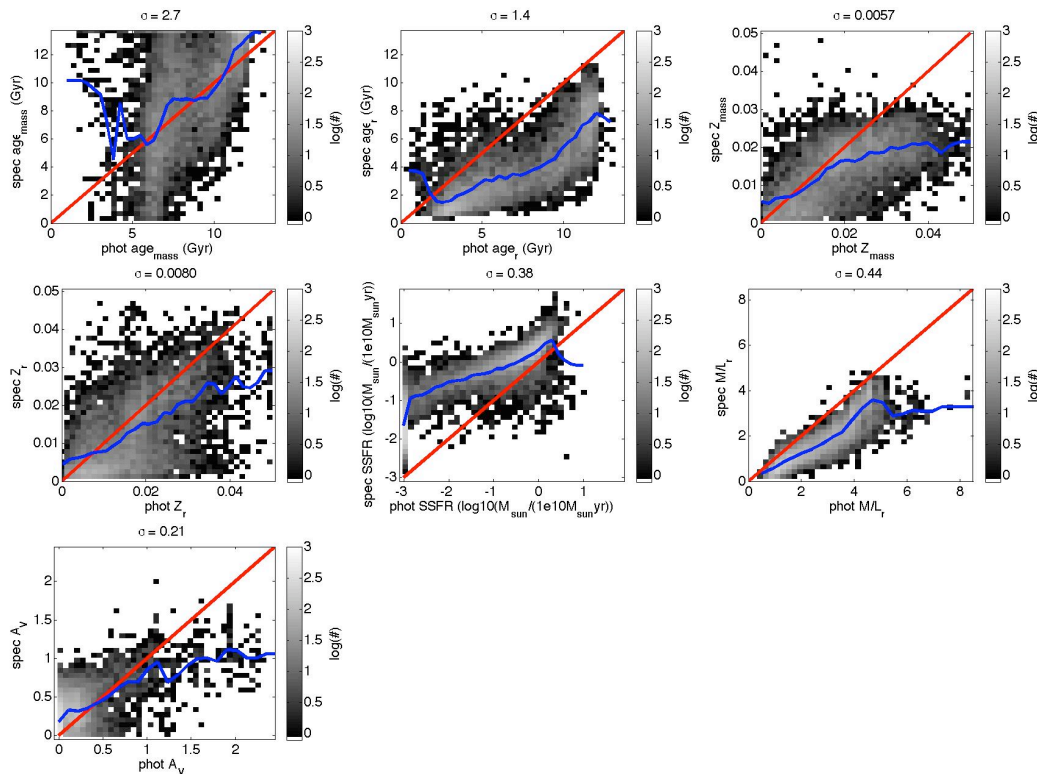
Figure 2.12: Comparison between stellar mass weighted ages, age$_{mass}$, r-band luminosity weighted ages, age$_r$, stellar mass weighted metallicities, z$_{mass}$, luminosity weighted metal-licities, z$_{lum}$, specific star formation rates, $SSFR$, r-band mass to light ratios, M/L_r, and total V-band extinctions, A_V, for the spectroscopic comparison sample (greyscale histogram) as derived from u,g,r,i,z-band photometry (phot) and spectra (spec) (Cid Fernandes et al., 2005; Gallazzi et al., 2005). The red lines show the 1:1 relations, blue lines indicate the mean in the spectroscopic values in bins of the photometric values. The bin widths are 1/30 of the entire range displayed, however, these are in some cases adjusted to enclose at least 50 galaxies in each bin. On top of each figure the standard deviation in the spectroscopic values around the mean, i.e. the blue line, is indicated.

ably higher in many of the parameters.

Moreover, with a similar technique we can test whether the exclusion of certain bands in the fitting can improve the quality of the derived parameters. We find that this is the case. Removal of one or two bands can indeed decrease the σ of the comparison with the spectroscopy by 5-10% for each of the parameters tested. However, an increase in the accuracy of one parameter typically comes at the expense of a diminished accuracy in another. For example, excluding u and g leads to a better estimate in the mass weighted metallicity but makes the accuracy of the $SSFR$ much worse. As no overall improvement is achieved by excluding one or two bands, we prefer to keep all bands in the fitting.

2.6.4 Insights from spectral fitting

While the main focus of this chapter is testing model predictions for u,g,r,i,z-band photom-etry an efficient test can be achieved by comparing observed and modelled spectra instead of colors due to the much larger information content. A drawback is that we already expect
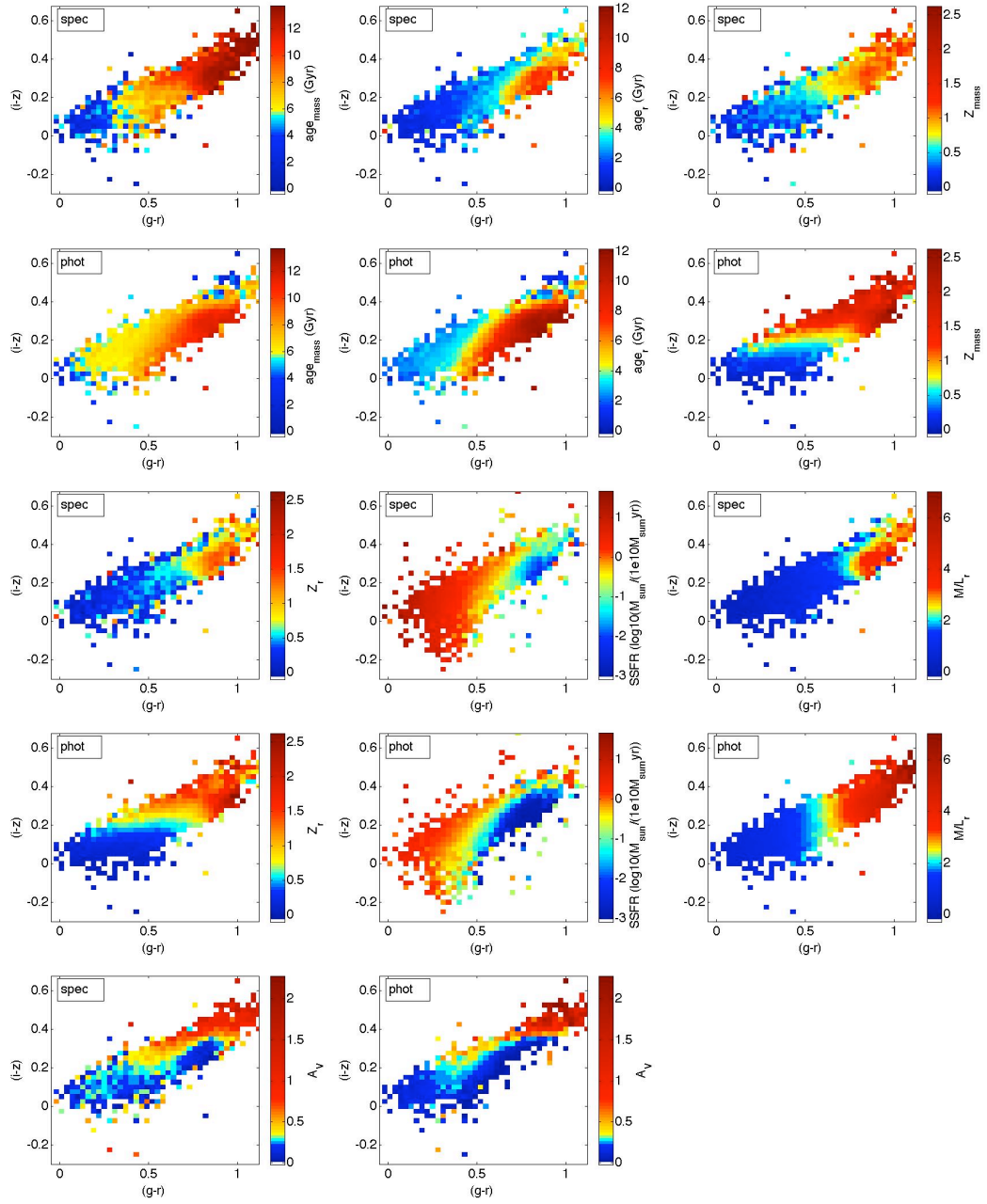
Figure 2.13: Galaxy properties for the spectroscopic comparison sample as we derived from u,g,r,i,z-band photometry (phot) and Cid Fernandes et al. (2005); Gallazzi et al. (2005) derived from spectra (spec). Color coded pixels show the average values of stellar mass weighted ages, age_{mass}, r-band luminosity weighted ages, age_r, stellar mass weighted metallicities, z_{mass}, r-band luminosity weighted metallicities, z_{lum}, specific star formation rates, $SSFR$, r-band mass to light ratios, M/L_r, and total V-band extinctions, A_V, in the $(i\text{-}z)$ vs. $(g\text{-}r)$ diagram. Spectroscopic quantities are derived either using spectral synthesis techniques (age_{mass},z_{mass},age_r) or an absorption line index analysis (z_{lum}).

28

Table 2.2: Dependence of the σ in stellar mass weighted age, age_{mass}, luminosity weighted age, age_r, stellar mass weighted metallicity, z_{mass}, luminosity weighted metallicity, z_{lum}, specific star formation rate, $SSFR$, r-band mass to light ratio, M/L_r, and V-band extinction, A_V, compared with the spectroscopically determined values. The parameters used in the computation of the maximum likelihoods are u,g,r,i,z-band photometry, ugriz, a prior based on M_r, prior(M_r), a prior based on a Monte Carlo estimate of M_r from u,g,r,i,z-band photometry, prior(ugriz$\rightarrow M_r$), and the isohotal axis ratio a/b.

				σ			
fitting parameters	age_{mass} (Gyr)	age_r (Gyr)	z_{mass} ($z_\odot$)	z_{lum} ($z_\odot$)	$SSFR$ (dex)	M/L_r ($M_\odot/L_\odot$)	A_V (mag)
ugriz	2.8	1.6	0.33	0.43	0.87	0.49	0.21
prior(M_r)	2.9	2.3	0.31	0.44	0.50	0.89	0.27
a/b + prior(M_r)	3.2	2.3	0.38	0.48	0.73	1.01	0.24
ugriz + prior(ugriz$\rightarrow M_r$)	2.8	1.5	0.34	0.44	0.75	0.50	0.21
ugriz + a/b + prior(ugriz$\rightarrow M_r$)	2.8	1.5	0.34	0.44	0.49	0.50	0.21
ugriz + prior(M_r)	2.9	1.6	0.32	0.44	0.49	0.50	0.21
ugriz + a/b + prior(M_r)	2.8	1.5	0.32	0.44	0.49	0.50	0.21

there will be some issues with the modelling because the chemical content of a galaxy is described by a single parameter in our model, i.e., the metallicity, an approximation that is not expected to reproduce all possible line ratios in galaxies.

We randomly select 1000 galaxies in our sample for which we obtain fully reduced flux calibrated SDSS spectra. These spectra are fitted to our model library in the wavelength range 3700Å to 7000Å (rest frame), as described in the Appendix 2.9.4. Sky lines and emission lines are masked out in the fit and the line of sight velocity distribution is taken into account.

The median reduced χ^2 of the fit to the 1000 galaxies is 3.9 for the BC03hr models with dust. This is a factor of two smaller than if only SSP models are used. A visual inspection of observations and best fit models show that not only issues with lines, but also with the continuum fit cause the poor quality. We note that the median reduced χ^2 can be substantially lowered if the fitted region is restricted to a shorter wavelength interval like 5000Å to 5500Å instead of 3700Å to 7000Å.

2.7 DISCUSSION

Before starting the discussion about the model performance and prediction it is worth taking a look at how the models are constructed.

2.7.1 Model ingredients

As opposed to Conroy et al. (2009, 2010) and Conroy and Gunn (2010) our aim has not been to judge each model ingredient and we thus find it suffice to say that some, but certainly not all, SSP models can be successfully used to predict u,g,r,i,z-band photometry of the local galaxy population. Caution should be taken in the choice of model. Of the models we tested (see Table 2.1), *we recommend the Bruzual and Charlot (2003) high resolution models for the purpose of predicting optical broad band photometry of galaxies.*

Does our library of star formation histories make sense? Given the distribution of average values for our models it seems we have covered essentially all possibilities with ages from 0-13Gyr, metallicities from 0.00-0.05 and with extinctions from 0-3mag. Furthermore we note that Eq. 2.1 produces star formation histories that resemble results from modelling of spectra of nearby galaxies by Heavens et al. (2004). As mentioned in the introduction the inclusion

of some stochasticity is expected to improve the realism of the models. In the context of the amplitude of the fluctuations in star formation over time we note the following. By studying the ensemble of UV to $H\alpha$ flux ratios in star forming dwarf galaxies Lee et al. (2009) investigated the starburst mode of dwarf galaxies. They conclude that starbursts with amplitudes of ~ 4 above the quiescent mode, which last for about 100Myr and occur every 1-2Gyr, could explain the whole population. The majority of our models do not have starburst episodes that supersede 4 times the local time average (see Fig. 2.10).

Our dust model is rather simple. However, given the success in reproducing the optical colors of the observed galaxy population (after some fine-tuning of constants, see Fig. 2.6), along with the observations that partially support our dust model (see Section 2.5) we believe it captures some of the essentials of obscuration by dust. It also turns out that the distribution of z-band extinctions for our models looks rather similar to the values for the galaxy sample of Kauffmann et al. (2003a).

In terms of line emission Fig. 2.3 suggests that modelling $H\alpha$ and $H\beta$ is not sufficient for the modelling of optical colors. If GALEV treats line emission adequately, this model further tells us that line emission only has a second order effect on *integrated u,g,r,i,z*-band photometry of nearby galaxies ($M_r \leq 17$), but caution should be taken at higher redshifts since migration of strong emission lines between filter bands does cause color shifts. Future studies improving the accuracy of the estimation of emission line strengths are on the way (Győry et al., 2011) and will further improve the quality of stellar population models.

Given the limited sensitivity of u,g,r,i,z-band photometry to the IMF as shown in Fig. 2.2 we conclude that the IMF slope, and consequently the stellar mass, cannot be *measured* with integrated optical broad band colors of galaxies at least in the range explored here (single slope IMFs from 2.1-2.9, Salpeter=2.35). This result is expected considering that most light from a stellar population with a "normal" IMF comes from stars of a rather limited mass range that reside close to the main sequence turnoff, on the giant branches or that are supergiants.

Is the number of models sufficiently large? When determining galaxy properties along with errors from colors using, e.g., a Bayesian maximum likelihood, the density of models in color space is of importance. Judging from Fig. 2.7-2.9 our library is sufficiently large for this purpose except at the very edges of the grid if using (u-g) vs. (r-i) or (g-r) vs. (i-z). However, if more than two colors are used the required density of the model library increases and caution has to be taken. The errors in Fig. 2.10 do not appear to be underestimated, except for one galaxy falling outside the model grid, and the method we use thus seems to work properly even for 10 colors.

The galaxy spectra are rather poorly reproduced with our model library, as mentioned in Section 2.6.4 both due to issues with lines and the continuum, though a significant improvement with respect to SSP models is achieved. Spectral lines may be poorly reproduced due to the simple one parameter treatment of element abundances. We should on the other hand be able to adequately model the continuum, especially considering its close connection to colors. However, in the modelling of galaxy spectra it is often assumed that the continuum is unreliable due to, e.g., flux calibration issues, and continuum variations are therefore removed with polynomial fits (cf. Chilingarian et al., 2007; Koleva et al., 2009). It is thus not completely clear whether the poorly fitted spectra mainly reflect problems with the models or the observations.

2.7.2 Model predictions

It is well known that optical colors can be used to separate star forming galaxies from quiescent ones. However, metallicity and dust extinction also have major impact. Our models suggest that, by using optical colors only, it is possible to overcome the age-metallicity degeneracy, and to be able to determine these quantities separately over a surprisingly large

part of the parameter space (see Fig. 2.7-2.9). Furthermore, an interesting prediction of the model is that, to some extent, the amount of internal extinction can be measured using optical colors. Is this really the case? We expect extinction to have the strongest effect in edge on disk galaxies. We therefore selected two subsamples of galaxies, with high and low estimated extinction, respectively (Fig. 2.11). It does indeed look like the high extinction bin contains a lot more edge on disk galaxies than the low extinction bin and, moreover, dust is seen in many more cases in the high extinction bin. It thus appears as if our color based estimate is reasonable.

Fig. 2.12 shows a rather good agreement between spectroscopically and photometrically determined galaxy properties in terms of average ages, metallicities, effective extinctions, specific star formation rates, and mass to light ratios. The strong correlation between (i-z) and metallicity in the photometric model (Fig. 2.8 and 2.12) is not as pronounced in (i-z) vs. spectroscopic metallicity (Fig. 2.12), suggesting that this particular model prediction may not be robust. We note, however, that the correlation between (i-z) and metallicity is present in all models we have considered (see Table 2.1). The wavelength dependence of the luminosity weighting, i.e. the wavelength dependence of the relative contribution of light from young and old stellar populations, could influence the metallicity estimate. If the spectroscopic metallicities are based on strong absorption lines line like e.g. the Mg line at $\sim$ 5100Å, they are likely more influenced by young stellar populations and blue horizontal branch stars than the i and z-band which have effective wavelengths of 7472 an 8917Å. The source of the discrepancy in metallicity is thus not resolved.

As the amount of dust present is coupled to a galaxy's specific star formation rate in our model, galaxies with young stellar populations are often heavily obscured. The introduction of the prior (see Sect. 2.6.1) reduces the degeneracy between old and dust free and young and dusty galaxies. However, a small number of old galaxies (ages determined by spectroscopy) still have young stellar populations according to our photometric model (Fig. 2.12). Figure 2.13 reveals some systematic differences between the parameters derived from photometry and spectroscopy along with some scatter. However, deviations are to be expected given the large difference in the amount of information contained in the two kinds of data (5 data points along the spectral energy distribution for u,g,r,i,z with respect to $\sim$2000 for SDSS spectra). To probe galaxy properties with optical photometry thus stands as a viable option, especially useful when limited spectral information is available such as in the case of severe aperture bias. We would also like to point out that spectroscopically derived quantities are not necessary "correct" as model dependencies may be present.

An interesting result is that the newer CB11 models perform much worse than the BC03 models in reproducing the colors of the nearby galaxy population. We would like to point out that this is not the same as saying that the ingredients of the BC03 model are somehow better than the newer version. We speculate that the offsets in the CB11 models may be a backlash of trying to optimize the model for predictions over a larger wavelength range. In BC03 as well as CB11, models based on the empirical library of stellar spectra by Le Borgne et al. (2003) do improve the modelling with respect to models based on stellar atmosphere models of Lejeune et al. (1997). This suggest that more uncertainties are introduced through a complete modelling than through an empirical approach.

A subclass of galaxies at (g-r,i-z)=(0.4,0.0) can not be modelled by any of the models considered (see Fig. 2.11). Most of these galaxies are rather faint in the z-band ($< m_z > \sim$ 17.0 as compared to $< m_z > \sim$ 15.5 for the entire sample), which has led us to suspect that a part of this population could simply be an artifact caused by photometric errors. The fraction of galaxies with small z-band photometric errors $\sigma_{m_r} < 0.05$ in the region $(0.3 < (g - r) < 0.4, -0.05 < (i - z) < 0.05)$ is a factor of two smaller than for the overall sample. However, this is not sufficient to explain the entire population. An other explanation is that these galaxies are even more metal poor than the most metal poor models (see Fig. 2.8) or, alternatively, that the SSP models fail at low metallicity.

31

The star formation histories, along with average ages, metallicities and r-band optical depth shown in Fig. 2.10 look reasonable at first glance. A quiescently looking galaxy, which in fact does not have any emission lines in its SDSS spectra, should according to the models have some amount of recent star formation. However, non star forming models lie within the errors. We thus conclude that the model output is reasonably reliable – within the limits of broad band photometry – in providing information about a galaxy's star formation history and dust content.

2.8 SUMMARY

If an adequate range of star formation histories, chemical enrichments and dust obscuration are being considered, some of the currently available stellar population models perform well in reproducing the integrated optical u,g,r,i,z-band photometry of nearby galaxies (see Fig. 2.6). However, strong differences between the various models are seen and it is therefore necessary to carefully consider the choice of model before proceeding with the analysis. *Our preferred model library is available on request.* Optical broad-band colors are insensitive to the slope of the IMF, but can on the other hand put constraints on star formation histories, chemical enrichments, and dust extinctions as verified through a comparison with spectroscopic data. The accuracy of the constraint depends on the galaxy's position in color space. This is mainly due to overlap of reddened and dust free models in certain parts of the color space.

2.9 APPENDIX

2.9.1 Galaxy colors

We test the colors of the galaxy sample we use in this chapter against two independent samples derived from SDSS data. The first sample from Lisker et al. (2008); Janz and Lisker

(2009b) and Meyer et al. (in prep.), hereafter S1, consists of Virgo cluster galaxies for which colors are measured within 2 effective radii or 1 Petrosian radius. The second sample is from Hansson et al. (in prep)., hereafter S2, and consists of an essentially volume limited sample of galaxies brighter than $M_r \sim -16$ within 50Mpc. Colors for these galaxies are measured within 2.5Kron radii, as determined from the r-band image using SourceExtractor (Bertin and Arnouts, 1996). For these two samples as well as for the sample we use in this chapter, hereafter S3, (r-i) vs. (u-g) and (i-z) vs. (g-r) colors are given in Fig. 2.14. The general agreement is good, but differences are seen. S3 have on average higher values of (i-z) at (g-r)=0.7. We test whether this can be explained by the difference in how the magnitudes are computed by looking at the change in colors when adopting Petrosian magnitudes (PetroMag) instead of modelMags. The median change in (i-z) is -0.06mag and for the other colors it is between -0.02mag and 0.00mag. Because the definition of Kron magnitudes is similar to Petrosian magnitudes we conclude that this offset can be explained by the difference in magnitude definitions. S1 also have many more galaxies in the region around (g-r,i-z)=(0.6,0.0). We find that all these galaxies are fainter than about $M_r = -16$ and as such are therefore absent in S3.

2.9.2 Extinction

The extinction in u,g,r,i,z for a given extinction curve is computed solely using the effective wavelength of each filter response. This can introduce an error depending on the spectral slope over the different passbands. To asses the importance of this error we compute the difference for the S99P models. The errors in the amplitude of the extinction are at a level of $\leq 4\%$ and can thus safely be neglected. However, if emission lines are included the correction can in some cases be larger.

2.9.3 Constants in dust model

A_0, the constant that sets the star formation history independent amplitude of A_r, should be chosen so that the distribution of A_r values ranges from zero to the limit set by the reddest galaxies observed. A value of A_0=0.40 keeps the models within or close to the observed cloud of galaxies.

t_0, the constant that relates A_r to the star formation history should be chosen in accordance with the limit at 10^8yr chosen by da Cunha et al. (2010). We employ an exponentially dropping limit with an exponent of $s = 3 \cdot 10^8$yr.

m, governing the metallicity dependence of A_r is measured directly from the data presented in Engelbracht et al. (2008) resulting in $m = 1.7$.

k, the power index of the wavelength dependence of the effective extinction, is found to be around -0.7 in the work of Charlot and Fall (2000). However, a value of -0.7 makes the model cloud too narrow in (r-i) at (u-g)> 1.3. k can be modified for a better match between models and observations without violating the previously mentioned constraints. We therefore adjust k to -1.1.

2.9.4 Spectral fitting

The spectra are deredshifted using the redshift provided by the SDSS according to

$$\lambda_{rest} = \lambda_{obs}\sqrt{\frac{1 - v/c}{1 + v/c}} \qquad (2.7)$$

where λ_{rest} and λ_{obs} are the rest wavelength and observed wavelength, respectively, v is the velocity corresponding to the Doppler shift and c is the speed of light.
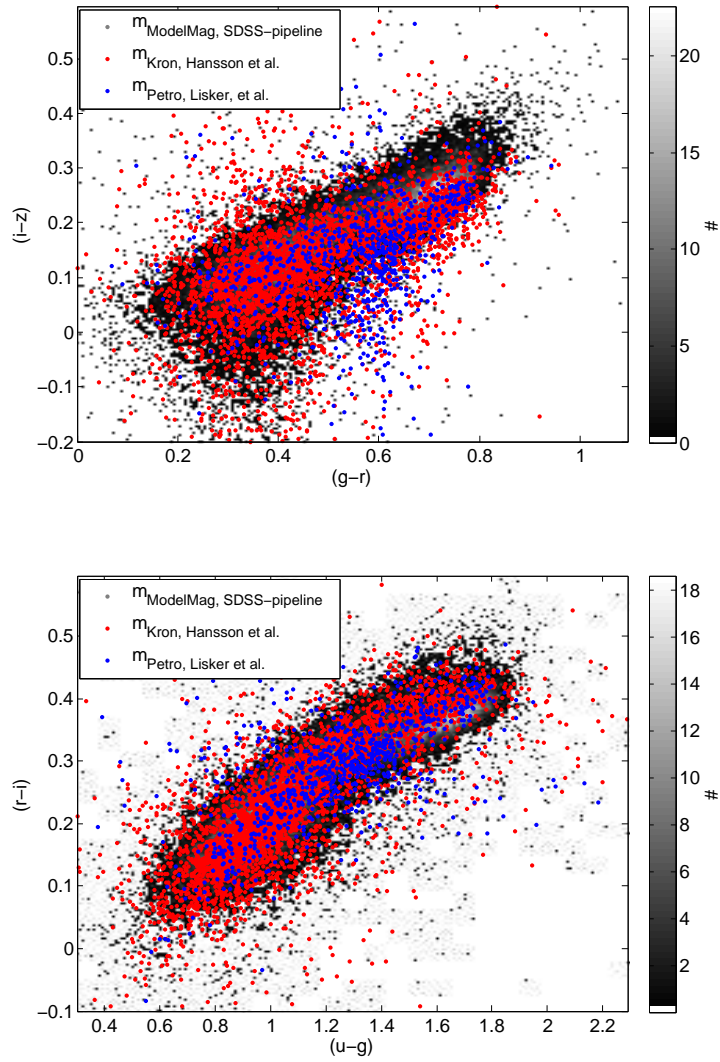
Figure 2.14: SDSS pipeline modelMags for the galaxy sample used in this chapter (grey 2D histogram), Kron magnitudes of SDSS galaxies from Hansson et al. (in prep.) and Petrosian magnitudes from (Lisker et al., 2008; Janz and Lisker, 2009b, Meyer et al. (in prep.)) in the $(r\text{-}i)$ versus $(u\text{-}g)$ and $(i\text{-}z)$ versus $(g\text{-}r)$ planes. All magnitudes were corrected for galactic foreground extinction.

The best models in our library of BC03hr spectra reproducing the data are found by means of calculating the reduced χ^2 between each model and the observations. In the fitting process we make use of the spectral region from 3700Å to 7000Å. Regions affected by the four brightest skylines (OI5577, OI6300, OI6354 and NaD5890) are masked out. The model library is at a slightly lower resolution ($\sigma_{mod} = 3\text{Å}/2.35$) than the data ($\sigma_{obs} \sim 2.5\text{Å}/2.35$ at $\lambda = 5000$Å) and we therefore degrade the resolution of the observed spectra to FWHM=3Å by convolving with a Gaussian with $\sigma = \sqrt{\sigma_{mod}^2 - \sigma_{obs}^2}$. As the model library is fairly large a direct fit to all models would be rather computationally expensive. We therefore carry out a two step fitting making use of binned models produced in the following way. The rms between one model and all other models is computed. The average of the 225 models[8] with the lowest rms is then computed, constituting the first binned model. The procedure is repeated but all models already included in the binned spectra are excluded. After 223 repetitions we have 223 binned models, each of which, except the last one, points to 225 other models. In the fitting procedure we first find the best binned model and secondly the best model in the bin. Such a fitting need not be equivalent to a χ^2 fit of all models since the best fitting model not necessarily needs to be contained in the best fit bin. Nevertheless, we find this approach preferable since it accelerates the fitting procedure by a factor of about 10^2.

Two things need to be considered before comparing the models with the observations, namely the line of sight velocity distributions of the stars and the emission lines. We assume that the former can be modelled by a Gaussian distribution. For each spectrum the minimum χ^2 is found after convolving the spectrum with Gaussians having dispersions from 100 to 285 km/s[9] in 12 logarithmically spaced steps. The procedure is repeated 25 times after having perturbed each pixel of the observed spectra with its errors. The best fit dispersion is taken to be

$$\sigma = \frac{\sum \sigma_i \exp(-\frac{1}{2}\chi_i^2)}{\sum \exp(-\frac{1}{2}\chi_i^2)} \qquad (2.8)$$

where σ_i is the best fit dispersion of the ith Monte Carlo realization, and where χ_i^2 is the lowest reduced χ^2 of the ith Monte Carlo realization.

The emission lines we consider in the fit are those 20 emission lines considered in Stoughton et al. (2002). These lines are expected to be the strongest in star forming galaxies according to the models of Anders and Fritze-v. Alvensleben (2003), and furthermore include the strongest emission lines expected due to AGN activity. For simplicity all 20 lines are masked out in the fit.

2.9.5 Bayesian maximum likelihood modelling

Assuming the errors are Gaussian the star formation history, stellar mass weighted stellar metallicity and effective extinction can be computed according to

$$a = \frac{\sum\limits_{i=1}^{i=n} \sum\limits_{j=1}^{j=m} w_i a_i e^{-\frac{1}{2}(\frac{c_{i,j} - c_{o,j}}{\sigma_{c_{o,j}}})^2}}{\sum\limits_{i=1}^{i=n} \sum\limits_{j=1}^{j=m} w_i a_i} \qquad (2.9)$$

where a is any of the properties mentioned above, i denotes a model, o an observation, c_j a color, $\sigma_{c_{o,j}}$ the error in an observed color and the summations are done over all n models and all m colors. The prior, i.e. the weights, w_i, are taken as the ratio of the number of

---

[8]The number of models in each bin was chosen for speed optimization ($\sqrt{50000} \sim 224$).

[9]A lower limit of 100km/s is adopted to avoid ending up with observations at higher resolution than the models at short wavelengths (SDSS spectra have $\delta\lambda/\lambda \sim 2000$). With an upper limit of 285km/s we can model all except some of the most massive galaxies in the Universe (Bernardi et al., 2007).

models in the library and the number of galaxies in the Guo et al. (2011) catalog[10] for bins[11] in M_r where the ratios are computed for models and galaxies within 0.1dex in stellar mass weighted age and 0.3dex in stellar mass weighted z of i. Figure 2.15 illustrates how the Bayesian approach influence the model grid in terms of age and metallicity.

---

[10]We only make use of the part of the simulation box known as milli-Millennium. The sample contains more than 50000 galaxies which ought to be sufficient.

[11]-24.5–22.5,-23.5–21.5,...,-18.5–16.5mag. Note that even in the absence of spectroscopic distances M_r can be estimated based on the observed galaxy structure.
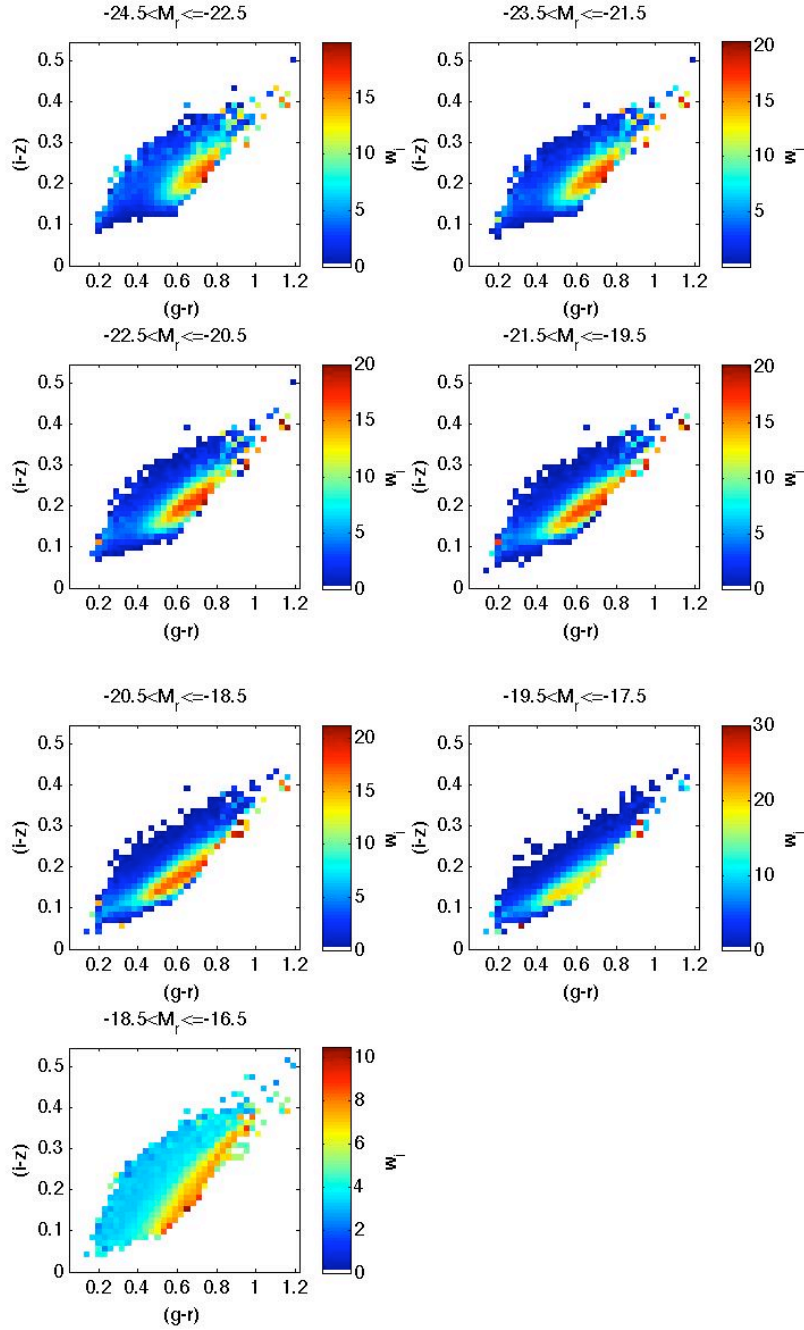
Figure 2.15: Distribution of Bayesian weights, w_i, in the $(i\text{-}z)$ vs. $(g\text{-}r)$ diagram (color coded pixels) for the seven bins in M_r adopted.

Chapter 3   Mass and environment

Galaxy properties are shaped by the mass of the galaxy as well as by several processes related to environment. In this chapter we take a closer look at an essentially volume complete sample of nearby galaxies with the aim of exploring how galaxy properties depend on mass and environment. Using the method outlined in Chapter 2 we derive stellar population ages and metallicities as well as specific star formation rates and stellar masses for almost 4000 galaxies for which u,g,r,i,z-band imaging are available from the SDSS. Additionally, axis ratios, half-light radii and morphologies are obtained and a galaxy group catalog is created based on linking lengths in redshift and on-the-sky position tuned to fit data from the Millennium simulation. All quantities except the axis ratios show a strong dependence on stellar mass. Relations with group mass at fixed galaxy stellar mass are also found for ages, metallicities, specific star formation rates and morphologies, but not for half-light radii and axis ratios. At fixed group mass and galaxy mass we find two characteristic features of the stellar mass function of groups that correlate with galaxy properties. Our findings also highlights that the typical stellar mass, m, of galaxies (with $m \geq 10^{9.7} M_\odot$) in groups increase with group mass, a feature which is important for the interpretation of apparent trends of galaxy properties with environment.

3.1   INTRODUCTION

The environment influences galaxies through a regulation of the gas supply needed for star formation (Gunn and Gott, 1972; Larson et al., 1980; Roediger and Hensler, 2005; Kereš et al., 2005) as well as through dynamical interactions (Moore et al., 1996, 1998; Mayer et al., 2001). These kind of processes have been used to explain observed correlations of galaxy properties with environment such as the morphology-density relation Dressler (1980) and the relative lack of star forming galaxies in groups and clusters (Weinmann et al., 2006). On the other hand, galaxy mass has been shown to correlate strongly with galaxy properties (Kauffmann et al., 2003b; Panter et al., 2007, 2008; Zhang et al., 2009; Bamford et al., 2009). These findings suggest that mass is a dominant driver behind galaxy formation and evolution.

It is worth pointing out that mass can be expressed using several different quantities but that we in this work focus on the stellar mass as this property can be derived from imaging data and correlates more strongly with other galaxy properties than luminosities.

The question about the relative importance of mass and environment in galaxy formation and evolution is often expressed as *nature* versus *nurture.* In order to separate the two several recent studies have focused on the effect of the environment at *fixed galaxy mass* (Kauffmann et al., 2004, Hansson et al. (submitted)[1]). A result of such studies is that lower mass galaxies are more easily affected by environmental processes (Bamford et al., 2009; Smith et al., 2011) which is expected given that the potential well in which the material reside is shallower.

---

[1]This paper, "Stellar population properties of galaxies in the WIde-field Nearby Galaxy-cluster Survey: dependence on galaxy intrinsic properties and environment", is a study of cluster galaxies using spectroscopic data and is not a part of this thesis.

As the (stellar) mass of a galaxy seems to be so important, an interesting question that follows is how the galaxy acquired its present (stellar) mass? Galaxies grow through two main mechanisms: merging and accretion. The former is related to environment as the abundance of galaxies and their orbital characteristics decides whether mergers occur. Gas accretion of course depends on the gas supply but also on the temperature and metallicity of the gas (Kereš et al., 2005). It seems reasonable to expect that these fundamental links between galaxy mass and environment ought to leave imprints on the galaxy mass function as a function of environment. We pursue a search for such features in this chapter. Previously, several authors have studied the behavior of the mass (or luminosity) function with group mass (Yang et al., 2009). In a series of papers (Tully et al., 2002; Trentham et al., 2006; Tully and Trentham, 2008; Chiboucas et al., 2009; Trentham and Tully, 2009) studied several nearby galaxy groups finding a diversity of R-band luminosity functions, including a steepening of the faint end slope for more rich groups (Tully et al., 2002), which may not be in seen galaxy samples that do not reach as faint absolute magnitudes (Croton et al., 2005).

In Chapter 2 we saw how the stellar mass can be derived using multi-wavelength optical imaging data. A measure of the environment has not yet been discussed in detail. Various ways of quantifying environment have been adopted in previous studies, including local galaxy number densities (Park et al., 2007), group membership (Weinmann et al., 2006) and cluster centric radii (Smith et al., 2011). For most data sets all methods suffer from the inherent weakness of using redshift as a distance indicator given the degeneracy between velocity and distance. In this chapter we study the effects of the environment using a galaxy group catalog and attempt to address the weakness of the method by considering several independent group properties. The best catalog of galaxy groups in the local Universe was for a long time Tully (1987), recently this work was superseded by Makarov and Karachentsev (2011). However, in this chapter, in contrast to Makarov and Karachentsev (2011), we make use of the power of the SDSS to derive accurate galaxy properties.

In this chapter we focus on how galaxy properties that can be derived from u,g,r,i,z-band imaging depend on the environment at fixed stellar mass. The novelty of this work is threefold. The sample we study has not been considered in detail due to issues with the SDSS pipeline for nearby galaxies. For this local sample ($\leq$50Mpc) we reach fainter magnitudes ($M_r = -16.0$) than most previous studies. The use of imaging data overcomes the aperture bias usually present in spectroscopic studies, particularly with fiber based spectroscopy like in the SDSS, though suffer from the drawback of lower information content concerning the spectral energy distribution.

This chapter is organized as follows. Section 3.2 deals with the photometric data and redshift we use. In Section 3.3 we describe how we obtained relevant galaxy properties from this data and in Section 3.4 relations with stellar mass are presented. Section 3.5 deals with the construction, quality and properties of our galaxy group catalog and presents how galaxy properties change with environment. Finally, our results are discussed in Section 3.6 and summarized in Section 3.7.

3.2   DATA

We base our study on imaging data and redshifts from the Sloan Digital Sky Survey (SDSS) data release 7 Abazajian et al. (2009), hereafter SDSS, supplemented by redshifts from either NED[2] or HYPERLEDA[3]. Moreover, we make use of the Millennium simulation (Springel et al., 2005), with accompanying galaxy catalogs from semi-analytic models (Guo et al., 2011). In particular we make use of data from milli-Millennium which is smaller version of the full simulation. The milli-Millennium volume is a cube where each side is $62.5h^{-1}$Mpc.

---

[2]The NASA/IPAC Extragalactic Database (NED) is operated by the Jet Propulsion Laboratory, California Institute of Technology, under contract with the National Aeronautics and Space Administration.

[3]HYPERLEDA database for physics of galaxies Paturel et al. (2003)

3.2.1 Initial sample selection

The spectroscopic catalog of SDSS is claimed to be complete down to $m_r = 17.77$ (although in Sec. 3.2.4 we will see that this is not completely true) corresponding to $M_r = -16$ at a distance of 50Mpc[4]. From the SDSS, NED and HyperLEDA catalogs we select all galaxies with velocities, v, less than 4000km/s[5] and Hubble law based absolute magnitudes brighter than -15 in any optical band provided as estimated using the cataloged photometry and redshifts. However, the catalogs overlap. As a staring point we use the SDSS and add objects from NED and thereafter HyperLEDA if these galaxies are not within 20" of a previous entry. For the galaxies included we manually select the best match in the SDSS photometric catalog using the SDSS navigate tool (typically this was chosen to be the object with the brightest r-band magnitude within the body of the galaxy.). To ensure that each galaxy only corresponds to one entry in our catalog we sort it by right ascension, examine all the galaxies visually and exclude all multiple entries, thus overcoming the problem of fragmented objects. For the remaining objects, now including galaxies without SDSS spectra, we have SDSS pipeline photometry[6] and velocity measurements. With these data we estimate r-band absolute magnitudes using the Hubble law and all objects with $M_r \leq -16.0$ are included in our initial galaxy sample consisting of 3915 galaxies.

3.2.2 Photometry

For large objects such as nearby galaxies the SDSS pipeline photometry suffers from poor sky subtraction and fragmentation, i.e. the division of a single galaxy into several objects, is common (Blanton et al., 2005; Lauer et al., 2007; Bernardi et al., 2007; Lisker et al., 2007; Blanton et al., 2011). We therefore make our own photometric measurements using the images provided by the SDSS. The Virtual Observatory tool SkyView (at http://skyview.gsfc.nasa.gov/) is used to retrieve u,g,r,i and z-band images, which are resampled into 300x300pixels with a pixel scale adjusted to the galaxy size ranging from 0.396-4.75"/pixel. In case the cutout consists of several SDSS fields we let SkyView add constants to the fields in order to set the difference in the median of the field boundaries to zero.

Next step is to make a sky subtraction which was performed as follows. Objects in the r-band images, which are the deepest, were detected using SourceExtractor (Bertin and Arnouts, 1996). The object masks (detection=1 else 0) constructed from the segmentation images provided by SourceExtractor were further expanded by Gaussian convolution (σ=2pix, new limit at a pixel value of 0.0005). The sky was taken as the mean of all unmasked pixels, clipped once at 3σ, and was subtracted from all images. Images were calibrated using the SDSS photometric zero-points, extinction coefficients and airmasses of the field closest to the image center.

Due to the large sample size an automated routine for the photometric measurements is preferred and for this purpose SourceExtractor (Bertin and Arnouts, 1996) was chosen. By telling SourceExtractor to use 0 as the sky and using the r-band image for object detection and estimation of the Kron (1980) radius, u,g,r,i and z-band magnitudes were measured within elliptical apertures of 2.5Kron radii. Note that these magnitudes are not a measure of the total object brightness, but ought to capture more than about 90% of the light for galaxies with light profiles that can adequately be described by the Sersic model (Graham and Driver, 2005). Fore- and background objects were masked out prior to the photometric measurements. The images along with masks and apertures used for the photometric mea-

---

[4]Throughout this work we adopt $H_0 = 71$km/s.

[5]The velocity limit was chosen to be greater than 3550km/s to allow for some velocity dispersion at a distance of 50Mpc. No cluster is located at this distance in the SDSS field and galaxies that deviate from the Hubble flow are therefore expected to be included in our sample.

[6]50 galaxies lack any photometry from the SDSS, but images are available. These were visually examined and assigned suitable r-band magnitudes.

surements were visually inspected and the masking was improved if we found it necessary. Corrections due to Galactic extinction were made based on the dust maps of Schlegel et al. (1998). Photometric errors were initially estimated following the prescription by Lisker et al. (2008). A comparison of photometry for galaxies in common with Lisker et al. (2008); Janz and Lisker (2009b) and Meyer et al. (in prep.) can be found in the Appendix 3.8.1. Despite that we use the same source of data we find standard deviations of about 0.06mag in g,r and i, 0.09mag in z and 0.15mag in u. However, the discrepancy can be attributed to differences in the method adopted as explained in more detail in Appendix 3.8.1. Nevertheless, these standard deviations ought to be a better estimate of the magnitude errors, $\sigma_{u,g,r,i,z}$, than our initial estimate which predicts significantly smaller errors. We therefore adopt σ_u=0.15mag, $\sigma_{g,r,i} = 0.06$mag and σ_z=0.09mag throughout.

3.2.3 Velocity

In this study all distances are computed using the Hubble law. An appropriate reference frame for distance measurements using radial velocities of galaxies within 50Mpc is the restframe of the local supercluster. Starting off with all galaxies in SDSS with heliocentric velocities lower than 4000km/s we corrected the redshifts to the rest frame of the local supercluster following Tully et al. (2008) according to:

$$\Delta v = V_{apex}[\sin(b)\sin(b_{apex}) + \cos(b)\cos(b_{apex})\cos(l - l_{apex})] \qquad (3.1)$$

where b and l are the galactic longitude and latitude of the galaxy as computed from the equatorial coordinates using the iraf/galactic task, $l_{apex} = 93$, $b_{apex} = -4$, and $V_{apex} = 316$km. Note that by correcting the velocities to the rest frame of the local supercluster we correct for the rotation of the Milky way and the infall of the local group towards the Virgo cluster. The corresponding distances will be reconsidered in Sec. 3.5 for galaxies in groups where velocities with respect to the restframe can be substantial.

3.2.4 Sample completeness

Despite the claims that the spectroscopic catalog of SDSS should have an incompleteness of only 4% the inclusion of NED and HyperLEDA objects increases our sample by about 30%. Part of this discrepancy can be attributed to issues with the SDSS pipeline photometry which was used for target selection. As a test all galaxy groups we detect (see Sec. 3.5) were visually inspected using the SDSS Navigate tool (at www.sdss.org). The Virgo cluster and seven other groups are excluded from our catalog due to high incompleteness. These group are affected by either the velocity cut at 4000km/s, the edge of the survey area, or simply by a lack of spectroscopic measurements. The Virgo cluster, however, is instead excluded because is located nearby and has a high velocity dispersion leading to large errors in the initial estimation of absolute magnitudes. In general, errors in the absolute magnitude estimates due to inaccurate photometry or large peculiar motion will cause some incompleteness close to the faint end limit of our sample and will considered in Sec. 3.5. However, the overall incompleteness is not so severe. For the remaining groups that we inspected we find that 96% of all potential group members *brighter* than $M_r = -16$ are included.

Our study focus on how mass and environment influence galaxies. To avoid an incompleteness in stellar mass, we limit our sample to galaxies that have a stellar mass of at least $10^{8.7}$M$_\odot$. This particular limit was chosen considering the distribution of stellar population ages described in the following Section. Old galaxies are missing at lower masses which is most likely caused by the magnitude limit of the sample.

3.3 GALAXY PROPERTIES

3.3.1 Stellar population properties

We derive stellar population properties by fitting all observed colors from u,g,r,i,z-band photometry to the recommended model library described in chapter 2. These models are constructed through linear combinations of single stellar populations from Bruzual and Charlot (2003) for a large range of star formation histories and metallicities, and includes modeling of emission lines based on the work by Kotulla et al. (2009) as well as a simplistic treatment of obscuration by dust (see chapter 2). As the initial mass function (IMF) is insensitive to u,g,r,i and z-band photometry a Chabrier (2003) IMF is used throughout (see Bastian et al. (2010)).

The parameters we adopt in this study to characterize a galaxy's stellar population are the stellar mass[7], m, stellar mass weighted age, t, stellar mass weighted metallicity, Z, as well as the specific star formation rate, $SSFR$, i.e. the star formation per unit stellar mass. Values and errors of the derived parameters are estimated using a Bayesian likelihood analysis (see chapter 2) to impose realistic model constraints. Assuming Gaussian errors we have that

$$ t = \frac{\sum_{i=1}^{i=n} \sum_{j=1}^{j=m} w_i t_i e^{-\frac{1}{2}\left(\frac{c_j - cm_{i,j}}{ec_j}\right)^2}}{\sum_{i=1}^{i=n} \sum_{j=1}^{j=m} w_i t_i} \tag{3.2} $$

where the summations are done over all n models, i, and all $m=10$ colors, j, and where c_j is the observed color with an error, ec_j, $cm_{i,j}$ is the model color and w_i is a weight. The latter is chosen as the ratio of the number of galaxies in the Guo et al. (2011) catalog and the number of models in the library, where both quantities are computed in bins of M_r, stellar mass weighted age and stellar mass weighted metallicity. A weight, w_i, thus reflects a prior probability that the model, i, is a good representation of the observation (see Sec. 2.6.1 and 2.9.5).

Fig. 3.1 show a comparison between the r-band mass to light ratios obtained using our method with power law fits to $(u$-$r)$, $(g$-$r)$, $(r$-$i)$ and $(i$-$z)$ from Bell et al. (2003). Some amount of scatter is seen, but the main difference is a change in slope causing differences in r-band mass to light ratio of up to 0.15dex.

3.3.2 Structural properties

As a measure of galaxy sizes we make use of half-light radii, r_{50}. This parameter is estimated using the SourceExtractor FLUX_RADIUS parameter. The values of r_{50} in pixels are converted to kpc using the pixel scale and the distances derived from radial velocities. The error in r_{50} is taken to be 11% based on results presented in chapter 4. We also use SourceExtractor to measure the ratio of the semi major axis, a, and the semi minor axis, b, for which we estimate errors of 11% in analog with the half-light radii. These properties are computed from the r-band image moments of all pixels above the detection threshold of 24mag/arcsec^2 for the objects in question. Through a visual inspection of SDSS color composite images (at www.sdss.org) we performed a morphological classification of the galaxies in our sample. The objects were classified either as late-type (including spiral and irregular galaxies) or early-type (including elliptical and lenticular galaxies)[8]. These classifications are parameterized using the variable M_{type} where late-types and early-types correspond to $M_{type} = 0$ and $M_{type} = 1$, respectively. The error in this classification is estimated as the

---

[7]We define stellar mass as the sum of all mass presently in stars and stellar remnants.
[8]Dwarf galaxies are also placed in either of the two classes.

;
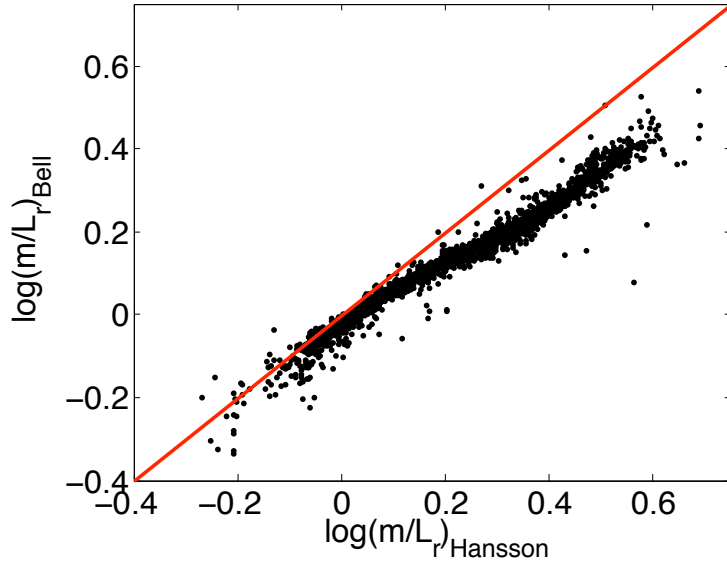
Figure 3.1: A comparison between r-band mass to light ratios, m/L_r, based on the models presented in chapter 2 and the mean of (u-r), (g-r), (r-i) and (i-z) estimates based on Bell et al. (2003) with a Kroupa et al. (1993) IMF for our initial sample of galaxies (black dots). The red line shows the 1:1 relation.

average error in a similar classification performed in the Galaxy Zoo project (Lintott et al., 2008, 2011) for ~ 1000 galaxies in common with our study. As multiple classifications of the same object differ in on average 15% of the cases we take the error to be 0.15 in M_{type}. Despite that the classifications are discrete expressing the errors in this manner is useful when studying a population of objects.

3.4 STELLAR MASS DEPENDENCE

Fig. 3.2 shows how the stellar mass weighted ages, t, stellar mass weighted metallicities, Z, half-light radii, r_{50}, specific star formation rates, $SSFR$, axis ratios, a/b and morphological types, M_{type}, depend on galaxy stellar mass. We fit 3rd order polynomials to the data for *isolated* galaxies, i.e. galaxies not residing in groups (see Sec. 3.5), at $m < 10^{11} \mathrm{M}_\odot$ and to *all* galaxies at higher masses. These fits reproduce the average relations as a function of mass very well and the coefficients of the polynomials can be found in Table 3.1. Strong dependencies are seen in almost all cases with more massive galaxies being on average older, more metal rich, larger, less star forming and are of earlier morphological type than lower mass galaxies. The exception is the axis ratio which only exhibits a mild dependence on mass where galaxies with $m \sim 10^{9.5} \mathrm{M}_\odot$ appear to have the highest axis ratios.

We denote the difference between t, Z, r_{50}, $SSFR$, a/b, M_{type} and the polynomial fits with Δt, ΔZ, Δr_{50}, $\Delta SSFR$, $\Delta b/a$ and ΔM_{type}, respectively. These values thus measure the difference in the galaxy properties with respect to the local stellar mass average.

3.5 GALAXY GROUPS

In this section we present how we construct a group catalog based on the galaxy sample and measurements described in the previous sections. The main part thereafter deals with our investigation of how galaxy properties are influenced by the group environment.
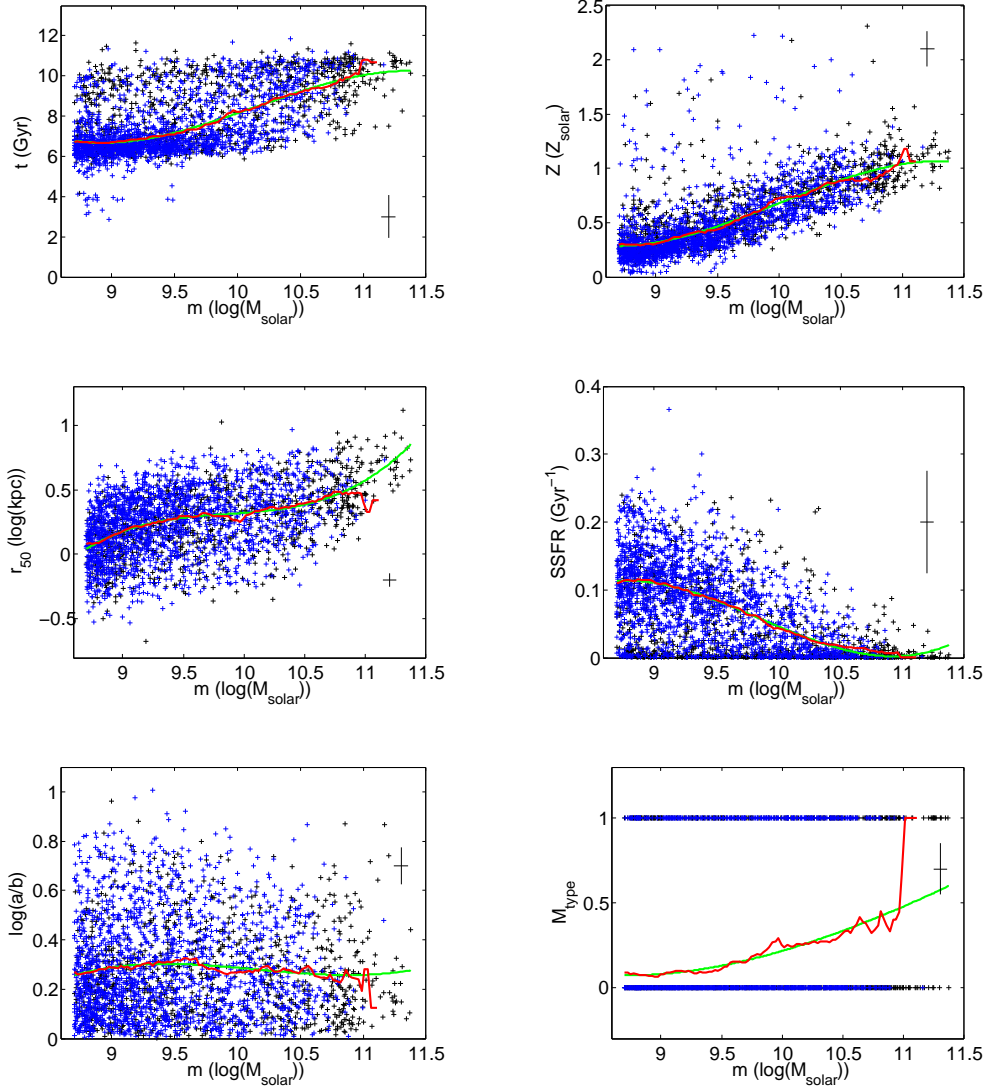
Figure 3.2: Stellar mass weighted age, t, stellar mass weighted metallicity, Z, half-light radius, r_{50}, specific star formation rate, $SSFR$, axis ratios, a/b and morphological type, M_{type} versus galaxy stellar mass, m, for isolated galaxies (blue crosses) and for galaxies residing in groups (black crosses). The red lines shows the mean trends computed using a bin width of 0.3dex in stellar mass. Green lines show 3rd order polynomials fitted to the isolated galaxies below a stellar mass of $10^{11}M_\odot$ and to the all galaxies at higher masses. Polynomial coefficients are given in Table 3.1. Errorbars indicate the median errors for isolated galaxies.

Table 3.1: Polynomial coefficient of mean relations with stellar mass, m, on the form: $Y = p_1 m^3 + p_2 m^2 + p_3 m^1 + p_4$.

Y	p_1	p_2	p_3	p_4
t (Gyr)	-0.4944	15.05	-150.4	502.2
Z ($Z_\odot$)	-0.08764	2.627	-25.79	83.58
r_{50} (log(kpc))	0.1274	-3.767	37.19	-122.3
$\log(a/b)$	0.02271	-0.6713	6.537	-20.90
SSFR (Gyr^{-1})	0.02271	-0.6713	6.537	-20.90
M_{type}	-0.008603	0.3211	-3.634	13.04

3.5.1 Group finding

The main observables relevant for determining group properties are galaxy positions, redshift and magnitudes. As gravity is the force behind the clustering of galaxies we chose to replace magnitudes with total galaxy masses. Taking such a step inevitably leads to uncertainties because the total galaxy mass, M, can not be measured with the data at hand. However, the use of total masses provides a more physical foundation. We therefore estimate total masses based on galaxy stellar masses following the prescriptions given in Moster et al. (2010). This paper provides stellar to dark matter mass ratios based on observed stellar mass functions (Panter et al., 2007) and dark matter halo mass functions from simulations (Springel et al., 2005). Note that absolute magnitudes, and hence stellar masses, are distant dependent and that an additional uncertainty is therefore introduced.

A simple but powerful way of determining group membership is the use of linking lengths in redshift, $l(M)$, and on the sky position, $r(M)$, (Huchra and Geller, 1982). If a galaxy is within the linking lengths of a second galaxy then the two belong to the same group. To determine group membership is a task of trying to determine whether or not galaxies are gravitationally bound. For this task the escape velocity, v, is a useful quantity. At a distance, r, from a point source of mass, M, we have

$$v = \sqrt{\frac{2GM}{r}} \tag{3.3}$$

where G is the gravitational constant. Moreover, the radius r from a point mass M corresponding to a constant force per unit mass, F, is

$$r = \sqrt{\frac{GM}{F}} \tag{3.4}$$

Based on Eq. 3.3 and 3.4 we think it is reasonable to use linking lengths in line of sight velocity and on the sky position which are proportional to $\sqrt{M}$

$$l(M) = k_l \sqrt{\frac{M}{10^{11} M_\odot}} \tag{3.5}$$

$$r(M) = k_r \sqrt{\frac{M}{10^{11} M_\odot}} \tag{3.6}$$

where k_l and k_r are constants which we tune to fit model data from the milli-Millennium simulation.

An additional constraint was imposed on the group finder to prevent it from connecting neighboring structures too easily, namely that each galaxy can only link to the most massive galaxy within the linking lengths.

The constants were tuned in the following way. We placed three observers in the middle of three, non parallel, sides of the milli-Millennium data cube. Sky positions and line of sight velocities as seen by the observers are calculated for all galaxies with $M_r \leq -16$. This particular limit was chosen to match our observational sample of SDSS data. Our group finder is applied to the Guo et al. (2011) milli-Millennium data. For each group, we assume that all group members reside at a distance from the observers corresponding to the mass weighted average redshifts of the group members, where the redshifts are calculated as the sum of the velocity corresponding to the expansion of the Universe and the galaxy's motions with respect to the observer. This assumptions thus leads to updated galaxy distances for group members as seen by the observers. We then compare these new distances, $d_{i,group}$, with the physical distances, $d_{i,real}$ for each galaxy, i. We can evaluate if the procedure has improved the distance measurements for group members using the quantity, Φ.

$$\Phi = \frac{1}{n} \sum_{i=1}^{i=n} |d_{i,group} - d_{i,real}| \tag{3.7}$$

where n is the total number of galaxies residing in groups. After testing a large number of possible linking length we find that maximal performance, i.e. a minimum value of Φ, is achieved by k_l=80km/s and k_r=0.04Mpc. These values were used for the observational sample as well. We let our group finder run on the observed galaxy sample which produces a galaxy group catalog. Eight of the groups are removed from the catalog due to incompleteness as discussed in Sec. 3.2.4. The distances to the galaxies in the groups are updated based on the assumption that all group members are located at the same distance and corresponding corrections to the galaxy's stellar masses are performed. The final group sample which we study in this chapter consists of 91 groups with at least three members each.

3.5.2 Group properties

Several independent properties characterizing galaxy groups are their total stellar mass, m_g, total mass, M_g, velocity dispersion, σ, mean galaxy separation, r_g, group axis ratios, $(b/a)_g$, and the difference in stellar mass between the two most massive galaxies, Δm. In combination with the galaxy mass functions these are the quantities we use in our study of galaxy groups and their influence on galaxy properties. We calculate M_g using the stellar-to-halo mass relation of Moster et al. (2010) applied to the most massive group members treating this galaxy as a *central* (see e.g. Moster et al., 2010). We estimate the velocity dispersion simply as $\sigma = \sqrt{(1/(n-1)) \sum_i (v_i - <v>)^2}$ where v_i is the velocity of group member i and the total number of group members is n. This estimate is of course not very accurate for groups with just a few galaxies, although σ turns out to correlate well with the stellar mass as we will see. Finally, galaxy group axis ratios are computed as in Tovmassian and Plionis (2009), i.e., as the ratio of the eigenvalues of the inertia tensor, I

$$I_{11} = \sum m_i(r_i^2 - x_i^2) \tag{3.8}$$

$$I_{22} = \sum m_i(r_i^2 - y_i^2) \tag{3.9}$$

$$I_{12} = I_{21} = -\sum m_i x_i^2 y_i^2 \tag{3.10}$$

where x_i and y_i are orthogonal galaxy coordinates on the plane of the sky with (x,y)=(0,0) in the mass weighted group center, r_i is the distance of the ith galaxy from the group center of mass and the stellar masses of the galaxies, m_i, are used as weights. Note that this typically leads to very small axis ratios for groups where a small number of galaxies dominate in mass.

Fig. 3.3 illustrate how the group properties introduced above depend on m_g. As expected correlations with group mass are seen: 1) σ increase with stellar mass 2) more massive groups

are rounder 3) more massive groups are larger 4) more massive groups have larger dark to stellar mass ratios 5) the difference in stellar mass between the two brightest galaxies in the group decrease with increasing stellar mass.

3.5.3   Quality of group catalog

Our tests on the milli-Millennium simulation show that the assumption that all group members are located at the same distance decreases the difference between the physical and estimates distances for group members by 40%. This is a significant improvement, although the degeneracy between distance and velocity still puts significant limitations on the accuracy of redshift based distances.

The SDSS group catalog by Yang et al. (2007) starts at $z = 0.01$ and some of our groups are included in this work. We make a positional match of the two catalogs allowing a $0.2°$ offset in sky position (~ 0.2Mpc at z=0.01) of the mass weighted group centers which yields 17 groups in common with stellar mass estimates by Yang et al. (2007). In Yang et al. (2007) dark matter halo masses are estimated using a ranking of completeness corrected integrated luminosities, or stellar masses, of all group members. Figure 3.4 shows a comparison between the total stellar and the (stellar mass based) dark matter halo masses for these groups. Our group mass estimates are on average higher both in stellar mass and halo mass. Considering that Yang et al. (2007) only take galaxies brighter than $M_r = -19.5$ into account the agreement is rather good in stellar mass. However, the halo masses appear to be systematically higher in our data, especially at the high mass end.

3.5.4   Galaxy properties versus group mass

Figure 3.5 shows the average values of Δt, Δz, Δr_{50}, $\Delta SSFR$, $\Delta b/a$ and ΔM_{type} for all galaxies in the groups plotted against the total stellar mass of the groups. We would like to point out that due to the use of an average these quantities will to a larger extent probe low mass galaxies as these are more abundant. We estimate errors in the parameters, σ_g, as the standard deviations with respect to the average relations in Fig. 3.2 multiplied by $N^{-1/2}$ where N is the number of galaxies in the group. We performed weighted least square fits of straight lines to the data using $1/\sigma_g^2$ as weights and addressed the errors in the fits through Monte Carlo simulations. The functional form used is the simplest quantitative parameterization possible and is motivated by the limitations of the sample in terms of size and errors.

Galaxies in more massive groups are on average more metal rich (4.7σ), older (7.4σ), form less stars (5.3σ) and are of earlier morphological types (11σ), but we do not see any relation with galaxy sizes or axis ratios. Some intrinsic scatter around the best fit relations are present, except for Δr_{50}. The low mass end of all relations are consistent with zero, i.e. with the average properties of isolated galaxies, but the lowest mass groups do deviate from the trend in some cases. They appear to be younger, less metal rich, form stars at a higher rate and be of later morphological type than isolated galaxies.

3.5.5   Stellar mass functions

Stellar mass functions for groups in bins of the group stellar mass are shown in Fig. 3.6. The mass functions have been convolved with a Gaussian kernel as indicated in the figure to reduce noise. The figure highlights that most of the stellar mass in groups are contained in the most massive group members. The mass distribution of isolated galaxies are on the other hand more extended. Figure 3.6 also shows that if giants are considered ($m > 10^{9.7} M_\odot$, Kannappan et al. (2009)), the median galaxy mass increases with increasing group mass, which amounts to a difference of about 0.5dex between galaxies in isolation and galaxies in groups with stellar masses above $10^{11} M_\odot$. Consequently, any observed trend of galaxy
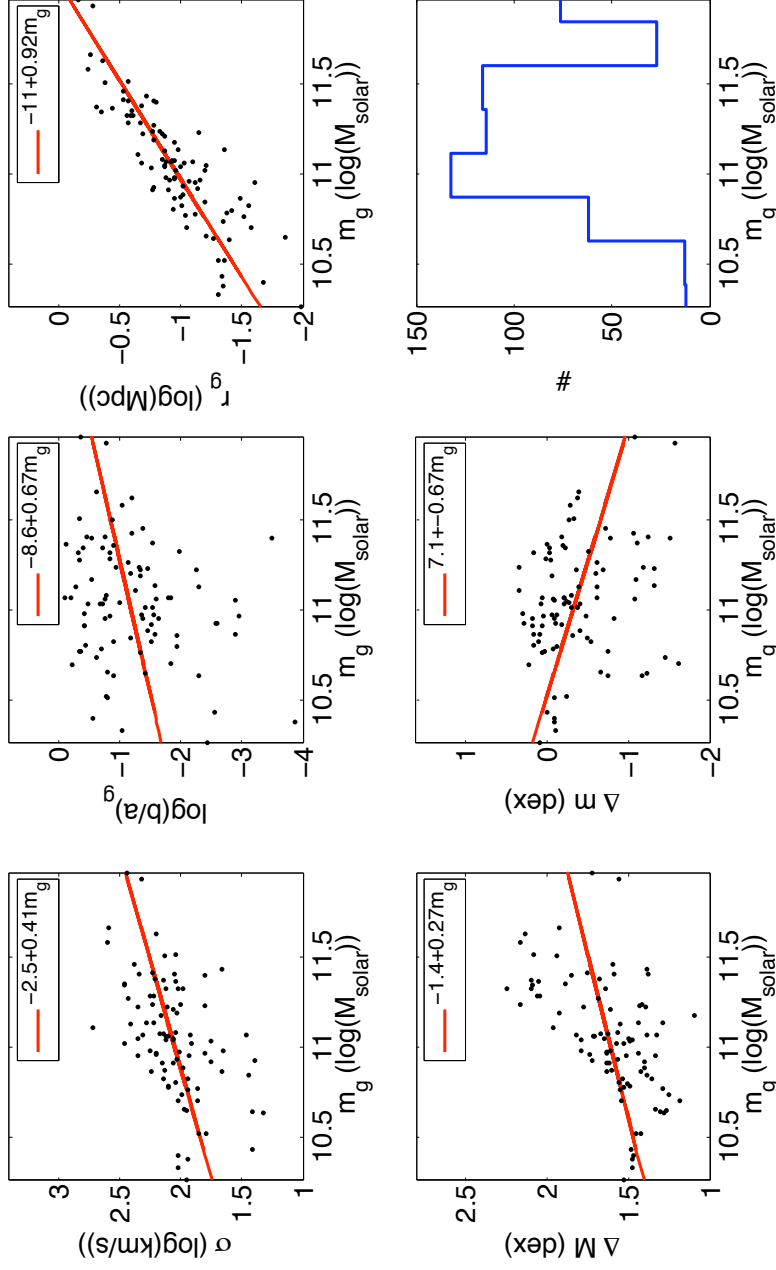
Figure 3.3: Velocity dispersion, σ, group axis ratios, $(b/a)_g$, mean galaxy separation, r_g, difference between total and stellar mass, ΔM, and difference in stellar mass between the two most massive group members, Δm, versus total stellar mass for galaxy groups. The red lines show least square fits of straight lines to the data. The lower right panel shows a histogram of the total number of group galaxies as a function of group stellar mass (blue line).
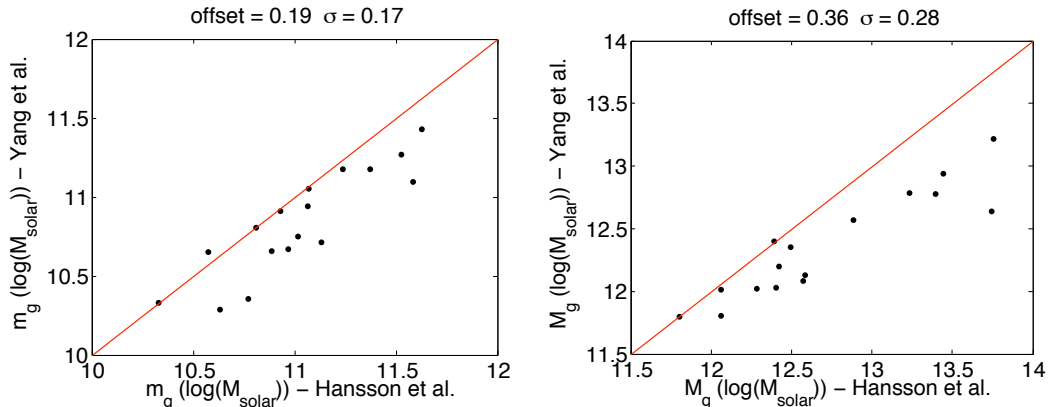
Figure 3.4: A comparison of the total stellar mass, m_g, (left) and dark matter halo mass, M_g, (right) for groups in common with Yang et al. (2007). The red line shows the 1:1 relation. One of the 17 groups have not any stellar mass based dark matter halo mass estimate from Yang et al. (2007) and are excluded in the right hand panel.

properties versus galaxy group mass/environment will be strongly influenced by a change in the typical stellar mass of the galaxies.

Throughout the rest of this section we will look at how the stellar mass function changes with galaxy group properties as well as the properties of the galaxies that reside in these groups. This is done in the following way. For each property we consider, like e.g. the velocity dispersion, we make the following steps.

1) Divide the groups into two bins depending on whether they are above or below the best fits shown in Fig. 3.3 and 3.5.

2) The combined mass functions for the two ensembles of groups are calculated.

3) These are then normalized by their total mass, thereby allowing a fair comparison of the two.

4) The normalized mass function for the ensemble of groups with low parameter values are subtracted from the corresponding normalized mass function for the ensemble with high parameter values.

5) The difference is thereafter evaluated in terms of the Poisson errors in the galaxy number counts.

The procedure outlined is meant to allow a fair comparison between the mass functions of galaxy groups with specific properties at a fixed group mass. Whether this is the case does to some extent depend on whether the mass distribution of groups above and below the best fits are similar.

The differences between the various mass functions are typically not very large in comparison with the errors. To enhance the signal to noise we divide the galaxies into three mass regimes: dwarfs ($m < 10^{9.7}$), low mass giants ($10^{9.7} <= m <= 10^{10.5}$) and high mass giants ($m > 10^{10.5}$). These particular mass limits are motivated by the studies of Kauffmann et al. (2003b); Kannappan (2004); Kannappan et al. (2009) who find that galaxy properties change dramatically around these masses. As the number of high mass giants are small the errors in the stellar mass contained in these bins are computed as the errors of the two lower mass bins added in quadrature. This can be done since the total mass difference should be zero due to the normalization. The results are shown in Fig. 3.7 and 3.8, and we comment on individual features below. In the following we ignore the lowest mass bin ($m < 10^{8.9} \mathrm{M}_\odot$) which seems to be affected by incompleteness (see also Sec. 3.2.4).

Groups with a large total to stellar mass have a smaller mass fraction in low mass giants
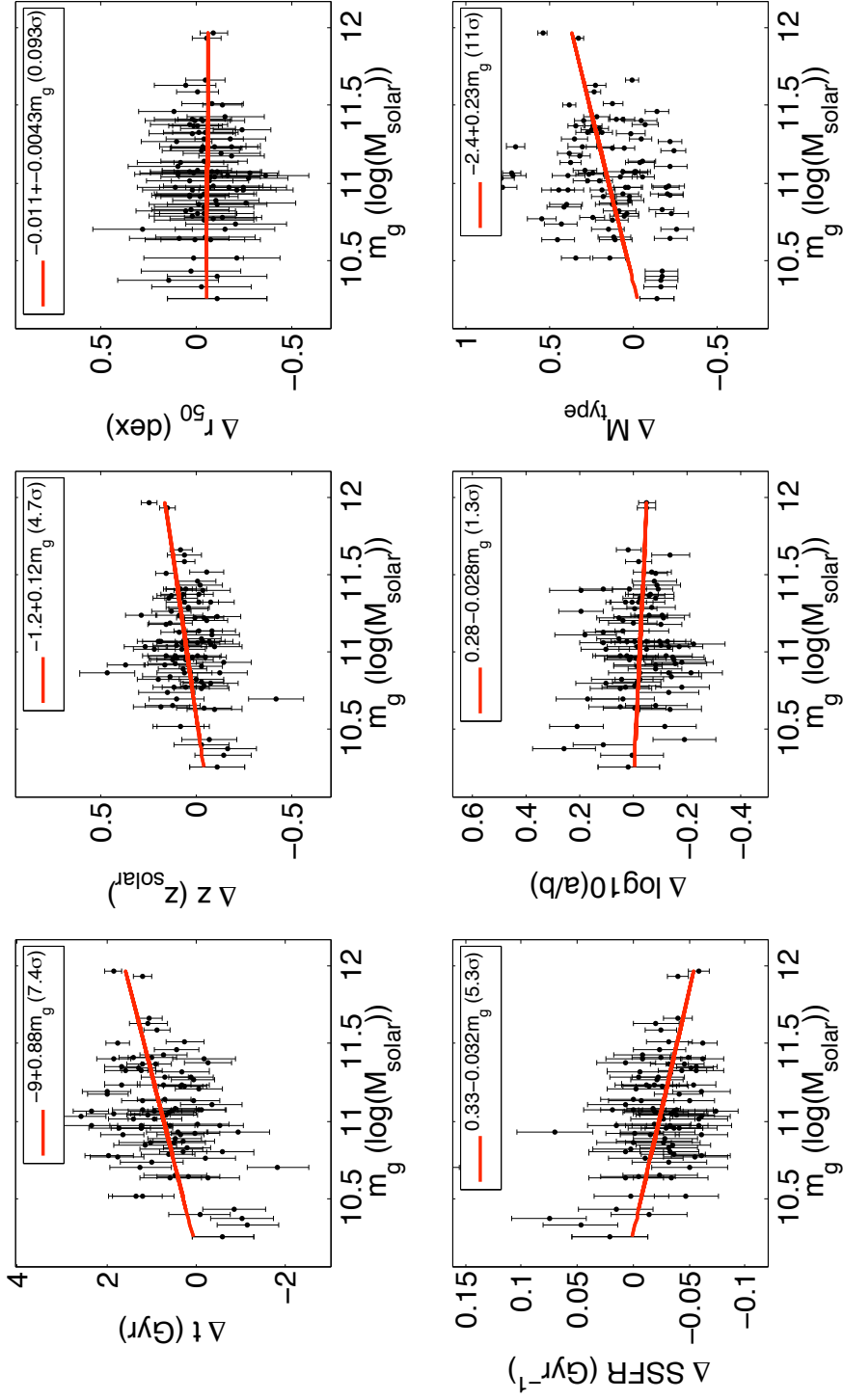
Figure 3.5: Offsets from the mean relations of galaxy properties versus stellar mass (see Fig. 3.2) averaged over all members of the group versus the total stellar mass of the group. The properties considered are the group average offsets in stellar mass weighted age, Δt, stellar mass weighted metallicity, ΔZ, half-light radius, Δr_{50}, specific star formation rate, $\Delta SSFR$, axis ratio, $\Delta a/b$, and morphological type, ΔM_{type}. The red lines show the results of error weighted least square fits and the statistical significance of the slopes are indicated.
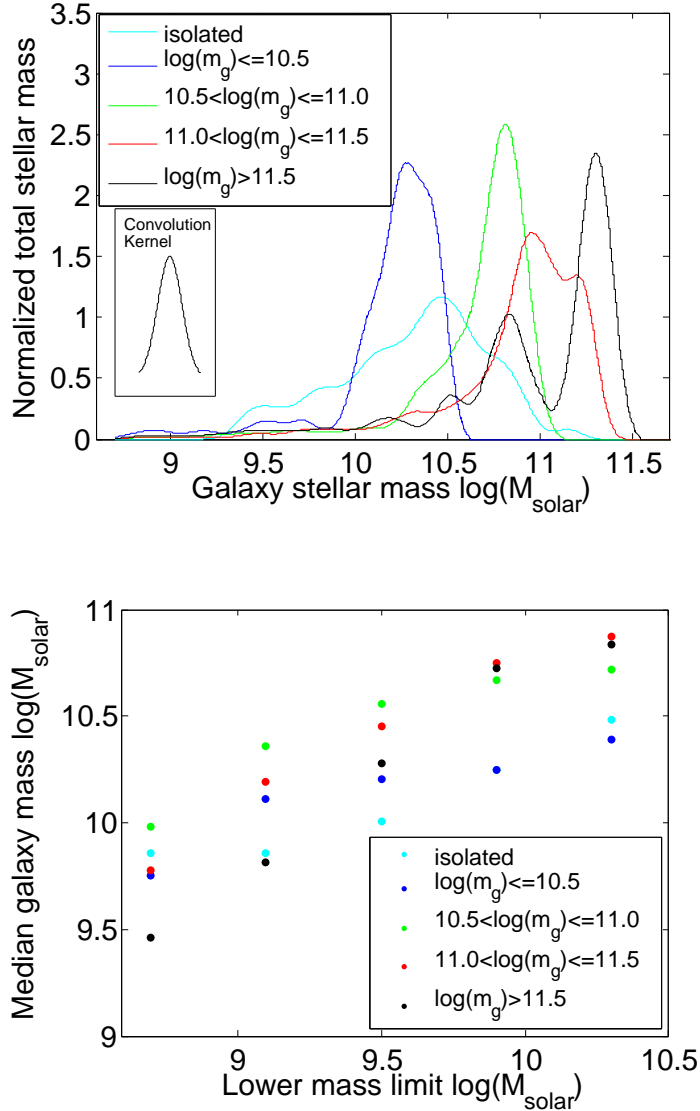
Figure 3.6: **Top panel:** Normalized total stellar mass versus galaxy stellar mass for isolated galaxies (cyan) and for galaxies in groups of various total mass (blue, green, red and black). The area under any of the curves indicate the normalized stellar mass in any range considered. The mass functions have been convolved with a Gaussian kernel as indicated in the figure to reduce noise. **Bottom panel:** Median stellar mass of galaxies in isolation (cyan) and of galaxies in groups of various total mass (blue, green, red and black) as a function of the lower mass limit adopted. The cyan and blue points overlap at a lower limit of $10^{9.9} M_{\odot}$.
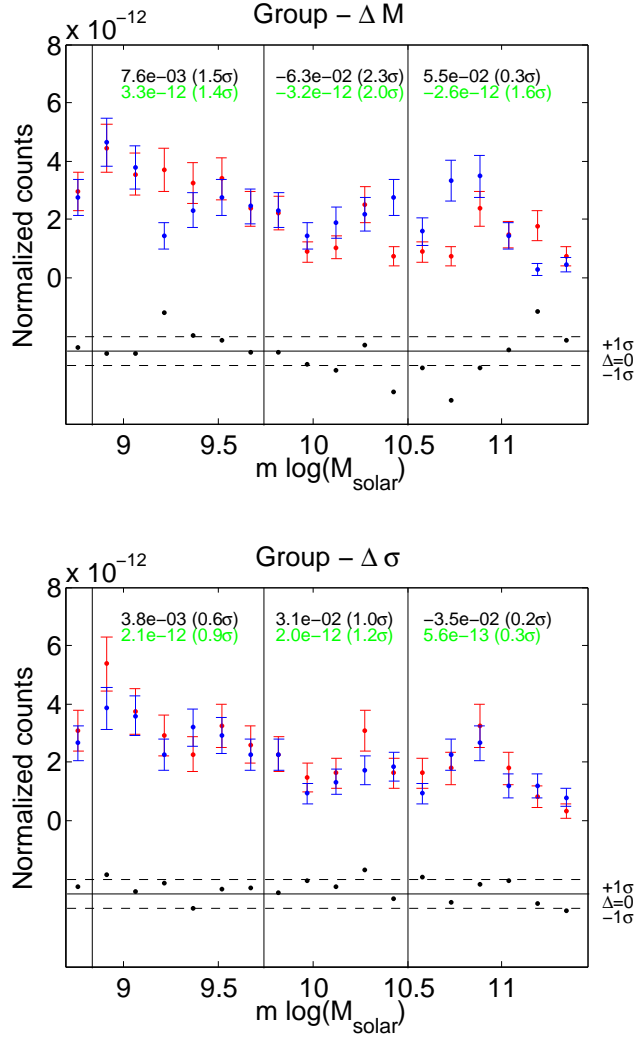
Figure 3.7: Stellar mass functions of groups above (red) and below (blue) the mean relations of group properties as a function of the total stellar mass of the group (see Fig. 3.3), where the mass functions have been normalized by the total stellar mass to allow a fair comparison. The group properties considered are the difference between the total and the stellar mass, ΔM, and the velocity dispersion, σ. The difference between the two mass functions in each panel are indicated in units of the standard deviation (black dots). The black vertical lines separates dwarfs, low mass giants and high mass giants for which the differences in numbers (green) and masses (black) between the two mass functions are indicated. The lowest mass bin ($m < 10^{8.9} M_\odot$) have been excluded because it is likely affected by incompleteness.
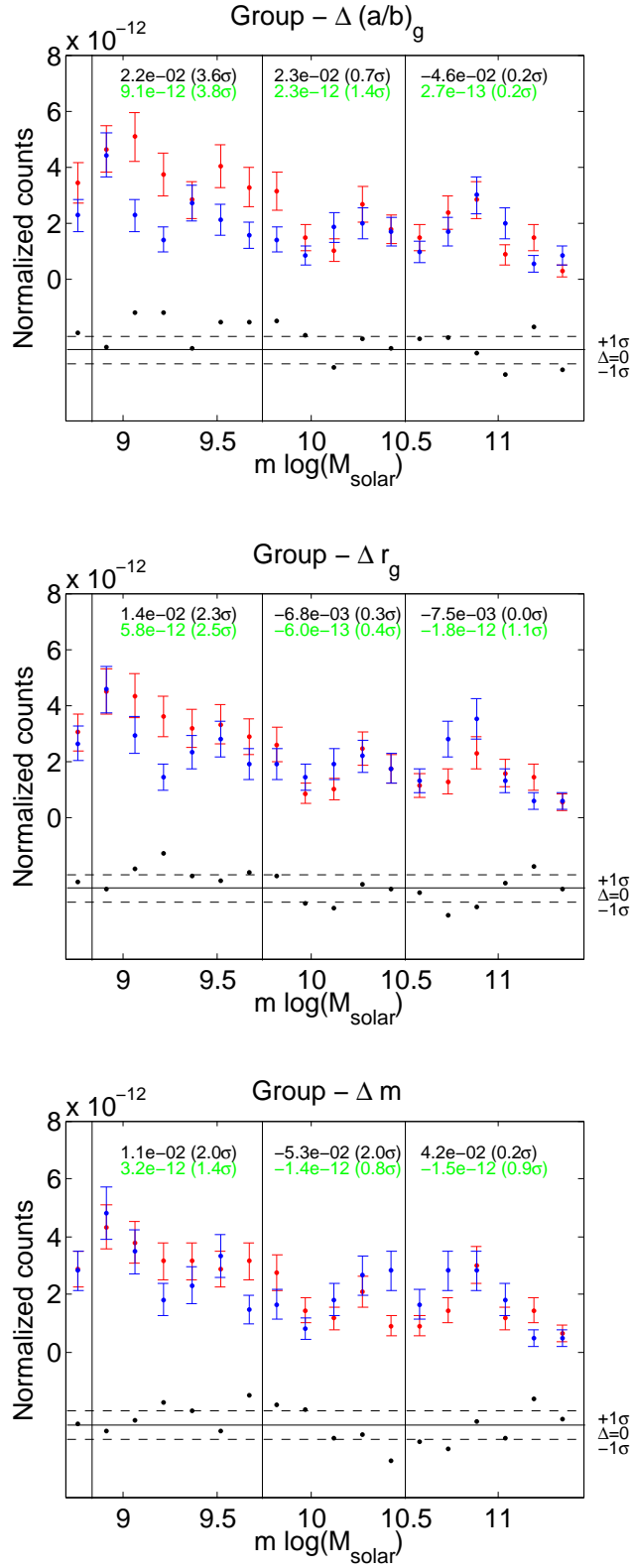
Figure 3.8: Same as Fig. 3.7, but for the group axis ratio, $(a/b)_g$, mean galaxy separation, r_g, and stellar mass difference between the two brightest group members, Δm_g.

(2.3σ). Rounder groups have more mass in dwarfs (3.6σ) and the same is true for groups with larger galaxy separations (2.3σ). Finally, groups with a large difference between the two most massive galaxies have more mass in dwarfs (2.0σ) and a mass function similar to groups with a large total to stellar mass.

As mentioned above we use the same method to study how the average galaxy properties at *fixed stellar mass* in groups depend on the stellar mass function. Figure 3.9, 3.10 and 3.11 illustrate the results obtained.

In terms of average galaxy sizes and shapes we can not identify corresponding significant features in the stellar mass function, except for maybe a slight lack of low mass giants in groups with smaller galaxies. In contrast, for galaxy ages, metallicities, specific star formation rates and morphologies two significant features are visible. Galaxy groups with positive average values of Δt, ΔZ and ΔM_{type} as well as groups with negative average values of $\Delta SSFR$ all have a larger number of dwarfs (2-3σ) and probably a higher mass in this regime (1-3σ). Given the rather continuous increase (or decrease for $\Delta SSFR$) in number difference for decreasing galaxy mass this likely corresponds to a steeper faint end slope of the mass function. A second feature is the number (or mass) of galaxies in the mass range $10^{10.4} - 10^{10.6} M_{\odot}$ minus the number in the range $10^{10.2} - 10^{10.3} M_{\odot}$. Galaxy groups with positive average values of Δt, ΔZ and ΔM_{type} as well as groups with negative average values of $\Delta SSFR$ all have positive differences at 2-3σ. If these four independent properties are combined the significance of the two features increase to more than 5σ.

We also note a probable excess in mass of low mass giants in groups with old galaxies (2.0σ).

3.6 DISCUSSION

We would like to emphasize that the results discussed here concern an essentially volume complete sample of galaxies with stellar masses above $10^{8.7} M_{\odot}$. As mentioned in the introduction, the stellar masses, stellar mass weighted ages, stellar mass weighted metallicities as well as the specific star formation rates presented in this work have been obtained using multi-color imaging data in contrast to many similar studies which are based on spectroscopy (Kauffmann et al., 2004; Gallazzi et al., 2005; Asari et al., 2007). As the information content in spectra are much larger than in broad band colors, spectroscopically determined quantities are expected to be more accurate. However, spectroscopic studies, and in particular studies using fiber spectra like the SDSS, often suffer from aperture bias, i.e., the spectra only samples a limited portion of the galaxies, which in case of non-uniform stellar populations will give a biased view of the galaxies stellar content. Some spectroscopic studies try to take this into account either by making color based aperture corrections like Brinchmann et al. (2004), or by aiming to sample most of the spatial content of the galaxy (Bacon et al., 2001) even though the latter approach leads to smaller sample sizes as this is a seriously challenging task for nearby/large galaxies.

Fig. 3.1 illustrates that the general agreement between our stellar masses and those obtained using the Bell et al. (2003) power law fits for a Kroupa et al. (1993) IMF is fair, but that a systematic difference is seen at larger mass to light ratios, that amount to a difference in m/L_r of 0.15dex. We think that this is caused by the functional form used by Bell et al. (2003) which assumes that the underlying relations between mass to light ratios and colors are power laws, an assumption that appears to work rather well but may not be perfect.

A cautious note: as a Bayesian approach based on the r-band absolute magnitude, M_r, is used to derive t, Z and $SSFR$ the relations between these properties and stellar mass are expected to be influenced by the model[9]. However, the range of parameters which can be reached by the observations for any value of M_r is considerable as we showed in chapter 2

---

[9]As a reminder the Guo et al. (2011) models were used to compute the Bayesian weights.
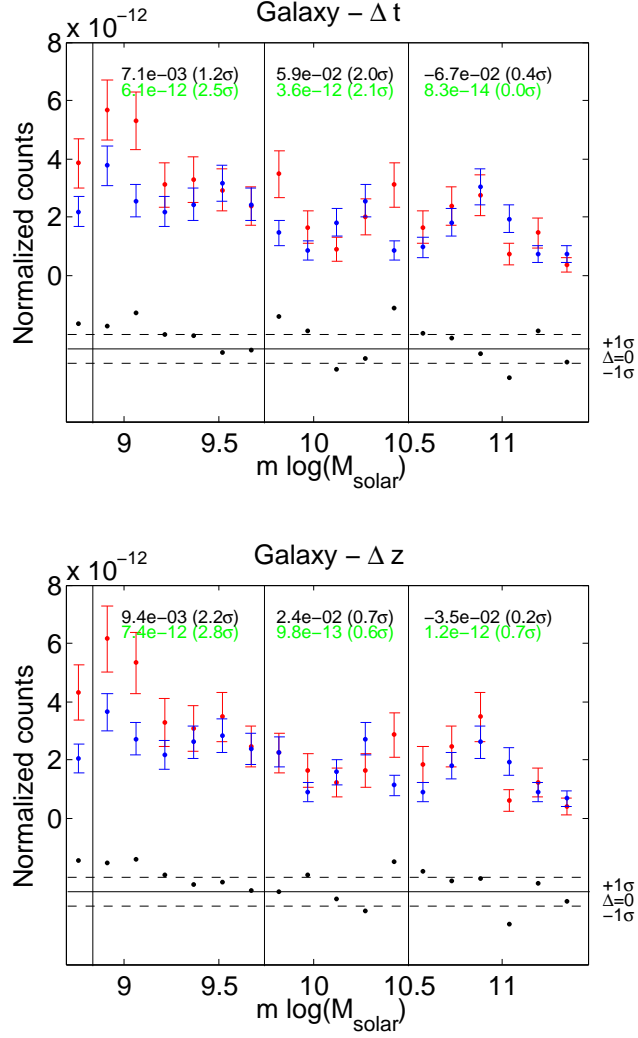
Figure 3.9: Stellar mass functions of groups above (red) and below (blue) the mean relations for groups in terms of galaxy properties as a function of the total stellar mass of the group (see Fig. 3.5), where the mass functions have been normalized by the total stellar mass to allow a fair comparison. The properties considered are the group average offsets in stellar mass weighted age, Δt, and stellar mass weighted metallicity, ΔZ. The difference between the two mass functions in each panel are indicated in units of the standard deviation (black dots). The black vertical lines separates dwarfs, low mass giants and high mass giants for which the differences in numbers (green) and mass (black) between the two mass functions are indicated. The lowest mass bin ($m < 10^{8.9} M_\odot$) have been excluded because it is likely affected by incompleteness.
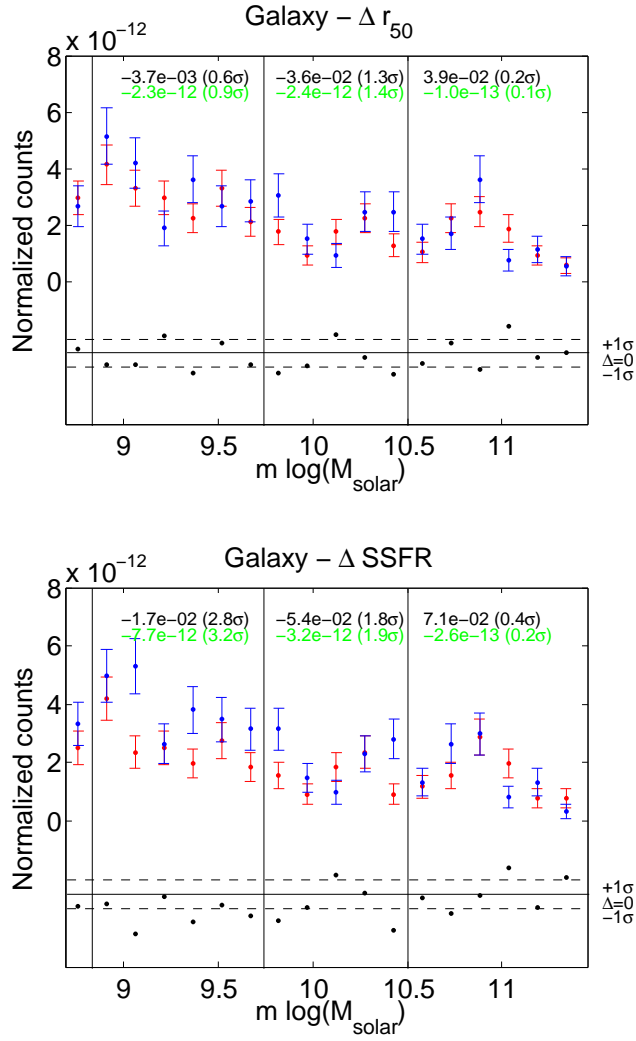
Figure 3.10: Same as Fig. 3.9, but for the half-light radius, Δr_{50}, and the specific star formation rate, $\Delta SSFR$.
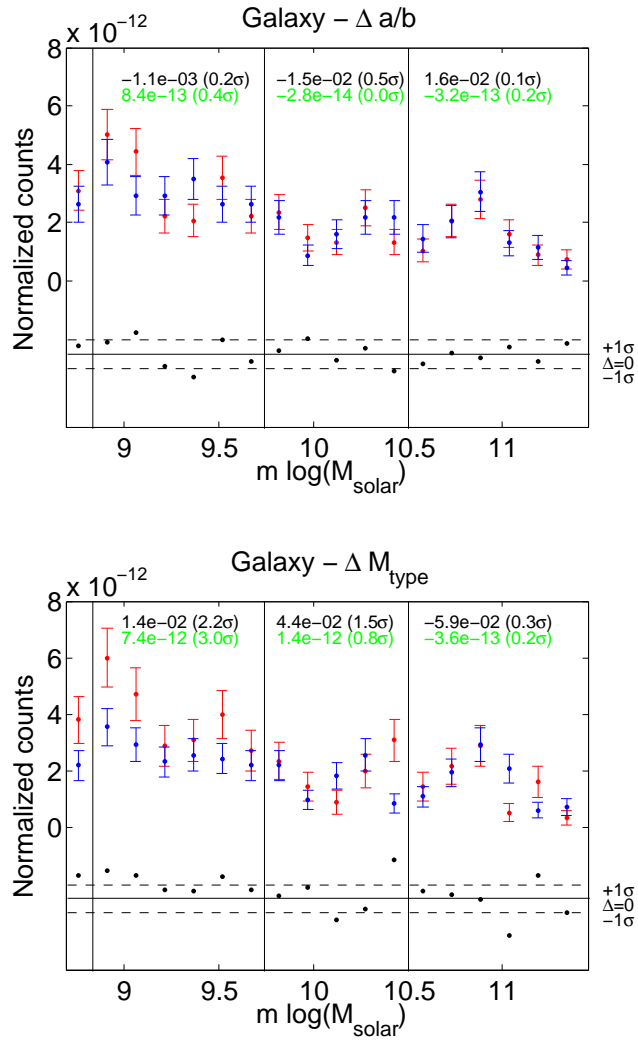
Figure 3.11: Same as Fig. 3.9, but for the axis ratio, $\Delta a/b$ and the morphological type, ΔM_{type}.

(Sec. 2.9.5).

As a reminder for the discussion below, correlations with galaxy properties and stellar mass can be found in Fig. 3.2 and correlations between galaxy properties and group mass can be found in Fig. 3.5.

Stellar ages and star formation rates

Most galaxies have mean stellar ages of around 6-7Gyr, i.e., about half of the age of the Universe. These values are thus consistent with a rather constant star formation rate in the past, or more precisely a star formation rate that only declines slightly with time (remember that a considerable fraction of stellar mass is lost from old populations due to stellar winds and supernovae explosions which will influence the mass weighting). Old galaxies with ages of about 10Gyr are present at all stellar masses, but constitute an increasingly large fraction of the population at higher masses. Very young galaxies ($t <$4Gyr) are rare in our sample and only appear at low masses. Many literature studies focus on luminosity weighted stellar population ages (or age tracers) (Kauffmann et al., 2003b; Gallazzi et al., 2005; Nelan et al., 2005) and consequently find dissimilar relations with stellar mass which are more influenced by recent star formation. The locus of the oldest galaxies shifts from about 10Gyr for low mass galaxies to about 11Gyr for high mass galaxies. Ages are found to correlate with group mass (7.4σ) with galaxies in more massive groups being older. This is in accordance with environmental processes such as ram-pressure stripping (Gunn and Gott, 1972), starvation (Larson et al., 1980), harassment (Moore et al., 1996) and tidal stirring (Mayer et al., 2001) which all tend to put an end to star formation earlier in more dense environments.

We find that passive galaxies are present at all stellar masses. The is also true for isolated galaxies, but remember that our group finder is tuned to improve galaxy distances and the label "isolated" does not rule out any physical connection to other galaxies. The average specific star formation rate drops strongly with increasing stellar mass, a result in agreement with Salim et al. (2007).

Stellar metallicities

Most galaxies fall on a tight and monotonically increasing relation of metallicity versus stellar mass in agreement with previous results (Panter et al., 2008). A rather small number of galaxies populate the region above this relation and seems to cover this space rather uniformly. We suspect that this population could be caused by photometric errors. For a discussion on the mass-metallicity relation we refer the reader to Panter et al. (2008) and Yates et al. (2011).

We find that galaxies in more massive groups are more metal rich (4.7σ). Two mechanisms that can be responsible for such a relation are the following: 1) the presence of a hot intra-group medium can slow down the accretion of pristine gas (Kereš et al., 2005) 2) the deeper potential well of more massive groups makes it easier to retain metal enriched gas expelled by supernovae which in a later stage can fall back onto the galaxies. The second mechanism is in analogy with Larson (1974) but operates on somewhat larger scales. A combination of these effects can explain the group mass-metallicity relation.

Sizes

The relation of half-light radii versus stellar mass is S-shaped with more massive galaxies being larger. A similar trend was observed for early-type galaxies in the Virgo cluster by Janz and Lisker (2008) in their observational data as well as in the semi-analytic galaxy formation models by Nagashima et al. (2005). Kauffmann et al. (2003b) finds a break in the scaling of half-light radii versus stellar mass at $m = 3 \cdot 10^{10} M_\odot$ with a flatter dependence at lower masses, in agreement with our observations. We do not find any relation between r_{50} and group mass and galaxies in groups appear to have the same size as galaxies in isolation. In

59

dense environments tidal stripping can produce more compact objects. Given our finding the effect must be too weak to show up as a significant average group quantity, which seems to be in accordance with Smith et al. (2010a) who find that strong tidal effects on galaxy structure are only present in the very centers of massive clusters and are less frequent than suggested before by (e.g.) Moore et al. (1996). At fixed stellar mass galaxies exhibits a large range of half light radii that amounts to about 1dex. Any model that aims to reproduce the size-mass relation must therefore allow a great variety of sizes at fixed mass in all environments.

Axis ratios
The observed distribution of axis ratios depends only moderately on galaxy mass. The distribution is shaped by the relative frequency of disks and spheroids as well as the intrinsic thickness of stellar disks. Spheroids become more and more frequent at higher luminosities or masses (Graham and Worley, 2008, see also the following paragraph) causing a slight lowering of the mean axis ratio. The distribution of $\log(a/b)$ also decrease slightly for the lowest masses. Thicker disk structures have been observed at lower masses and can be a consequence of supernovae feedback (Governato et al., 2010; Sánchez-Janssen et al., 2010). Moreover, low mass galaxies are more easily influenced by heating in a group tidal field or due to galaxy encounters, an effect which will also tend to make these objects rounder. In dense environments we expect such a heating to be more pronounced than in low density environments. However, the observed relation with group mass is not statistically significant (1.3σ).

Morphological types
The fraction of early-type galaxies is very low at low masses and increases steadily towards higher masses reaching 50% at $m = 10^{11}M_\odot$. A strong trend with an increasing early-type fraction with increasing group mass is observed (11σ), but a significant scatter is present at intermediate masses. It is known that groups with similar total stellar masses can harbor vastly different galaxy populations. For example the Ursa major cluster is dominated by spiral galaxies (Trentham et al., 2001), while groups of similar stellar masses can contain larger numbers of early types (Trentham and Tully, 2009). The group mass-morphology relation is similar to the morphology-density relation (Dressler, 1980), but here we show that the former is present also if the galaxy stellar mass is kept fixed (see also Bamford et al., 2009).

The early-type fraction of isolated galaxies amounts to about 10% of the population in the dwarf regime. Is this really the case? Do early-type dwarfs exist in isolation? As mentioned above even galaxies classified by the group finder as "isolated" can have neighbours with whom they have interacted in the past. Moreover, the visual classification of morphology is not perfect especially for small galaxies located at distances close to the limit of our sample due to the limited resolution. Nevertheless, we found 11 reasonably well resolved early-type dwarfs that do not have any galaxies within 0.7Mpc in projection. However, almost all of these do form stars in their centers as indicated by Balmer emission in their SDSS spectra. Early-type dwarfs in isolation are therefore dissimilar to their counterparts in high density environment, although a subpopulation of early-type dwarfs in the Virgo cluster does have blue centers indicative of recent or ongoing star formation Lisker et al. (2006).

The least massive groups
Galaxies in the least mass groups $(m_g < 5 \cdot 10^{10}M_\odot)$ are on average younger, less metal rich, more star-forming and of later morphological type than isolated galaxies. As these groups only contain a few low mass galaxies, we suspect that ram-pressure stripping is absent or at least inefficient in these environments. The difference with respect to isolated galaxies it that these galaxies have the possibility to interact with each other. Such interactions could remove angular momentum from the gas reservoirs allowing a faster gas accretion and hence

enhance the star formation rate. This scenario is in agreement with the observed values of t, $SSFR$, a/b, M_{type} and is moreover in agreement with the lower metallicities caused by infall of pristine gas. However, continued gas infall is needed to preserve these properties on longer timescale.

Stellar mass functions
Fig. 3.6 highlights an important property of galaxy groups: most of the stellar mass is contained in the most massive members and, if dwarf galaxies are excluded, the median galaxy mass will be a strong function of environment that increases with group mass. This amounts to a difference of 0.5dex in stellar mass between galaxies in isolation and galaxies in groups more massive than $10^{11}M_\odot$.

Galaxy groups
The comparison of stellar masses of our groups in common with Yang et al. (2007), Fig. 3.4, indicates a fair agreement if the higher luminosity limit in the work of Yang et al. (2007) is considered. However, there appears to be some discrepancies in the estimated dark matter halo masses. The use of the Moster et al. (2010) relation for the stellar mass of the most massive group member does not show a good agreement with the ranking of group members performed by Yang et al. (2007). As more galaxies are considered in the later approach, we believe that this is a more robust method for determining dark matter halo masses, but we do not want to speculate about the quality of the quantitative predictions.

Galaxy group properties in terms of the velocity dispersion, the axis ratio, the mean galaxy separation, the dark to stellar mass and the difference in stellar mass between the two most massive group members all correlate with the total stellar mass of the group members as shown in Fig. 3.3, although significant scatter is present.

Stellar mass functions of galaxy groups
One of the most interesting findings in this chapter is that particular features of the galaxy mass function correlate with galaxy properties at *fixed galaxy stellar mass* and at *fixed group stellar mass*. Groups with galaxies that are older, more metal rich, of earlier morphological types and that have lower specific star formation rates have a larger number of dwarfs and a larger mass fraction contained in dwarfs which is most likely connected to a steeper faint end slope of the stellar mass function. Moreover, the same groups also have a larger ratio of galaxies with masses of $\sim 10^{10.5}M_\odot$ with respect to galaxies with masses of $\sim 10^{10.3}M_\odot$.

A steeper luminosity function in denser environment has been observed (Tully et al., 2002; Trentham and Tully, 2009), but our findings suggest that this is true at a fixed group mass for systems that have galaxies which are older, more metal rich, less star forming and of earlier morphological type. This might be connected to an earlier formation and/or a larger total to stellar mass. The stellar mass (or luminosity) function of the field and most groups is quite flat (Bell et al., 2003; Montero-Dorta and Prada, 2009; Trentham and Tully, 2009). Moreover, galaxy mergers and tidal interactions are expected to flatten a steep stellar mass function over time (see chapter 4). So how do these groups acquire a steep stellar mass function? As mentioned in the introduction, galaxies grow due to gas accretion and mergers. If galaxy growth is put to an end early on, before the galaxies have had time to build up a significant stellar mass, then these galaxies could contribute to a steep faint end slope of the luminosity function in the low redshift Universe. Such a scenario would be consistent with the observed faint end slope of the stellar mass function and its connection to "red and dead" galaxies. Processes that could be responsible for an early termination of the star formation could be ram-pressure stripping and possibly reionization as proposed by Tully et al. (2002).

The significant difference in the number of galaxies with stellar masses of $10^{10.5}M_\odot$ and $10^{10.3}M_\odot$ may be associated with the "wiggle" in the luminosity function seen in simulations

and which is "consistent to some degree with observations" (Snaith et al., 2011; Trentham et al., 2006).

The mass functions of groups with high velocity dispersions, larger estimated dark matter halo masses or rounder shapes show both similarities and dissimilarities with the two characteristic features identified. So called fossil groups (D'Onghia et al., 2005) are expected to have formed early and have the characteristic feature of a large luminosity gap between the two most massive group members. We do not see any strong indication that such groups in our sample should have mass functions characteristic of groups with old galaxies even though a higher ratio of dwarfs are observed in such systems.

A potential problem in trying to decipher the connection between galaxy properties, the galaxy mass function and galaxy group properties is that the quality of the latter may be limited due to a possible confusion between group members and foreground and background objects.

3.7 SUMMARY

Stellar population ages and metallicities as well as specific star formation rates, half-light radii, projected axis ratios and morphologies have been obtained using multi color imaging data for an essentially volume complete sample of nearby galaxies (<50Mpc) with stellar masses greater than $10^{8.7}M_\odot$. All these properties are found to correlate strongly with galaxy mass, except for the projected axis ratios which have a weaker dependence. We have constructed a galaxy group catalog using linking lengths tuned to fit data from the Millennium simulation. Importantly, most of the stellar mass in groups are contained in the most massive group members while the mass distribution of isolated galaxies are more extended. By studying galaxy properties at *fixed galaxy mass* we do not see any significant influence of the group environment on galaxy sizes and shapes, but metallicities, ages, specific star formation rates and morphologies do depend on the group mass in accordance with the classical picture of environmental quenching of star formation. In the stellar mass functions of groups we identify several characteristics that depend on specific group properties or average galaxy properties. Most importantly galaxy groups with older, more metal rich, less star forming galaxies with earlier morphological types have more dwarfs and a larger difference in number of galaxies with stellar masses of $\sim 10^{10.3}M_\odot$ with respect to $\sim 10^{10.5}M_\odot$. Both of these features are significant to $> 5\sigma$ at *fixed galaxy group mass*.

3.8 APPENDIX

3.8.1 Photometry

We compare our photometric data with independent measurements by (Lisker et al., 2008; Janz and Lisker, 2009b, Meyer et al. (in prep.)) (LJM) for a subsample of galaxies in common between these studies and our sample. Considering the image pre-processing, different methods are used to combine adjacent SDSS field and the sky subtraction are also not performed in the same way. In this work Kron magnitudes are measured by SourceExtractor within 2.5Kron radii while LJM measure magnitudes within 2 Petrosian radii (Petrosian, 1976), were the latter are determined from coadded g,r,i-images. Moreover, details in star masking and pixel resampling differ and will cause further discrepancies between the data sets, despite that the source of data is the same. Fig. 3.12 shows a comparison of the u,g,r,i,z-band photometry. Two galaxies have been excluded from the plot due to inaccurate photometry caused by overlapping sources. In the figure a comparison with r-band Petrosian magnitudes from the SDSS pipeline is also performed. The figure illustrates that our photometry is of much higher quality than those produced by the SDSS pipeline. For the brightest galaxies in common with LJM we seem to underestimate the objects fluxes. This difference can be
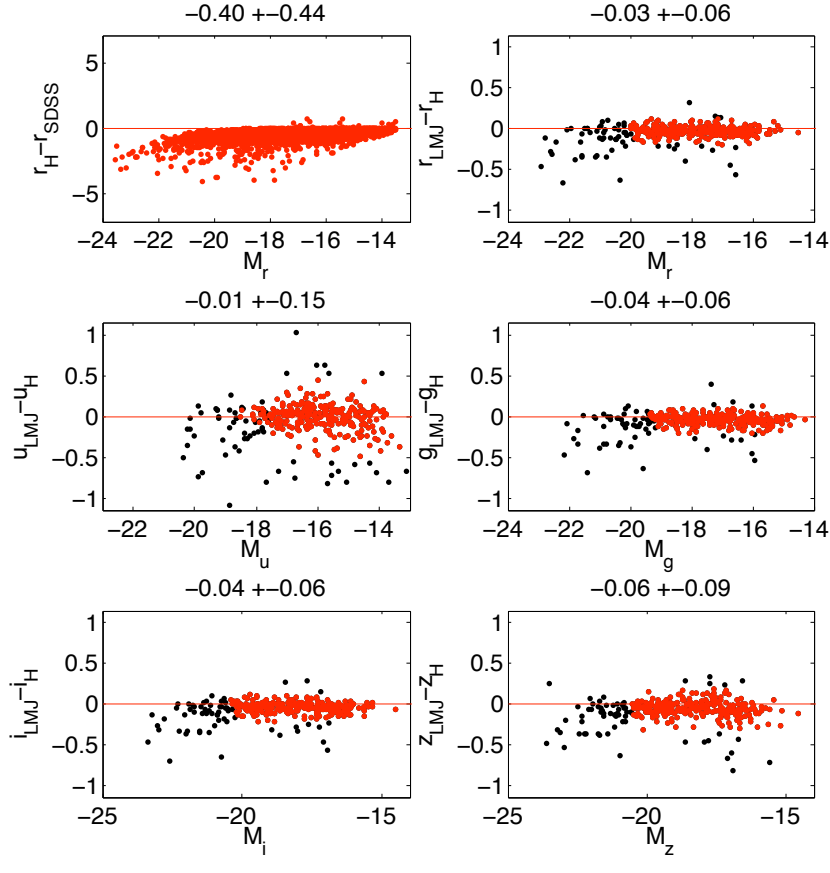
Figure 3.12: Difference in u,g,r,i,z-band photometry measured by Lisker et al. (2008); Janz and Lisker (2009b) and Meyer et al. (in prep.) (LJM) and the data used in this chapter (H) versus absolute r-band magnitude for a a subsample of galaxies in common between the studies. See Section 3.8.1 for more details. The mean offset and σ are indicated on top of each panel.

attributed to the large field sizes needed to sample nearby giants which require the mosaicing of fields, a task which LJM admittably perform better than this study, but a different treatment of light in wings of the light profile can also contribute. As most of the galaxies in our sample are much further away than the Virgo cluster members and are of fainter luminosities we neglect the brightest galaxies when estimating the errors in the photometry through a comparison with LJM.

Chapter 4   The Abell 569 cluster core

An imaging study of the central region of the Abell 569 cluster core at a distance of 85Mpc has been performed. B, R and filter-less images have been obtained with the WIYN0.9m telescope reaching depths of 25.9, 26.9 and 27.6 mag/arcsec^2, respectively. Through the use of model images based on carefully selected fields from a semi analytic galaxy formation model we assess cluster membership based on galaxy magnitudes, colors, sizes and concentration indices. Whether individual galaxies belong to the cluster or not is hard to asses, but for ensembles of galaxies the problem can be tackled using probabilities. The method is used to reconstruct the luminosity function of the cluster core down to $M_R = -14$, as limited by the star/galaxy separation (seeing FWHM~1.9"). A Schecter function is fitted to the data, which yields a faint end slope of -1.25±0.11, while M^* is rather poorly constrained (-22.8±1.3). These values have been debiased from dependences on the model luminosity function. Plausible signs of galaxy interactions in the form of tidal tails, lopsided disks and shell structures are seen in several cases. Given the lack of such features in the two most massive galaxies, most galaxy orbits likely avoid the center or, alternatively, the majority of interaction signatures are not merger signatures.

4.1   INTRODUCTION

The faint end slope of the luminosity function in galaxy clusters has received much attention. Tully et al. (2002) found that the faint end slope steepens with group richness. A number of papers have presented diverse results that range from shallow slopes of ~ -1.2 (Cypriano et al., 2006; Penny and Conselice, 2008; Rines and Geller, 2008) up to even -2.0 (Adami et al., 2007). Discrepancies may be attributed to differences in the way of removing background galaxies (Rines and Geller, 2008), but intrinsic variations are both expected and observed (Weinmann et al., 2011). If stellar population effects are neglected, the luminosity function of a galaxy cluster is shaped by mergers, infall and disruption of low mass galaxies. Tidal tails, lopsided disks and shell structures are commonly interpreted as merger signatures (Malin and Carter, 1983; Rudnick et al., 2000; van Dokkum, 2005; Martínez-Delgado et al., 2010) and can serve as a probe of galaxy mergers (Tal et al., 2009), although tidal forces and close encounter can also produce these kind of features (Moore et al., 1996, 1998). We use deep imaging data to search for signs of galaxy interactions in the core of a galaxy cluster and attempt to interpret the results in connection with the observed luminosity function.

To obtain accurate spectroscopic redshifts from low surface brightness objects such as dwarf galaxies is a seriously challenging task that requires long integrations with large telescopes. Alternative distance indicators are therefore desirable. Imaging data can carry a wealth of information about the distance to a source given that: 1) galaxy structure change with intrinsic brightness (Kauffmann et al., 2003b; Graham and Guzmán, 2003; Janz and Lisker, 2008), 2) galaxy colors change which intrinsic brightness (Baldry et al., 2004; Lisker et al., 2008; Janz and Lisker, 2009b), and 3) colors and surface brightness are redshift dependent (Bolzonella et al., 2000). Discrimination between foreground, group and background

Table 4.1: Summary of observations.

Telescope	Instr.	Target	Filter	Exp. time (s)
WIYN 0.9m	S2KB	A569	B	$4 \cdot 900$
			R	$8 \cdot 900$
			clear	$29 \cdot 900$

galaxies have often been attempted for nearby clusters and groups using 1 and 2 (Binggeli et al., 1985; Trentham and Tully, 2002). Photometric redshifts are on the other hand often used for distance determination on much larger scales (Csabai et al., 2003). With some pre-knowledge of the expected distribution of galaxies along the line of sight the power of such methods increases. One way of obtaining expectation values of galaxy properties in the field of view is to make use of galaxy catalogs from semi analytic models of galaxy formation (Guo et al., 2011; De Lucia et al., 2006; Bower et al., 2006). In this work we make use of the (Guo et al., 2011) model (see also Springel et al., 2005) which has been proved to reproduce a number of important observational constraints such as the galaxy luminosity function and the stellar mass autocorrelation function. It therefore seems reasonable to expect that it can produce, at least to first order, realistic galaxy catalog for any field of view.

In this chapter we explore the power of deep imaging in a study the galaxy population of the central region of the galaxy cluster A569 (Abell, 1958) at a heliocentric redshift of 0.0201 (Struble and Rood, 1999) corresponding to a distance of about 85Mpc[1]. Dale et al. (1997) studied the cluster using I-band imaging and spectroscopy with the aim of probing the Tully and Fisher (1977) relation. However, the cluster core has not been studied using deep imaging. In this chapter we pursue a novel approach to assess cluster memberships of galaxies. We make use of redshift based absolute magnitudes for the three brightest galaxies in the field of view to select suitable fields from Guo et al. (2011). Cluster memberships are then assessed based on observed and modelled galaxy magnitudes, colors, sizes and light concentrations. A motivation of the study, apart from probing galaxy interactions and the luminosity function, is to test the power of the method described above.

The chapter is organized as follows. Section 4.2 describes the observations and the data reduction. In Section 4.3 the construction of the model images is described. Section 4.4 deals with the source extraction and parameter measurements. Section 4.5 describes how cluster memberships are assessed. The luminosity function is derived in Section 4.6. Section 4.7 presents the interaction signatures detected. A toy model for galaxy infall and mergers are presented in Section 4.8. The results are discussed in Section 2.7 and summarized in Section 4.10.

4.2 OBSERVATIONS

The observations were carried out on the 14th and 18th of December 2010 with the WIYN 0.9m telescope located at Kitt Peak in Arizona. The detector used was the S2KB CCD giving a field of view of 20.5' with a pixel scale of 0.6". We used the B and R filters as well as observations with no filter, which we will refer to as the L-band, as summarized in Table 4.1. The quantum efficiency of the CCD limits the sensitivity of the filter-less observation to a region of about 3000-10000Å. The sky conditions were not photometric, including some cirrus on the first night, and the seeing FWHM was around 1.9". Our target, the A569 core, was imaged using offsets between the individual exposures with a step size of order 1'. An exposure time of 900s was used to limit the effects of saturation and cosmic rays.

Master bias and darks were subtracted from the raw science images after which a division with a twilight skyflat was performed. To further improve the image quality of the L-band

---

[1]Throughout this work we use $H_0 =71$km/s.

we constructed a superflat as described below.

4.2.1 Superflat

Each science exposure is divided into 50 by 50 pixel boxes for which the distribution of counts are clipped three times above the median at 1, 5 and 1σ, respectively. Boxes above 1σ of the average are replaced by the mean of their neighbors (2x2) giving a first estimate of the sky background. All connected pixels above the sky at 0.5 and 1σ levels, respectively, were treated as objects if the number of connected pixels were greater than 5 and 100, respectively. The sizes of these objects were further expanded by convolving with a Gaussian (σ=2pix) and making a new size cut at 1% of the flux level. The final background for each exposure was created through a removal of all objects using linear interpolation. A sky background for each night was then created by normalizing the individual backgrounds to the median of all non-masked pixels and by averaging over all frames during the night. Small regions that happened to be masked in all images were filled using linear interpolation. An illumination correction was created by smoothing the superflat with a Gaussian kernel with $\sigma = 5$pix. Moreover, a fringe pattern correction was created by subtracting the superflat from the illumination correction. All science images are divided by the illumination correction, and the fringe pattern is multiplied by the median of each image and is thereafter subtracted.

4.2.2 Image coaddition

Given the small offsets of $\sim$1' between the images shifts and rotations are sufficient for the image coaddition without taking distortions and projection effects into account. As a starting point image shifts and rotations (quantified by the angle Ω) were estimated by visual inspection of the images. Sources were identified using Source Extractor (Bertin and Arnouts, 1996) from which objects with STAR_CLASS > 0.7 were selected as references. The median distances between each pair of sources in the two images were computed for various shifts in x, y and Ω. This exercise was repeated twice around the best solution (i.e. the one having the lowest median distance) using a smaller step in coordinate shift and rotation down to 0.04pixels in x and y, and 30" in Ω. The offsets were applied to shift and rotate the images onto the most central image. The final coadded images we use in this chapter are covered by all exposures in all three filters and have a size of 18.0' by 17.1'. Figure 4.1 shows the coadded L-band image. To reach a slightly better image quality we further coadded the L and R band images using weights as in Knox et al. (1998) to optimize the signal to noise[2]. We refer to these images as LR.

4.2.3 Photometric calibration

As A569 is not covered by the SDSS data release 8 (Aihara et al., 2011) we made use of the USNO-A2.0 catalog (Monet, 1998) for the photometric calibration. The photometric accuracy of this catalog is not very good. Typical errors in USNO-A1.0 (Monet et al., 1998) is 0.25mag and the improvement for USNO-A2.0 is significant mainly for bright sources[3]. Matching our stellar sources (STAR_CLASS > 0.7) with USNO-A2.0 resulted in 361 common sources. The sample was reduced by removing objects with low S/N as well as objects that may suffer from saturation. Finally, a 2σ clipping was applied. The resulting samples have a scatter of 0.19mag in ΔR, 0.17mag in ΔB. The depth of the coadds are 25.9mag/arcsec^2 in B, 26.9mag/arcsec^2 in R and 27.6mag/arcsec^2 in L[4], as estimated through the standard

---

[2]The weights were computed for the median flux of a galaxy in our sample (see Sect. 4.4).

[3]See http://tdc-www.harvard.edu/catalogs/ua1.html and http://tdc-www.harvard.edu/catalogs/ua2.html.

[4]As L magnitudes are unknown this estimate assumes that $m_L=m_R$.
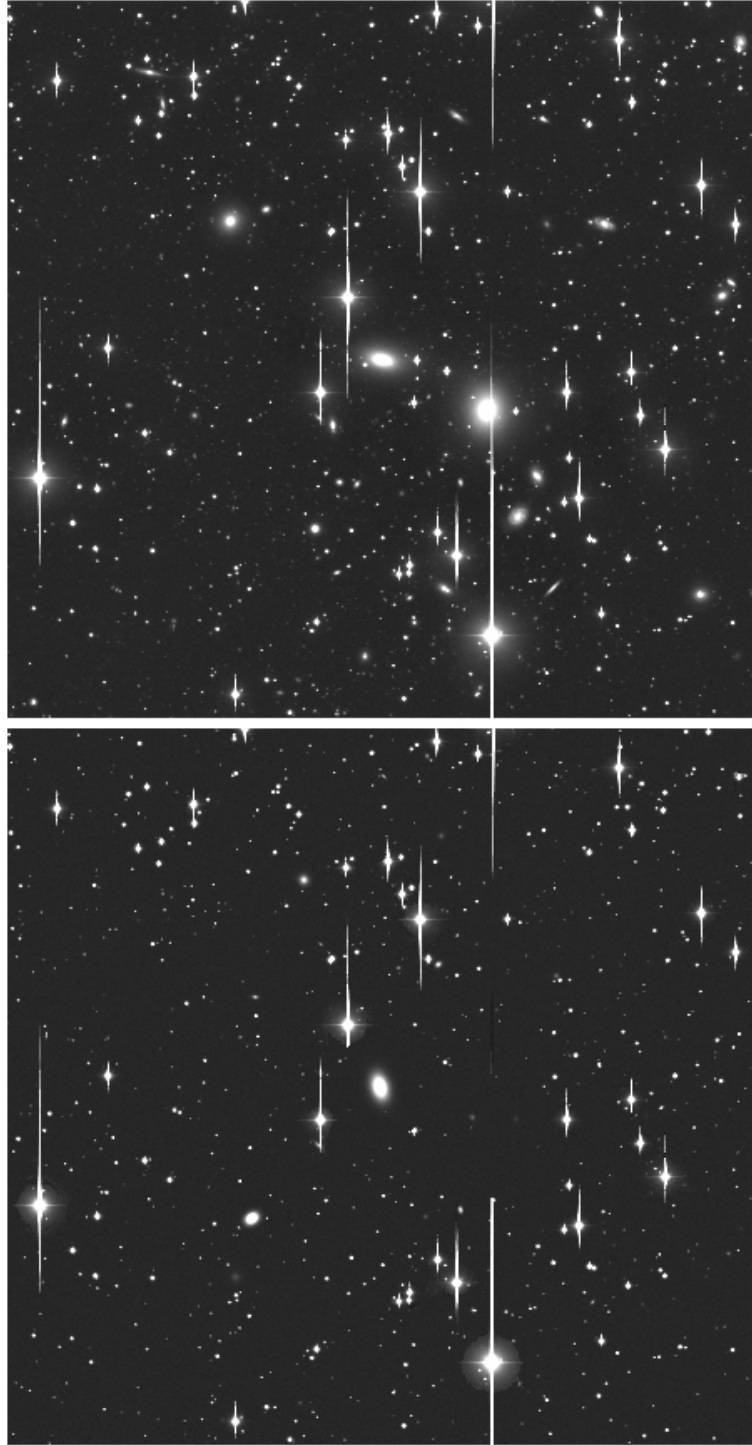
Figure 4.1: **Top panel:** Observed L-band image 18.0' by 17.1' of the A569 core centered on (ra=107.346° dec=48.636°). **Bottom panel:** Modelled image including star from the observed L-band image and galaxies from a similar field of view in the Guo et al. (2011) models have been added.

deviation of the background in regions with no objects[5]. The data is corrected for galactic extinction using the Schlegel et al. (1998) maps.

4.3 MODEL IMAGES

To obtain an object catalog from the models which matches the observation we set out to find objects similar to A569 in the Millennium simulation (Springel et al., 2005). The brightest galaxies in the field of view do have known redshifts in NED[6]. The three brightest galaxies have absolute R-band magnitudes of -22.0, -21.4 and -20.4, respectively, and have (B-R) colors redder than 1.2. We find 18 clusters that have two galaxies, $M_R = -22.0$ and -21.4, with $(B - R) > 1.1$ and no other galaxy brighter than $M_R = -20.4$ within a radius of 0.4Mpc (the size of the field of view at the cluster distance). For each of these clusters we place an "observer" located at a distance of 85Mpc (in the x coordinate of the catalog) from the most massive galaxy. The galaxy populations in the various field of view is taken from Guo et al. (2011). We make use of the cosmology calculator by Wright (2006) to get luminosity distances and angular scales for all objects under the adopted cosmology. As the simulation box is $500h^{-1}$ Mpc, it is insufficiently large to account for all possible background sources. We therefore add background sources up to a distance of 2100Mpc (distance modulus, DM, of 42.2mag) by randomly adding galaxies from the part of the simulation box referred to as milli-Millennium, while keeping the number density of sources constant at the average of the milli-Millennium[7]. This treatment may under predict the field to field variation of distant sources, but not for nearby sources ($< 500h^{-1}$Mpc, DM=39.5) as we apply a periodic boundary condition. Finally, 8 of the 18 model images were discarded because the three brightest galaxies in the field of view as seen by the observers do not reside within the radius defined above.

4.3.1 Model galaxies

The light distribution of the galaxies are modelled by two components. An exponential form for disks is used and a Sersic profile (Sersic, 1968) for bulges. For the latter we use the Sersic index versus luminosity relation from Janz and Lisker (2009a). The absolute magnitude of the bulge, the total absolute magnitude of the galaxy (dust extinction included), the disk scale length and the half mass bulge radii[8] are taken directly from the Guo et al. (2011) catalog. We neglect any extinction of the bulge component and take the difference in the two magnitudes as the brightness of the disk. The disks are given a random inclination and position angle which are translated into axis ratios for infinitely thin disks. If the axis ratios are lower than 1/7 they are adjusted to this value. The minimum value of the axis ratio is motivated by recent studies of disk galaxies (Padilla and Strauss, 2008). The light distribution for each galaxy is computed for a 300x300 pixel image with a scale of 20pixel per scale length (disk+bulge). The image is then rescaled to the pixel scale in kpc/pixel computed for the object in question. After that we use the observed photometric zero points to transform the fluxes into counts and finally we model the effect of the psf through a convolution with a Gaussian. The model magnitudes in the B, R and L-bands are computed based on g, r and

---

[5]We note that the the noise reduction caused by linear interpolation for non-integer image shifts and rotations turns out to be small and we therefore neglect this effect in the noise estimate.

[6]The NASA/IPAC Extragalactic Database (NED) is operated by the Jet Propulsion Laboratory, California Institute of Technology, under contract with the National Aeronautics and Space Administration.

[7]As a test we computed the number of galaxies in Guo et al. (2011) brighter than $M_r = -22.5$ and find that the milli-Millennium has 75% as many sources per unit volume as the total Millennium simulation. However, the number of faint sources in Fig. 4.1 indicates that we do not underestimate the background density in the model.

[8]Half mass bulge radii, r_m, are used to compute scale lengths, h, under the assumption of a constant mass to light ratio and by using $r_m = b^n h$, see Graham and Driver (2005).

i from Guo et al. (2011) and the Blanton and Roweis (2007) color transformations assuming that $M_R=M_L$. Here we also take k-corrections into account using analytic approximations from Chilingarian et al. (2010b)[9].

Our model images are constructed from backgrounds with the same σ as the observations. The original sources identified by SourceExtractor which are brighter than $m_R=21$ and have STAR_CLASS > 0.7 are included to preserve the influence of stars. However, galaxies are left out to avoid an artificially high crowding. All model galaxies inside the field of view seen by our "observers" where added to such background images at their appropriate positions. An example of a model image is shown in Fig. 4.1.

4.4 SOURCE EXTRACTION

We make use of Source Extractor (Bertin and Arnouts, 1996) to detect and measure structural parameters of the observed and modelled galaxies. The L-band image is used for identification of sources since it is the deepest of our images. The detection and deblending parameters were manually tuned to achieve a balance suitable for galaxies significantly larger than the psf. To separate stars and galaxies we make use of the STARCLASS parameter and classify objects with STARCLASS<0.30 as galaxies. Confusion between stars and galaxies become more and more severe at fainter magnitudes. We therefore exclude sources fainter than $m_R=21.0$ (corresponding to $M_R=-13.6$ at the distance of A569) from the analysis (see Fig. 4.2). After manually excluding some detected object corresponding to parts of stars and blended objects our galaxy sample contains 148 galaxies.

4.4.1 Structural parameters

The parameters we use are the ratio of the radii containing 20% and 80% of the object's flux, $C80$ (see Kent, 1985), the radius enclosing half of the object's light, r_{50}, the total R-band magnitude and the $(B-R)$ color. The radii containing 20%, 50% and 80% of the objects flux are measured using the FLUX_RADIUS parameter. ISO magnitudes, which measure the objects' fluxes above the detection threshold, are used throughout.

4.4.2 Completeness

We know the exact position of the inserted galaxies in our model images and a positional match can reveal the corresponding objects from the extracted sources. However, due to uncertainties associated with object detection and deblending we choose to apply m_L as an additional parameter in the object matching. Objects are matched by finding the minimum cartesian distance in pixel rows, columns and m_L using 1mag=10pix. We do not consider galaxies with best matches that have $\sqrt{(\Delta\text{row})^2 + (\Delta\text{column})^2 + (\Delta m_L)^2} > 10$ to have been recovered by the source detection algorithm, corresponding to an incompleteness in our source catalog. Fig. 4.3 shows the completeness of our model images in terms of the percentage of recovered sources as a function of input magnitude. Judging from a visual inspection of the observed images all galaxies brighter than about $m_R=17.0$ must be visible. We therefore set the completeness to 1 at brighter magnitudes.

4.4.3 Quality check

To test the quality of the derived parameters we compare the input values of $C80$, r_{50}, M_R and $(B-R)$ in the model with the values measured in the model images. Comparison plots

---

[9]The formulae give k-corrections based on observed colors and redshifts. For the model galaxies we initially assume that the observed colors are the same as the intrinsic and update the former based on the analytic k-corrections. This was done in five steps for each galaxy, with a constant step size, from z=0.00 up to the model redshift to improve the estimates of the observed magnitudes.
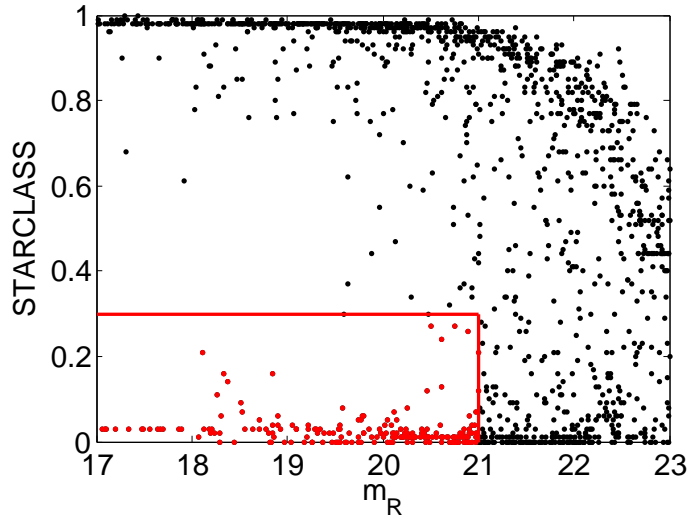
Figure 4.2: STARCLASS from Source Extractor as a function of R-band magnitude for objects detected in the L-band image. The red line shows the selection box used to separate galaxies (red) from stellar sources (black).
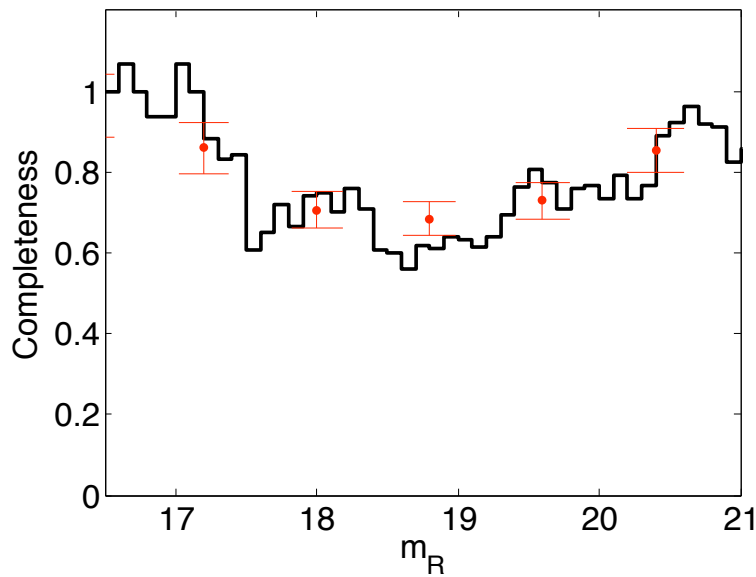
Figure 4.3: Completeness, i.e. the ratio of recovered and inserted galaxies, as a function of m_R computed in bins with widths of 2.0mag. The black line shows a running histogram with a bin size of 2.0mag and a step size of 0.1mag and the red dots show the average in bins used to construct the luminosity function.

along with a short discussion can be found in Appendix 4.11.1. Issues regarding source detection, deblending, matching and parameter measurements give rise to significant discrepancies between the input and measured values. The average standard deviation in 8 equally spaced bins of the quantities are $\sigma_{M_R} = 0.11$mag, $\sigma_{r_{50}} = 11\%$, $\sigma_{C80} = 0.03$ and $\sigma_{(B-R)} = 0.10$.

4.5 MEMBERSHIP

We use the parameters introduced in Sec. 4.4.1 to classify the observed galaxies into two categories: 1) galaxies residing in the cluster and 2) foreground and background objects. In the models we define cluster membership as being within 1.0Mpc of the cluster center at a distance of 85Mpc in the direction parallel to the line of sight.

The structural parameters we have derived are independent quantities that can be used as probes of galaxy distances. Galaxies at higher redshifts have redder $(B-R)$ colors due to the apparent shift in spectral energy distribution caused by the redshift. Many background objects therefore have redder $(B-R)$ colors. In the nearby Universe the apparent galaxy size is inversely proportional to the distance to the galaxy. A galaxy will therefore be larger if it is located in front of the cluster and smaller if is located behind. Galaxy properties in general, including $(B-R)$, r_{50} and $C80$, depend on the intrinsic brightness of the galaxy. The absolute magnitude of the galaxy can thus be estimated using these quantities and be compared with the apparent magnitude to assess the distance to the galaxy. These facts form the basis of the method we use to determine cluster membership and are further complemented with realistic distributions of galaxies along the line of sight to increase the predicting power.

To make use of as much information as possible we evaluate the χ^2 of $C80$, r_{50}, m_R and $(B-R)$ between each observed galaxy and the values measured for galaxies in our model images using σ_{M_r}, $\sigma_{r_{50}}$, σ_{C80} and $\sigma_{(B-R)}$ as defined above. This procedure is repeated 1000 times per object after having perturbed the measurements with Gaussian errors (σ_{M_r}, $\sigma_{r_{50}}$, σ_{C80} and $\sigma_{(B-R)}$). The 1000 model galaxies with the lowest χ^2 for each observed galaxy are used to assess cluster membership. The fraction of the 1000 models that belong to the clusters are taken to be the membership probability, P, for each observed galaxy.

Figure 4.4 shows color magnitude diagrams of galaxies in the model and observation. It can be used to illustrate the procedure. In the model, we can distinguish between member and non-member galaxies, and look at their distribution in the color magnitude diagram (top panel). Obviously, faint red objects are likely to be non-members. Therefore, a color and magnitude value located in this region of the diagram leads to a small membership probability, as illustrated by the symbol color of the bottom panel.

Figure 4.5 and 4.6 show the position of modelled and observed galaxies in diagrams of r_{50} and $C80$ versus m_R, illustrating how these parameters can aid in the discrimination between cluster objects and interlopers. The overlap between cluster members and foreground and background objects in these diagrams are substantial, but, importantly, the density of objects in the two categories varies across the parameter space.

The sum of P for all observed galaxies suggest that the sample contains roughly 36 galaxies belonging to A569. This number is changed to 42 when correction factors for the incompleteness are applied and to 41 once the dependence of the model luminosity function is taken into account as described below.

4.6 LUMINOSITY FUNCTION

Using the membership probabilities we reconstruct the luminosity function of the A569 core in the following way. The number of objects in our observed galaxy sample in bins of M_R from -22.4 to -14.4 using a bin width of 0.8mag are computed using P as weights. For $4 \cdot 10^6$ luminosity functions on the Schechter (1976) form with α -1.0005,-1.0010,...,-2.000 and
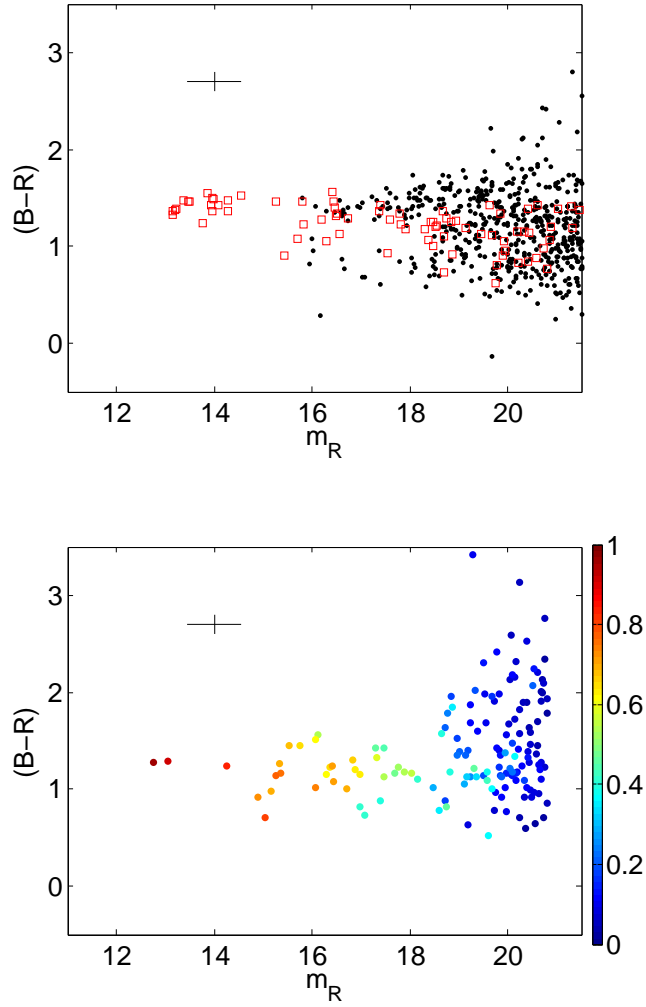
Figure 4.4: **Top panel:** (B-R) color versus R-band magnitude for cluster members (red) and foreground and background objects (black) in the model images. **Bottom panel:** (B-R) color versus R-band magnitude for observed galaxies color coded by their membership probability P. The errorbars indicated $\sigma_{(B-R)}$ and $5\sigma_{m_R}$

.
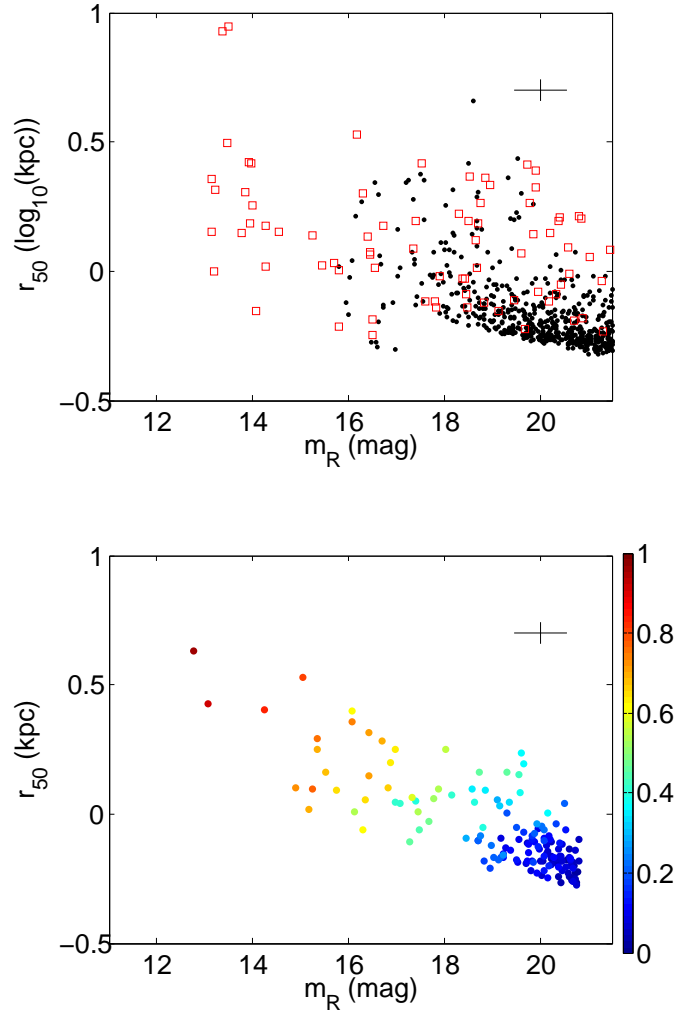
Figure 4.5: **Top panel:** Half-light radius, r_{50}, versus R-band magnitude for cluster members (red) and foreground and background objects (black) in the model images. **Bottom panel:** Half-light radius, r_{50}, versus R-band magnitude for observed galaxies color coded by their membership probability P. The errorbars indicated $\sigma_{r_{50}}$ and $5\sigma_{m_R}$
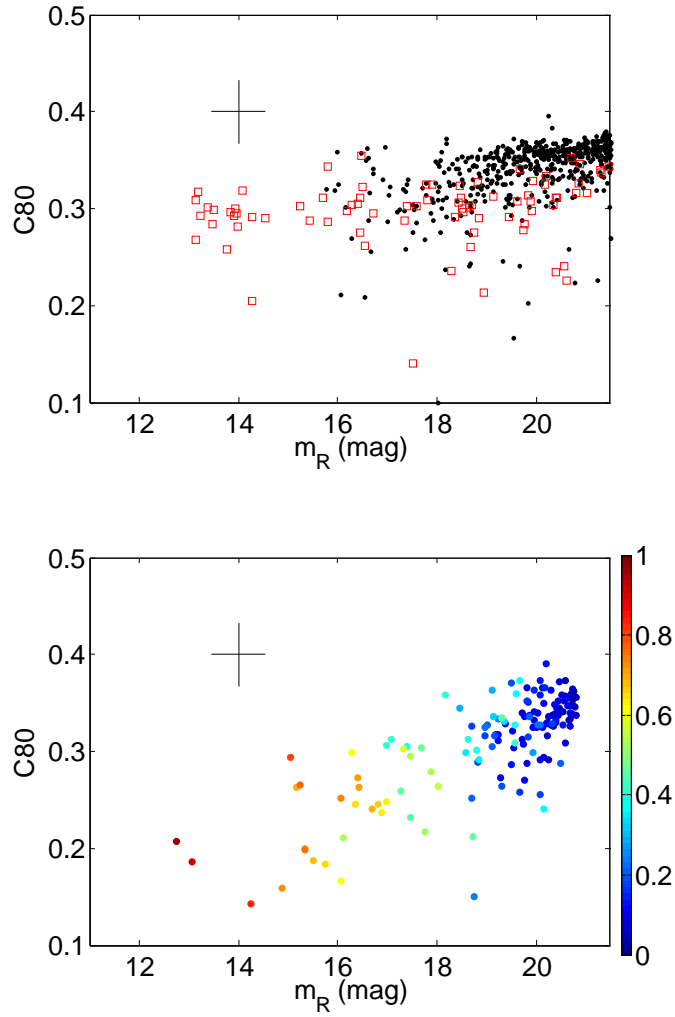
Figure 4.6: **Top panel:** Concentration index, $C80$, versus R-band magnitude for cluster members (red) and foreground and background objects (black) in the model images. **Bottom panel:** Concentration index, $C80$, color versus R-band magnitude for observed galaxies color coded by their membership probability P. The errorbars indicated σ_{C80} and $5\sigma_{m_R}$

M_R^*=-18.000,-18.003,...,-26.000 42 galaxies are randomly drawn for each set of parameters. If the corresponding luminosity functions are exactly the same as the one reconstructed from the observations at M_R=-20.0 and above, and within the Poisson noise (reduced χ^2 <=1.00) for the fainter bins that particular luminosity function is considered a match. The best fit luminosity function in terms of α and M_R^* is taken as the average of the matches.

The outcome of this "fit" does not depend on any intitial guess and is more sensitive to the bright end than if matching luminosity functions would be chosen using Poisson errors at M_R <=-20 as well.

The best fit luminosity function is found to be $\alpha = 1.26 \pm 0.11$ and M_R^*=-22.7 $\pm$ 1.3.

4.6.1 Debias for model dependence

As P is computed as the ratio of cluster members and foreground and background galaxies in the model, the outcome will depend on the luminosity function of the model. To account for this we include a weight, w, in the computation of P that compensates for the difference in observed slope, α_{obs}, and the slope, α_{mod}, measured in the Guo et al. (2011) model data for the corresponding clusters. As the faint end slope of the model data drops at M_R >-17 (Fig. 4.7) due to the mass resolution limit of the simulation, we apply an additional correction factor for faint galaxies. This factor is determined as the difference in the average faint end slope above and below M_R=-17. α is measured using the technique outlined above for M_R <-17 and by fitting a power law to the data at M_R >=-17. The weights are given by

$$w \underset{M_R <= -17}{=} 10^{-0.4(\alpha_{obs} - \alpha mod)(M_R - M_R^*)} \tag{4.1}$$
$$w \underset{M_R > -17}{=} 10^{-0.4((\alpha_{obs} - \alpha mod)(M_R - M_R^*) - 0.30(M_R + 17.0))}$$

where the factor $-0.30(M_R + 17.0)$ compensates for the mass resolution limit. As α_{obs} and M_R^* change after introducing w, the procedure must be iterated. After only one iteration the parameters stabilize at α=1.25 and M_R^*=-22.8, which we consider the final parameters of the observed luminosity function. Figure 4.7 shows the derived luminosity function and Fig. 4.8 shows the final debiased membership probabilities, P_{de}, as a function of M_R. In case individual model images are used to derive memberships we obtain several independent measurements of P_{de} which are found to have a standard deviation of 0.09, which increases to 0.16 if only galaxies with P_{de} >0.20 are considered.

4.7 GALAXY INTERACTIONS

Through a visual inspection we search for features indicative of galaxy-interactions. Figure 4.9 shows LR-band images of six galaxies that exhibits interesting features. In one elliptical galaxy we identify a shell-like structure with a sharp edge. This galaxy has overall somewhat irregular and asymmetric isophotes which are probably not caused by the psf. Another galaxy exhibits dumbbell-shaped outer isophotes from a shell structure or maybe a spiral arm. One spiral galaxy have a strongly lopsided outer disk, while a second lopsided spiral appear to have a tidal tail extending from the plane of the disk. A second case of a galaxy with a tidal tail is also observed. This galaxy has a very close neighbor, but based on the visual inspection we are not sure whether the neighbor is related or not. Additionally, two overlapping sources are observed that could be a pair of elliptical galaxies undergoing a merger. A light excess is observed close to the pair which may be caused by material expelled during the merger.

As described above we have identified several galaxies with plausible interaction signatures. This includes tidal tails, shell structures, lopsided disks and possibly a galaxy pair undergoing a merger. We would like to emphasize that some of the features might not be unambiguous detections. To make sure that the features we detect are not caused by the
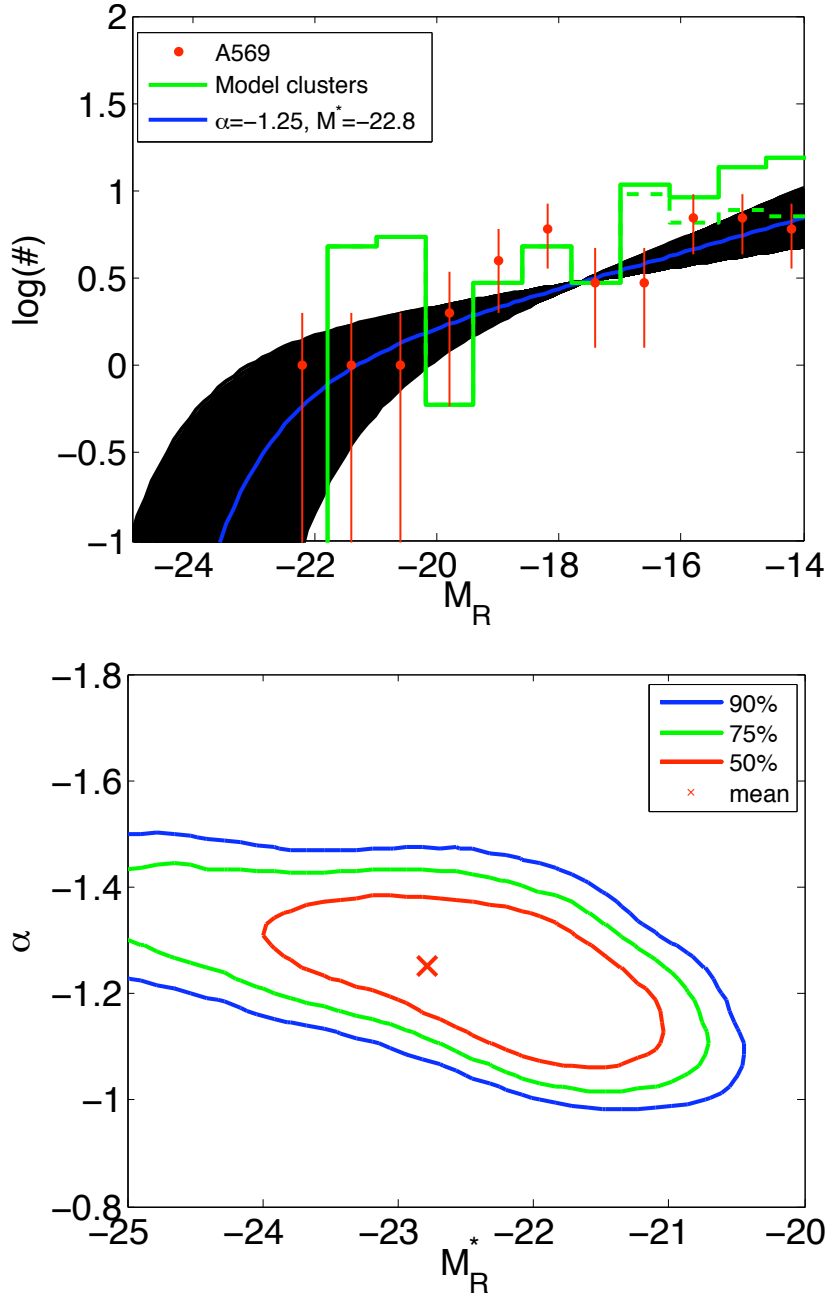
Figure 4.7: **Top panel:** Number of galaxies that belong to the A569 cluster core in bins of absolute R-band magnitude (red dots), with $\sqrt{N}$ error bars. The best fit Schechter (1976) function (blue line) with 1σ errors (black region) are shown along with the luminosity function of model cluster members (green histogram where the original faint end (dashed line) have been corrected for the mass resolution limit) where the luminosity functions have been normalized to the observed value for $M_R=-17.4$. The bright end of the model luminosity function differ slightly from the selection criteria (Sec. 4.3) because the magnitudes are somewhat altered by dust. **Bottom panel:** Distribution of luminosity functions that match the observations in α versus M_R^*. The red cross shows the average values of $\alpha=1.25$ and $M_R^*=-22.80$ and the contours show the 90% (blue), 75% (green) and 50% (blue) confidence intervals.
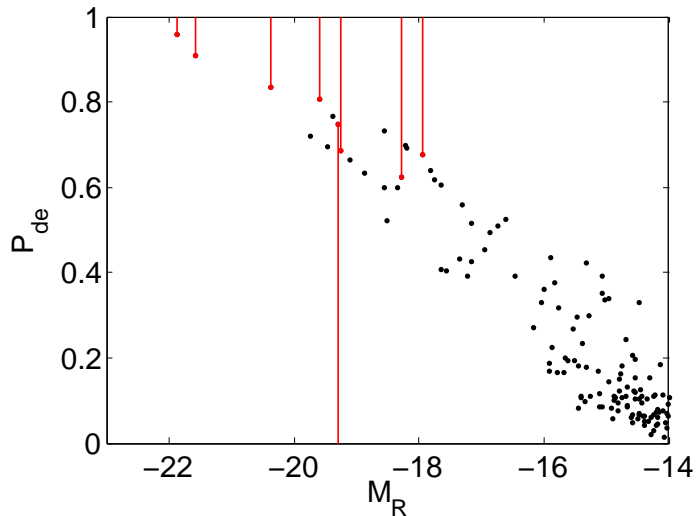
Figure 4.8: Debiased cluster membership probabilities, P_{de}, versus absolute R-band magnitude, m_R, for the galaxy sample studied in this chapter (dots). Galaxies with available redshifts are denoted in red with lines indicating whether their radial velocities, v, are consistent with them being cluster members ($5700 < v < 6400$, $P_{de}=1$) or not ($P_{de}=0$).

superflat due to insufficient masking of objects we also inspect images reduced without the superflat and find a good consistency. The features we report here are thus not caused by the superflat. We therefore believe that the majority of the signatures we report are indeed caused by galaxy interactions.

4.8 TOY MODEL

The observations have revealed signs of galaxy interactions as well as the luminosity function of the A569 cluster core. In this section we interpret both these results within the framework of a very simple model. In the core of a cluster the stellar populations of most galaxies are old and their luminosities therefore mainly trace stellar mass. If the system were closed, the evolution of the luminosity function would solely be determined by the redistribution of stellar material through galaxy mergers, tidal stripping and mass loss due to close encounters. As stars in low mass galaxies are less bound, they are more susceptible to external influence and processes such as tidal stripping due to close encounters between galaxies are therefore more efficient in the low mass regime. These processes are therefore expected to lower α over time. The influence of galaxy mergers are less straight forward as the merger frequency depends on galaxy masses, velocities and orbits. Limited kinematic data are at hand which makes assumptions necessary. In the simulated observations most clusters have a rather mass independent velocity dispersion at $M_R > -19$ that drops towards zero for even more luminous galaxies. Five cluster members with $M_R > -19$ have redshifts and for these we estimate a 3D velocity dispersion of roughly 700km/s. For our model we adopt this constant velocity dispersion for $M_R > -19$. At higher luminosities we let the dispersion drop with a constant slope and reach zero a $M_R = -24$.

Due to the moderate depth of the B-band images we decided to use a constant mass to light ratio for all galaxies. From the median of $(B-R)=1.3$ for cluster members we chose the

78
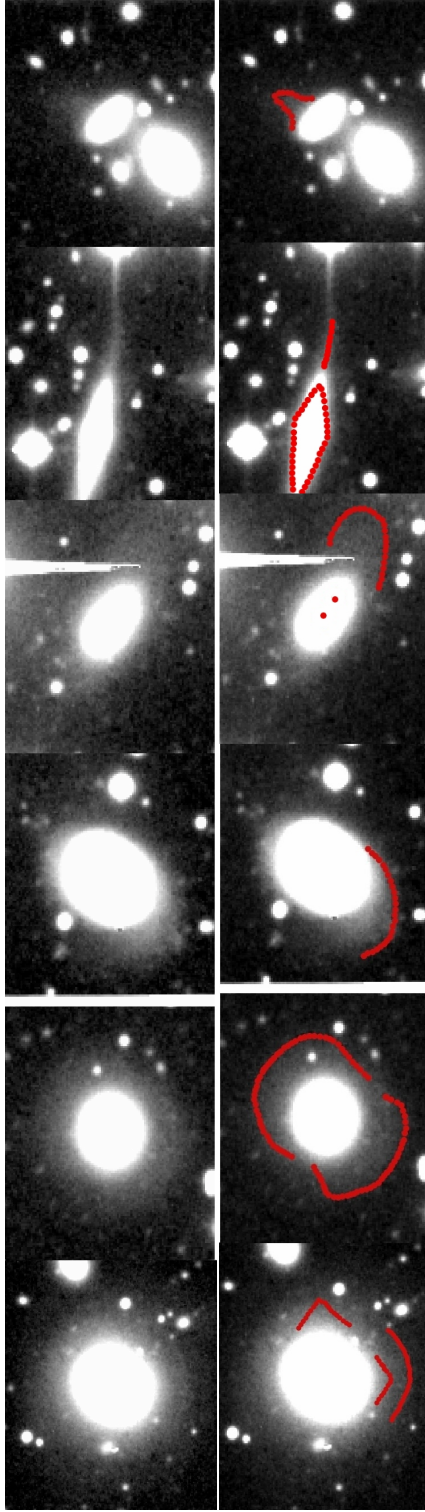
Figure 4.9: **Top panels:** *LR*-band images showing galaxies with features plausibly indicative of galaxy-galaxy interactions. The left most image is 1.8'x1.5' and all the rest are 1.3'x1.1'. The images are drawn with the same contrast level. **Bottom panels:** Same as the top panels but where the features are highlighted with red color to guide the eye. **Comments on individual galaxies:** From left to right: 1) This elliptical galaxy has a shell like structure with a sharp edge in the lower part of the image as well as overall somewhat irregular and asymmetric isophotes which are probably not caused by the psf. 2) Dumbbell shaped outer isophotes from a shell structure or maybe a spiral arm. A star overlap the central part of the galaxy. 3) Strongly lopsided outer disk. 4) Two overlapping sources and possibly an associated light excess. Could be a system undergoing a merger or simply a pair in projected. 5) Lopsided disk galaxy with a tidal tail. Judging from other bright stars in the region the diffraction spike to the right should not reach the galaxy/tidal tail. 6) Galaxy with a tidal tail. We are uncertain whether the bright neighbouring galaxy is related or not.

79

mean value of M/L_R=2.1 based on the models in Hansson et al. (in prep.)[10].

A closed box model certainly has its disadvantage and we therefore complement with galaxy infall from a global average luminosity function of Montero-Dorta and Prada (2009) with α =1.16 and M^* =-21.0[11]. The infall rate is adjusted to the merger rate to keep the total number of galaxies with M_R >-14.0 constant.

We base the merger model on the cross section, s, for collisions including gravitational focusing

$$s = \pi r^2 \left(1 + \frac{GM}{v^2 r}\right) \tag{4.2}$$

where r is the radius of the colliding bodies, which we take to be the half-light radius, r_{50}, M is the mass, G is the gravitational constant and v is the initial difference in velocity. If we consider each possible merger separately the merger probability per unit time, ψ, is proportional to vs. If the radius is expressed in terms of the stellar mass of the most massive galaxy in the merger, m_1, ($r = 3(m_1/5e10)^{0.3}$kpc, Kauffmann et al. (2003b)[12]), we have the following proportionality

$$\psi \propto M^{0.6} \left(1 + \frac{GM}{v^2 3(m_1/(5 \cdot 10^{10}))^{0.3}\text{kpc}}\right) \tag{4.3}$$

By computing ψ for all possible galaxy mergers the model can be evolved one merger at a time by randomly drawing a merger from the probabilities given by ψ. We investigate the evolution of the model both when M is taken as the stellar mass, m, and as the total halo mass estimated by a halo to stellar mass ranking (Moster et al., 2010). When galaxies enter a more massive halo their dark matter is gradually stripped. We thus expect that in reality the solution lies in between these two extremes.

To account for galaxies below the detection limit we extrapolate the luminosity function by 2.4mag to allow for less massive merger progenitors. The evolutionary tracks, in terms of α and M^* are shown in Fig. 4.10 along with luminosity functions of some nearby groups and clusters from the literature.

If we interpret the observed interaction signatures as merger signatures, this merger model can be extended to predict their frequency as a function of galaxy mass. Whether a merger signature will be present depends on: 1) whether any merger has occurred and thus in an average sense on ψ 2) the prominence of the merger signature, or in other words, the ability to detect that particular feature, D 3) the lifetime of the merger signature, τ.

In the following we denote the least massive galaxy in a merging pair as the secondary and the most massive as the primary. In general the signature can be seen as a disruption of the secondary and/or a perturbation of the primary caused by the secondary. We therefore find it reasonable to assume that D is proportional to the signal to noise per unit area of the faintest galaxy in the interaction, a property which under the assumption of a constant mass to light ratio is proportional to the stellar surface mass density of the secondary. Using the relation between stellar mass and stellar surface mass density from Kauffmann et al. (2003a) for galaxies below the bimodality mass we have that

$$D \propto m_2^{0.63} \tag{4.4}$$

where m_2 is the mass of the least massive of the two galaxies. Finally, we need some prescription for the lifetime of merger signatures. As this property depends on the dynamics of the

---

[10]These are based on the Bruzual and Charlot (2003) single stellar population models, a Chabrier (2003) IMF, line emission from Kotulla et al. (2009) and new dust prescriptions for a large range of star formation histories and chemical enrichments (see chapter 2).

[11]These values are based on $^{0.1}i$ which have an effective wavelength that are only 5% longer than for R at z=0.0.

[12]This relation is based on the median stellar mass and half-light radii from Kauffmann et al. (2003a) and use the scaling valid above the bimodality mass ($5 \cdot 10^{10}\text{M}_\odot$) from Kauffmann et al. (2003b).
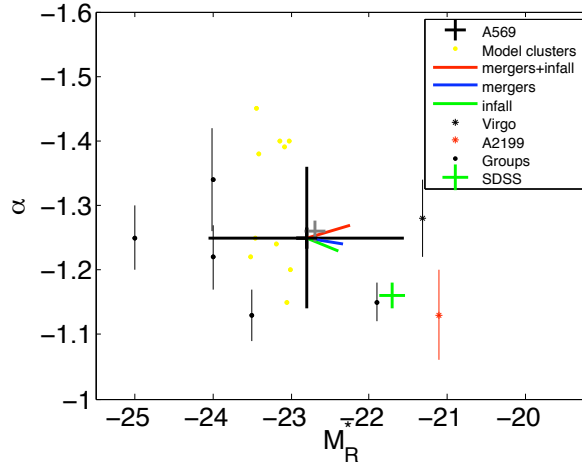
Figure 4.10: Luminosity function faint end slope, α, and turnover magnitude, M^* for the A569 core (black cross) evolved with our merger+infall model (red), our merger model (blue) and by infall only (green) as well as for the Virgo cluster Rines and Geller (2008) (black star), the A2199 cluster (Rines and Geller, 2008) (red star), and the compilation of groups from Trentham and Tully (2009) (black dots). For the Virgo and Abell 2199 data points we have assumed that $M_R = M_r$ (the effective wavelengths of the filters differ by only 5%). The results shown in red, blue and green are the average of the results for models with and without dark matter.

galaxies, the orbits and viewing angle, properties which are likely unknown, we assume τ is proportional to the dynamical timescale (see Tal et al., 2009) as estimated from the circular velocity

$$\tau \propto r/(GM/r)^{-1/2} \propto m_{1+2}^{-0.05} \tag{4.5}$$

Where the r is taken to be the half-light radius, m_{1+2} is the total stellar mass of the two galaxies and the second proportionally comes from the assumption that stellar mass dominates over dark matter within this radius.

To summarize the presence of detectable merger signatures, η, ought to be proportional to

$$\eta = Nv\psi m_{1+2}^{-0.05} m_2^{0.63} \tag{4.6}$$

where we choose the normalization constant, N, to reproduce the total number of detected galaxy interactions. Equation 4.6 is evaluated before the first merger in our model and predicts the frequency of merger signatures as a function of galaxy mass. Fig. 4.11 show a comparison between the observed and modelled distribution of detected interaction signatures as a function of m_R. The sum of P_{de} for the galaxies with plausible interaction signatures amounts to 4.2, but if the values are rounded off in bins of m_R as in Fig. 4.11 the sum is instead 5. We therefore select 5 galaxies randomly from the distribution of modelled interaction signatures 50000 times for the models without dark matter. These distributions are compared with each other and in 95% of the cases the distributions are reproduced more often than the (rounded) observed distribution. The observed distribution thus disagrees with the models at a 2σ level. If the procedure is repeated for the model with dark matter the corresponding figure is at least 3σ, because the observations are in no case closer than the random realizations.
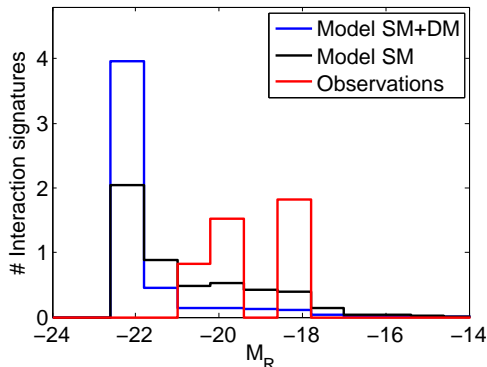
Figure 4.11: Distribution of observed (red) and modelled interaction signatures as a function of galaxy absolute R-band magnitude. The observed distribution has been weighted by the membership probabilities, P_{de}. Results are shown for models where masses are computed as the stellar mass (black) as well as the total mass (blue) estimated from a stellar to dark matter halo mass ranking (Moster et al., 2010).

4.9   DISCUSSION

4.9.1   Method used for deriving cluster membership

Figure 4.8 shows that the method we use to determine cluster membership certainly suffers from some uncertainty as the distribution of P_{de} extends rather smoothly from 0 to 1. We find the method sufficiently good for a statistical extraction of the galaxy luminosity function, but for individual galaxies at fainter magnitudes ($M_R >$-19) it is in many cases not good enough to assess membership (see Fig. 4.8). The field to field variation in P_{de} suggest an average uncertainty of about 0.09. However, this estimate has two limitations namely that it does not take field to field density variation at distances of more than $500h^{-1}$Mpc into account (see Sec. 4.3.1) and that the statistics of individual fields are limited. Redshifts are available for eight galaxies in the field of view. Seven of these have redshifts consistent with them being cluster members, while $\sum P_{de}$=6.2. Figure 4.8 shows that P_{de} depends strongly on m_R reflecting that most of the model galaxies that do not belong to the cluster are background galaxies and that these become more and more abundant at fainter magnitudes.

The discrimination power of the method lies in the relative values of m_R, r_{50}, $C80$ and (B-R) for objects at various distances. Apparent sizes of galaxies at low redshift are proportional to the distances at which the objects are located. Relative differences in size corresponding to a fixed physical separation along the line of sight thus become smaller with increasing distance. The galaxy number density contrast of the cluster plays a major role in enhancing P_{de} and thus lower the confusion between background and foreground objects. The power of the method therefore depends strongly on: 1) cluster distance 2) galaxy number density of the cluster 3) cosmic variance, or in other words, the amount of foreground and background contamination. We therefore recommend to consider the limitations carefully before adopting this method. Note, that it is possible to apply the method not only to clusters but to any field of view, although the limitations will be greater if the objects of interest do not reside in an over density.

4.9.2 Luminosity function

A direct comparison between studies of the galaxy luminosity function is hard to perform for the following reasons. The result depends on the method adopted to measure distances or differentiate between cluster (or group) members and foreground and background galaxies (Lieder et al. (in press)). The choice of band will yield somewhat different results (Montero-Dorta and Prada, 2009) due to the shape of the spectral energy distributions. Moreover, the method used to measure α and M^* differs (see e.g. Barkhouse et al., 2007; Rines and Geller, 2008) and the absolute magnitude limit can influence the results.

As our value for M_R^* is poorly constrained we instead focus the discussion on α. Our value of α=-1.25±0.11 is similar to those found for the Sloan Digital Sky Survey Sixth Data Release (Adelman-McCarthy et al., 2008; Montero-Dorta and Prada, 2009), nearby galaxy groups by Trentham and Tully (2009) as well as the Virgo and A2199 clusters as studied by Rines and Geller (2008), see Fig. 4.10. Studies of nearby galaxy clusters using other filter bands also reveal faint end slopes similar to ours (Mieske et al., 2007; Penny and Conselice, 2008; Misgeld et al., 2008, 2009), although Lieder et al. (in press) finds a V-band slope of α=-1.49±0.17 for the Virgo cluster core. Our toy model suggests that the faint end slope will not change significantly due to mergers and infall of field galaxies. We tested whether this also holds for an initially steeper slope of α=-1.5 and find that such a slope will flatten with time. The latter is in agreement with the simulations of Fang and Saslaw (1997). Penny et al. (2009) argue that some dwarf galaxies in the core of the Perseus cluster must have substantial dark matter content to avoid disruption by the tidal field of the cluster. Tidal disruption is not included in our model and this effect could contribute to a flattening of the faint end slope with time (see also Moore et al., 1996, 1998).

4.9.3 Interaction signatures

Our model for galaxy mergers and infall of field galaxies is indeed very simple. An assumption that enters is that galaxy orbits are random. This can in our case not be tested by observations, and such attempts would nevertheless suffer from the lack of proper motions at distances much beyond the local group. Lisker et al. (2009) conclude that a certain subpopulation of galaxies in the Virgo cluster are probably on circularized orbits suggesting that they have been residing in the cluster for a long time. As the most massive cluster galaxies likely reside in or close to the cluster center they would not collide with galaxies on circularized orbits providing a possible explanation for the lack of merger signatures in the two most massive galaxies.

Mergers are not solely behind tidal tails, shells and lopsided disks. Hα observations have revealed ram-pressure stripping of ionized gas from galaxies in clusters (Sun et al., 2007). In principle this could cause an optical signature similar to what is observed (Smith et al., 2010b). However, one of the galaxies for which we detect tidal tails is also lopsided which could disfavors such an interpretation. Close encounters and tidal interaction could also be responsible for the observed interaction signatures (Moore et al., 1996; Mastropietro et al., 2005). However, a close encounter is just about a merger. We therefore expect they should behave similar to mergers, although the signature is likely more pronounced in the less massive of the two galaxies. This would be a possible explanation for the lack of interaction signatures in the two brightest cluster members, but note that the results of Smith et al. (2010a) indicate that close encounters might be less important than previously thought. A question that arises regarding the interpretation of merger signatures is the following. *How frequent are mergers in clusters?* There is some debate in the literature about this. Makino and Hut (1997) find that mergers are rare in clusters today due to the high velocity dispersion of these system, but the merger rate must have been greater in the past van Dokkum et al. (1999). For the Millennium simulation Fakhouri and Ma (2009) found an increasing merger rate of dark matter haloes with increasing galaxy number density, but this result may not hold

for subhaloes and is perhaps not realistic for galaxy clusters. Lin et al. (2010) investigated the merger rate by looking at the frequency of galaxy pairs as a function of environment and used numerical simulations to assess whether the galaxy pairs will merge or not. They find that gas rich mergers have a weak environmental dependence, but that gas poor merger increase rapidly with local density. Ellison et al. (2010) conclude that mergers leading to tidal distortions occur in all environment and that the close pair fraction of asymmetric galaxies is the highest in cluster centers. The simulations by Feldmann et al. (2008) show that the lifetime of merger signatures depends on the dynamics of the galaxies. Features caused by dynamically hot systems disperse faster, which can explain that Tal et al. (2009) finds a lower frequency of tidal features in elliptical galaxies that reside in clusters. The picture emerging from the discussion above seems to favor a relatively high merger rate in clusters centers. It is on the other hand not clear how the merger rate compares with close encounters that cause tidal features.

4.10   SUMMARY

Deep R, B and filterless observations of the A569 cluster core located at a distance of 85Mpc have been obtained with the WIYN 0.9m telescope. Cluster membership probabilities, P_{de}, of objects in the field are estimated by comparing m_R, r_{50}, $C80$ and (B-R) with model images based on the Guo et al. (2011) galaxy catalog from a semi analytic galaxy formation model. With the use of P_{de} we have investigated the galaxy luminosity function of the cluster core. Aided by the deep images we detect plausible signs of galaxy interaction in six cluster members in the form of shells, tidal tails, lopsided disks and a galaxy pair possibly undergoing a merger. The evolution of the luminosity function and the frequency of interaction signatures as a function of galaxy luminosity is investigated using a toy model of galaxy infall and mergers. Our finding are summarized below.

1) Cluster membership probabilities, P_{de}, and the retrieved luminosity function of the A569 cluster core depend on the luminosity function of the model. This problem can be overcome by iterative procedures.

2) For our field of view cluster membership is hard to assess for individual galaxies, at least at $M_R >$-19, but can be achieved in a statistical sense through the use of P_{de} which have individual errors of about 0.09 (member=1, non-member=0).

3) The luminosity function is retrieved for 41 statistical members of the A569 core. A Schecter function fit results in α=1.25±0.11 and M^*=22.8±1.3. The value of α is similar to the values found for nearby galaxy groups (Trentham and Tully, 2009) as well as the Virgo and A2199 clusters (Rines and Geller, 2008), but Lieder et al. (in press) finds a steeper luminosity function of the Virgo cluster core.

4) Our toy model suggests that α will not change significantly due to galaxy infall and mergers.

5) The model predictions are consistent with the observed distribution of galaxy interactions below M_R=-21, but not at higher luminosities. The lack of interaction signatures observed in the two most massive cluster members could indicate that most galaxy orbits are not random and avoid the cluster center, or that most of the interaction signatures are caused by close encounters and not mergers.
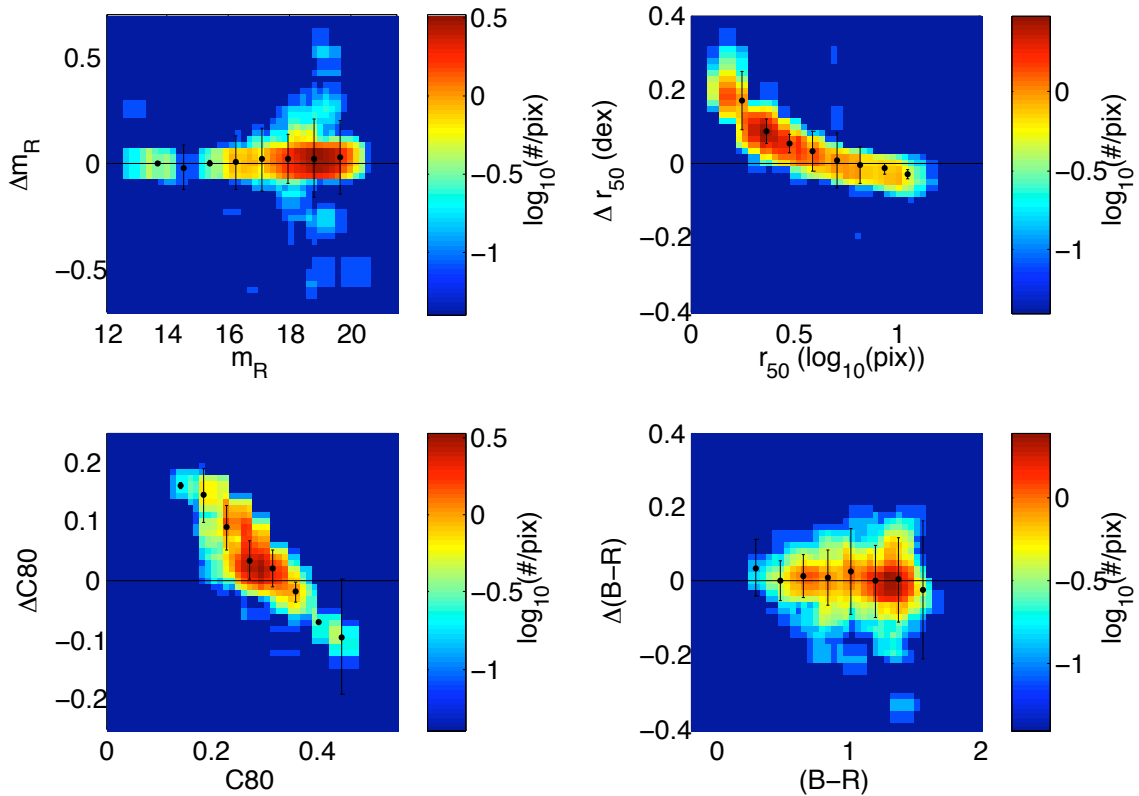
Figure 4.12: Comparison between model galaxy properties in terms of m_R (top left), r_{50} (top right), $C80$ (bottom left) and $(B - R)$ (bottom right) as inserted in the model images, and those recovered by SourceExtractor (Δ = inserted-retrieved). The plots are color coded by density and the density map have been convolved with an 5x5 pixel average filter.

from the International Max Planck Research School in Heidelberg.

4.11 APPENDIX

4.11.1 Quality of observed parameters

Figure 4.12 shows a comparison between input parameters for the model galaxies in the model images and the parameters retrieved using SourceExtractor. Errors associated with object detection and deblending cause a considerable scatter. The input $C80$ values cluster strongly around $C80 \sim 0.25$ since most galaxies are disks with exponential light profiles. The output $C80$ values do on the other hand scatter a lot more, this can be explained by the 2σ detection threshold which cut faint outer structures. $C80$ may thus not be a good indicator of the intrinsic light profile, but can still aid in the membership determination (see Sec. 4.5). r_{50} is recovered with an accuracy of about 11% for all except the smallest sources where again the detection threshold plays a role.

Chapter 5   Conclusions and outlook

Probing the stellar content of galaxies

In chapter 2 we saw that commonly used stellar population models differ in their prediction of u,g,r,i,z-band photometry (see Fig. 2.4 and 2.5) and we would therefore like to emphasize the importance of the choice of model. Once an adequate range of star formation histories, chemical enrichments and dust extinctions are considered the Bruzual and Charlot (2003) model performs well in reproducing colors of galaxies in the local Universe. Our rather simple treatment of dust that couples the amount of extinction to a galaxy's stellar population, suggests that extinction in galaxies can be probed by optical colors although some degeneracies are present (Fig. 2.9). Moreover, all models we tested in chapter 2 display rather orthogonal dependence of stellar population age and metallicity in (g-r) versus (i-z) (Fig. 2.7 and 2.8). These results are exciting, can we learn almost everything about a galaxy's stellar population from optical imaging? More work is needed before we can say to what degree this is true. However, our modelling of stellar population properties using broad band colors was shown to agree reasonably well with results based on spectra (Fig. 2.12 and 2.13). The method thus stands as a viable option for probing the stellar content of galaxies, particularly useful when spectroscopic measurements are hard to obtain like in the case of galaxy outskirts, or low mass galaxies in general. However, currently available stellar population models struggle to reproduce the photometry of both star forming and quiescent low mass galaxies. An improvement of the models will be important for future work, especially since spectroscopic measurements are extremely difficult for unresolved low surface brightness galaxies.

Applying the method used in this work to galaxies at higher redshifts is not straight forward. The redshift enters as an additional parameter that changes the spectral energy distribution and will lead to further degeneracies. Through the use of additional bands in the near infra red it may be possible to overcome this issue.

What sets galaxy properties

In chapter 3 we presented how structural and stellar population properties of nearby galaxies depend on galaxy stellar mass and the environment in which the galaxies reside. Almost all properties correlate strongly with mass. More massive galaxies are on average older, more metal rich, larger, form less stars and are of earlier morphological type (Fig. 3.2). As expected, given the importance of gravity on galactic scales galaxy mass is an important driver behind galaxy formation and evolution.

Nevertheless, the mass of the group in which the galaxies reside is also shown to correlate with galaxy properties (Fig. 3.5). These correlations are in agreement with environmental processes such as ram-pressure stripping, which is expected to be more efficient in dense environments. Galaxies in more massive groups are older, less star forming and of earlier morphological type, but also more metal rich. The latter could be an indication of the fact that it is more difficult for galaxies in massive groups to acquire pristine gas. A connection between the environment and galaxy growth in the form of mergers and accretion is expected.

In Sec. 3.5.5 we found a connection between average galaxy properties of galaxies in groups and the stellar mass function at fixed galaxy mass and group mass (Fig. 3.9 and 3.7).

Groups that have more "red and dead" galaxies have a larger number of dwarfs as well as more mass in galaxies with stellar masses of $\sim 10^{10.5} M_{\odot}$ with respect to $\sim 10^{10.3} M_{\odot}$. These findings highlight the link between the environment and galaxy growth. In this context it is also worth pointing out that, if dwarfs are excluded, the typical galaxy mass will depend on the mass of the group in which the galaxies reside (Fig. 3.6). Galaxies in more massive groups are more massive, a property which influences any apparent correlation between galaxy properties and environment.

To summarize galaxy properties are determined by the mass of the galaxy as well as by the environment in which the galaxies reside. Importantly, environment plays a role both through processes such as ram-pressure stripping, but also because the merger and accretion history will be different in various environments.

Studies similar to ours that use larger galaxy samples will shed more light on the connection between the environment and galaxy growth. The method used in this work requires spectroscopic redshifts and is therefore challenging for large galaxy samples even though some surveys will meet these requirements (see e.g. Driver et al., 2011). Alternatively, instead of focusing on larger volumes, one can instead aim to sample the stellar mass function to even lower masses in the local Universe. Such studies do not necessarily need redshifts as distances to nearby galaxies can be addressed with imaging data only.

Imaging based galaxy distances

The structure and the colors of galaxies depend on galaxy mass as we saw in chapter 3. The observed size, light profile and color will therefore say something about the distance to the source. It is therefore possible to assess distances to nearby galaxies based on imaging data, although some limitations are present as we saw in chapter 4. As discussed in Sec. 4.9 the accuracy that can be achieved depends on the distance to the source as well as the field of view through the amount of foreground and background contamination. Galaxy catalogs from semi-analytic galaxy formation models are a very valuable tool to constrain the expected distribution of galaxies along the line of sight (see also Henriques et al., 2011), and can thereby aid in the distance determination as we saw in Sec. 4.5. However, these catalogs still have some issues since certain properties of the semi-analytic galaxies are not yet in perfect agreement with observations (Guo et al., 2011). A combined effort of observers and modellers will likely reduce these discrepancies in the future. We find that the method outlined in chapter 4 can be used to assess cluster memberships in statistical sense for galaxies in the Abell 569 cluster located at a distance of 85Mpc, but that individual memberships for galaxies fainter than $M_R = -19$ are uncertain. The use of more colors can improve the method. For example in chapter 2 we saw that u,g,r,i,z-band photometry can constrain absolute magnitudes of nearby galaxies with an accuracy of about 1mag.

Interaction signatures

In chapter 4 we used deep imaging to detect several features indicative of galaxy interaction in the Abell 569 cluster core. Studies of interaction signatures can potentially reveal the frequency of galaxy mergers, also as a function of galaxy mass and environment. This kind of studies can thereby address a key aspect of galaxy formation and evolution. However, in Sec. 4.9 we saw that it is not straight forward to interpret features indicative of galaxy interactions. For example it is very hard to say whether a particular tidal tail is caused by a merger, a close encounter or the tidal field of the cluster. Sophisticated models, perhaps along the lines of Feldmann et al. (2008); Chilingarian et al. (2010a); Lotz et al. (2010), will be valuable for interpreting the frequency of interaction signatures as a function of environment. Larger observational studies that provide better statistics of the abundance of shells, tidal tails, lopsided disks, merging pairs and disturbed isophotes will impose important constraints for galaxy formation models as well as for cosmological models. Such studies have

been initiated (Martínez-Delgado et al., 2010; Duc et al., 2011) although it is desirable to survey a larger range of environments and galaxy types to get a complete picture.

Acknowledgement

First of all I would like to thank Maria Niewiem for being so nice and positive, and for always supporting me. I am grateful to Thorsten Lisker for supervising me these three years and to Eva Grebel and Jay Gallagher for useful suggestions to improve the content of this thesis.

I would like to thank the usual suspects Mauricio Cisternas, Roman Follert, Mario Gennaro, Alexander Karim, Julian Merten, Gisella De Rosa, Kasper Schmidt, Bhargav Vaidya and Ana Valente who made the stay in HD more fun. Hope to see you all again soon although you will be off to all sorts of places around the globe. I am glad to have had the opportunity to do my PhD studies within the framework of the IMPRS program. Thanks also to Sanjaya Paudel for many interesting science discussions.

The ones I did not mention so far, thanks to the Weberstraße crowd.

Moreover, I would like to express my gratitude to Ulla and Jan Anders Hansson for their support and kindness as well as for believing in me. Last of all I once again would like to thank Maria Niewiem for putting up with me during the writing of this thesis.

Bibliography

Abazajian, K. N., Adelman-McCarthy, J. K., Agüeros, M. A., Allam, S. S., Allende Prieto, C., An, D., Anderson, K. S. J., Anderson, S. F., Annis, J., Bahcall, N. A., and et al.: 2009, *ApJS* **182**, 543

Abel, T., Bryan, G. L., and Norman, M. L.: 2002, *Science* **295**, 93

Abell, G. O.: 1958, *ApJS* **3**, 211

Adami, C., Durret, F., Mazure, A., Pelló, R., Picat, J. P., West, M., and Meneux, B.: 2007, *A&A* **462**, 411

Adelman-McCarthy, J. K., Agüeros, M. A., Allam, S. S., Allende Prieto, C., Anderson, K. S. J., Anderson, S. F., Annis, J., Bahcall, N. A., Bailer-Jones, C. A. L., and Baldry, I. K. e. a.: 2008, *ApJS* **175**, 297

Adelman-McCarthy, J. K., Agüeros, M. A., Allam, S. S., Anderson, K. S. J., Anderson, S. F., Annis, J., Bahcall, N. A., Baldry, I. K., Barentine, J. C., and Berlind, A. e. a.: 2006, *ApJS* **162**, 38

Aihara, H., Allende Prieto, C., An, D., Anderson, S. F., Aubourg, É., Balbinot, E., Beers, T. C., Berlind, A. A., Bickerton, S. J., and Bizyaev, D. e. a.: 2011, *ApJS* **193**, 29

Allen, S. W., Dunn, R. J. H., Fabian, A. C., Taylor, G. B., and Reynolds, C. S.: 2006, *MNRAS* **372**, 21

Anders, P. and Fritze-v. Alvensleben, U.: 2003, *A&A* **401**, 1063

Asari, N. V., Cid Fernandes, R., Stasińska, G., Torres-Papaqui, J. P., Mateus, A., Sodré, L., Schoenell, W., and Gomes, J. M.: 2007, *MNRAS* **381**, 263

Bacon, R., Copin, Y., Monnet, G., Miller, B. W., Allington-Smith, J. R., Bureau, M., Carollo, C. M., Davies, R. L., Emsellem, E., Kuntschner, H., Peletier, R. F., Verolme, E. K., and de Zeeuw, P. T.: 2001, *MNRAS* **326**, 23

Baldry, I. K., Glazebrook, K., Brinkmann, J., Ivezić, Ž., Lupton, R. H., Nichol, R. C., and Szalay, A. S.: 2004, *ApJ* **600**, 681

Bamford, S. P., Nichol, R. C., Baldry, I. K., Land, K., Lintott, C. J., Schawinski, K., Slosar, A., Szalay, A. S., Thomas, D., Torki, M., Andreescu, D., Edmondson, E. M., Miller, C. J., Murray, P., Raddick, M. J., and Vandenberg, J.: 2009, *MNRAS* **393**, 1324

Barkhouse, W. A., Yee, H. K. C., and López-Cruz, O.: 2007, *ApJ* **671**, 1471

Bastian, N., Covey, K. R., and Meyer, M. R.: 2010, *ARA&A* **48**, 339

Bell, E. F. and de Jong, R. S.: 2001, *ApJ* **550**, 212

Bell, E. F., McIntosh, D. H., Katz, N., and Weinberg, M. D.: 2003, *ApJS* **149**, 289

Bernardi, M., Hyde, J. B., Sheth, R. K., Miller, C. J., and Nichol, R. C.: 2007, *AJ* **133**, 1741

Bertelli, G., Bressan, A., Chiosi, C., Fagotto, F., and Nasi, E.: 1994, *A&AS* **106**, 275

Bertelli, G., Girardi, L., Marigo, P., and Nasi, E.: 2008, *A&A* **484**, 815

Bertin, E. and Arnouts, S.: 1996, *A&AS* **117**, 393

Binggeli, B., Sandage, A., and Tammann, G. A.: 1985, *AJ* **90**, 1681

Binney, J.: 1985, *MNRAS* **212**, 767

Blanton, M. R., Kazin, E., Muna, D., Weaver, B. A., and Price-Whelan, A.: 2011, *AJ* **142**, 31

Blanton, M. R. and Roweis, S.: 2007, *AJ* **133**, 734

Blanton, M. R., Schlegel, D. J., Strauss, M. A., Brinkmann, J., Finkbeiner, D., Fukugita, M., Gunn, J. E., Hogg, D. W., Ivezić, Ž., Knapp, G. R., Lupton, R. H., Munn, J. A., Schneider, D. P., Tegmark, M., and Zehavi, I.: 2005, *AJ* **129**, 2562

Bolzonella, M., Miralles, J.-M., and Pelló, R.: 2000, *A&A* **363**, 476

Boselli, A., Boissier, S., Cortese, L., and Gavazzi, G.: 2008, *ApJ* **674**, 742

Bower, R. G., Benson, A. J., Malbon, R., Helly, J. C., Frenk, C. S., Baugh, C. M., Cole, S., and Lacey, C. G.: 2006, *MNRAS* **370**, 645

Boylan-Kolchin, M., Springel, V., White, S. D. M., Jenkins, A., and Lemson, G.: 2009, *MNRAS* **398**, 1150

Brinchmann, J., Charlot, S., White, S. D. M., Tremonti, C., Kauffmann, G., Heckman, T., and Brinkmann, J.: 2004, *MNRAS* **351**, 1151

Bruzual, G. and Charlot, S.: 2003, *MNRAS* **344**, 1000

Cardelli, J. A., Clayton, G. C., and Mathis, J. S.: 1989, *ApJ* **345**, 245

Cassisi, S., Castellani, V., Ciarcelluti, P., Piotto, G., and Zoccali, M.: 2000, *MNRAS* **315**, 679

Cava, A., Bettoni, D., Poggianti, B. M., Couch, W. J., Moles, M., Varela, J., Biviano, A., D'Onofrio, M., Dressler, A., Fasano, G., Fritz, J., Kjærgaard, P., Ramella, M., and Valentinuzzi, T.: 2009, *A&A* **495**, 707

Chabrier, G.: 2003, *PASP* **115**, 763

Charlot, S. and Bruzual, A. G.: 1991, *ApJ* **367**, 126

Charlot, S. and Fall, S. M.: 2000, *ApJ* **539**, 718

Chiboucas, K., Karachentsev, I. D., and Tully, R. B.: 2009, *AJ* **137**, 3009

Chilingarian, I., Prugniel, P., Sil'Chenko, O., and Koleva, M.: 2007, in A. Vazdekis & R. F. Peletier (ed.), *IAU Symposium*, Vol. 241 of *IAU Symposium*, pp 175–176

Chilingarian, I. V., Di Matteo, P., Combes, F., Melchior, A.-L., and Semelin, B.: 2010a, *A&A* **518**, A61

Chilingarian, I. V., Melchior, A., and Zolotukhin, I. Y.: 2010b, *MNRAS* **405**, 1409

Chung, A., van Gorkom, J. H., Kenney, J. D. P., Crowl, H., and Vollmer, B.: 2009, *AJ* **138**, 1741

Chung, A., van Gorkom, J. H., Kenney, J. D. P., and Vollmer, B.: 2007, *ApJ* **659**, L115

Cid Fernandes, R., Mateus, A., Sodré, L., Stasińska, G., and Gomes, J. M.: 2005, *MNRAS* **358**, 363

Conroy, C. and Gunn, J. E.: 2010, *ApJ* **712**, 833

Conroy, C., Gunn, J. E., and White, M.: 2009, *ApJ* **699**, 486

Conroy, C., White, M., and Gunn, J. E.: 2010, *ApJ* **708**, 58

Croton, D. J., Farrar, G. R., Norberg, P., Colless, M., Peacock, J. A., Baldry, I. K., Baugh, C. M., Bland-Hawthorn, J., Bridges, T., Cannon, R., Cole, S., Collins, C., and Couch, W.: 2005, *MNRAS* **356**, 1155

Csabai, I., Budavári, T., Connolly, A. J., Szalay, A. S., Győry, Z., Benítez, N., Annis, J., Brinkmann, J., Eisenstein, D., Fukugita, M., Gunn, J., Kent, S., Lupton, R., Nichol, R. C., and Stoughton, C.: 2003, *AJ* **125**, 580

Cypriano, E. S., Mendes de Oliveira, C. L., and Sodré, Jr., L.: 2006, *AJ* **132**, 514

da Cunha, E., Charlot, S., and Elbaz, D.: 2008, *MNRAS* **388**, 1595

da Cunha, E., Eminian, C., Charlot, S., and Blaizot, J.: 2010, *MNRAS* **403**, 1894

Dale, D. A., Giovanelli, R., Haynes, M. P., Scodeggio, M., Hardy, E., and Campusano, L. E.: 1997, *AJ* **114**, 455

De Lucia, G. and Blaizot, J.: 2007, *MNRAS* **375**, 2

De Lucia, G., Springel, V., White, S. D. M., Croton, D., and Kauffmann, G.: 2006, *MNRAS* **366**, 499

Di Matteo, P., Combes, F., Melchior, A.-L., and Semelin, B.: 2007, *A&A* **468**, 61

Doi, M., Tanaka, M., Fukugita, M., Gunn, J. E., Yasuda, N., Ivezić, Ž., Brinkmann, J., de Haars, E., Kleinman, S. J., Krzesinski, J., and French Leger, R.: 2010, *AJ* **139**, 1628

D'Onghia, E., Sommer-Larsen, J., Romeo, A. D., Burkert, A., Pedersen, K., Portinari, L., and Rasmussen, J.: 2005, *ApJ* **630**, L109

Dressler, A.: 1980, *ApJ* **236**, 351

Driver, S. P., Hill, D. T., Kelvin, L. S., Robotham, A. S. G., Liske, J., Norberg, P., Baldry, I. K., Bamford, S. P., Hopkins, A. M., Loveday, J., Peacock, J. A., Andrae, E., Bland-Hawthorn, J., Brough, S., Brown, M. J. I., Cameron, E., Ching, J. H. Y., Colless, M., Conselice, C. J., Croom, S. M., Cross, N. J. G., de Propris, R., Dye, S., Drinkwater, M. J., Ellis, S., Graham, A. W., Grootes, M. W., Gunawardhana, M., Jones, D. H., van Kampen, E., Maraston, C., Nichol, R. C., Parkinson, H. R., Phillipps, S., Pimbblet, K., Popescu, C. C., Prescott, M., Roseboom, I. G., Sadler, E. M., Sansom, A. E., Sharp, R. G., Smith, D. J. B., Taylor, E., Thomas, D., Tuffs, R. J., Wijesinghe, D., Dunne, L., Frenk, C. S., Jarvis, M. J., Madore, B. F., Meyer, M. J., Seibert, M., Staveley-Smith, L., Sutherland, W. J., and Warren, S. J.: 2011, *MNRAS* **413**, 971

Duc, P.-A., Cuillandre, J.-C., Serra, P., Michel-Dansac, L., Ferriere, E., Alatalo, K., Blitz, L., Bois, M., Bournaud, F., Bureau, M., Cappellari, M., Davies, R. L., Davis, T. A., de Zeeuw, P. T., Emsellem, E., Khochfar, S., Krajnović, D., Kuntschner, H., Lablanche, P.-Y., McDermid, R. M., Morganti, R., Naab, T., Oosterloo, T., Sarzi, M., Scott, N., Weijmans, A.-M., and Young, L. M.: 2011, *MNRAS* **417**, 863

Ellison, S. L., Patton, D. R., Simard, L., McConnachie, A. W., Baldry, I. K., and Mendel, J. T.: 2010, *MNRAS* **407**, 1514

Emsellem, E., Cappellari, M., Krajnović, D., van de Ven, G., Bacon, R., Bureau, M., Davies, R. L., de Zeeuw, P. T., Falcón-Barroso, J., Kuntschner, H., McDermid, R., Peletier, R. F., and Sarzi, M.: 2007, *MNRAS* **379**, 401

Engelbracht, C. W., Rieke, G. H., Gordon, K. D., Smith, J., Werner, M. W., Moustakas, J., Willmer, C. N. A., and Vanzi, L.: 2008, *ApJ* **678**, 804

Fakhouri, O. and Ma, C.-P.: 2009, *MNRAS* **394**, 1825

Fall, S. M. and Efstathiou, G.: 1980, *MNRAS* **193**, 189

Fan, X., Carilli, C. L., and Keating, B.: 2006, *ARA&A* **44**, 415

Fang, F. and Saslaw, W. C.: 1997, *ApJ* **476**, 534

Feast, M. W. and Catchpole, R. M.: 1997, *MNRAS* **286**, L1

Feldmann, R., Mayer, L., and Carollo, C. M.: 2008, *ApJ* **684**, 1062

Gallazzi, A., Charlot, S., Brinchmann, J., White, S. D. M., and Tremonti, C. A.: 2005, *MNRAS* **362**, 41

Gavazzi, G., Bonfanti, C., Sanvito, G., Boselli, A., and Scodeggio, M.: 2002, *ApJ* **576**, 135

Gavazzi, G., Boselli, A., Mayer, L., Iglesias-Paramo, J., Vílchez, J. M., and Carrasco, L.: 2001, *ApJ* **563**, L23

Girardi, L., Bressan, A., Bertelli, G., and Chiosi, C.: 2000, *A&AS* **141**, 371

González Delgado, R. M. and Cid Fernandes, R.: 2010, *MNRAS* **403**, 797

González-Lópezlira, R. A., Bruzual-A., G., Charlot, S., Ballesteros-Paredes, J., and Loinard, L.: 2010, *MNRAS* **403**, 1213

Governato, F., Brook, C., Mayer, L., Brooks, A., Rhee, G., Wadsley, J., Jonsson, P., Willman, B., Stinson, G., Quinn, T., and Madau, P.: 2010, *Nature* **463**, 203

Graham, A. W. and Driver, S. P.: 2005, **22**, 118

Graham, A. W. and Guzmán, R.: 2003, *AJ* **125**, 2936

Graham, A. W. and Worley, C. C.: 2008, *MNRAS* **388**, 1708

Gunn, J. E., Carr, M., Rockosi, C., Sekiguchi, M., Berry, K., Elms, B., de Haas, E., Ivezić, Ž., Knapp, G., Lupton, R., Pauls, G., Simcoe, R., Hirsch, R., Sanford, D., Wang, S., York, D., Harris, F., Annis, J., Bartozek, L., Boroski, W., Bakken, J., Haldeman, M., Kent, S., Holm, S., Holmgren, D., Petravick, D., Prosapio, A., Rechenmacher, R., Doi, M., Fukugita, M., Shimasaku, K., Okada, N., Hull, C., Siegmund, W., Mannery, E., Blouke, M., Heidtman, D., Schneider, D., Lucinio, R., and Brinkman, J.: 1998, *AJ* **116**, 3040

Gunn, J. E. and Gott, III, J. R.: 1972, *ApJ* **176**, 1

Gunn, J. E., Siegmund, W. A., Mannery, E. J., Owen, R. E., Hull, C. L., Leger, R. F., Carey, L. N., Knapp, G. R., York, D. G., Boroski, W. N., Kent, S. M., Lupton, R. H., Rockosi, C. M., Evans, M. L., Waddell, P., Anderson, J. E., Annis, J., Barentine, J. C., Bartoszek, L. M., Bastian, S., Bracker, S. B., Brewington, H. J., Briegel, C. I., Brinkmann, J., Brown, Y. J., Carr, M. A., Czarapata, P. C., Drennan, C. C., Dombeck, T., Federwitz, G. R., Gillespie, B. A., Gonzales, C., Hansen, S. U., Harvanek, M., Hayes, J., Jordan, W., Kinney, E., Klaene, M., Kleinman, S. J., Kron, R. G., Kresinski, J., Lee, G., Limmongkol, S., Lindenmeyer, C. W., Long, D. C., Loomis, C. L., McGehee, P. M., Mantsch, P. M., Neilsen, Jr., E. H., Neswold, R. M., Newman, P. R., Nitta, A., Peoples, Jr., J., Pier, J. R., Prieto, P. S., Prosapio, A., Rivetta, C., Schneider, D. P., Snedden, S., and Wang, S.-i.: 2006, *AJ* **131**, 2332

Guo, Q., White, S., Boylan-Kolchin, M., De Lucia, G., Kauffmann, G., Lemson, G., Li, C., Springel, V., and Weinmann, S.: 2011, *MNRAS* **413**, 101

Guo, Q., White, S., Li, C., and Boylan-Kolchin, M.: 2010, *MNRAS* **404**, 1111

Győry, Z., Szalay, A. S., Budavári, T., Csabai, I., and Charlot, S.: 2011, *AJ* **141**, 133

Häring, N. and Rix, H.-W.: 2004, *ApJ* **604**, L89

Heavens, A., Panter, B., Jimenez, R., and Dunlop, J.: 2004, *Nature* **428**, 625

Henriques, B., White, S., Lemson, G., Thomas, P., Guo, Q., Marleau, G.-D., and Overzier, R.: 2011, *ArXiv e-prints*

Hubble, E.: 1929, *Proceedings of the National Academy of Science* **15**, 168

Huchra, J. P. and Geller, M. J.: 1982, *ApJ* **257**, 423

Iliev, I. T., Moore, B., Gottlöber, S., Yepes, G., Hoffman, Y., and Mellema, G.: 2011, *MNRAS* **413**, 2093

Janz, J. and Lisker, T.: 2008, *ApJ* **689**, L25

Janz, J. and Lisker, T.: 2009a, *Astronomische Nachrichten* **330**, 948

Janz, J. and Lisker, T.: 2009b, *ApJ* **696**, L102

Kannappan, S. J.: 2004, *ApJ* **611**, L89

Kannappan, S. J., Guie, J. M., and Baker, A. J.: 2009, *AJ* **138**, 579

Kauffmann, G., Heckman, T. M., White, S. D. M., Charlot, S., Tremonti, C., Brinchmann, J., Bruzual, G., Peng, E. W., Seibert, M., Bernardi, M., and Blanton, M.: 2003a, *MNRAS* **341**, 33

Kauffmann, G., Heckman, T. M., White, S. D. M., Charlot, S., Tremonti, C., Peng, E. W., Seibert, M., Brinkmann, J., Nichol, R. C., SubbaRao, M., and York, D.: 2003b, *MNRAS* **341**, 54

Kauffmann, G., White, S. D. M., Heckman, T. M., Ménard, B., Brinchmann, J., Charlot, S., Tremonti, C., and Brinkmann, J.: 2004, *MNRAS* **353**, 713

Kenney, J. D. P., van Gorkom, J. H., and Vollmer, B.: 2004, *AJ* **127**, 3361

Kennicutt, Jr., R. C.: 1998, *ApJ* **498**, 541

Kent, S. M.: 1985, *ApJS* **59**, 115

Kereš, D., Katz, N., Weinberg, D. H., and Davé, R.: 2005, *MNRAS* **363**, 2

Knox, R. A., Hambly, N. C., Hawkins, M. R. S., and MacGillivray, H. T.: 1998, *MNRAS* **297**, 839

Koleva, M., Prugniel, P., Bouchard, A., and Wu, Y.: 2009, *A&A* **501**, 1269

Komatsu, E., Smith, K. M., Dunkley, J., Bennett, C. L., Gold, B., Hinshaw, G., Jarosik, N., Larson, D., Nolta, M. R., Page, L., Spergel, D. N., Halpern, M., Hill, R. S., Kogut, A., Limon, M., Meyer, S. S., Odegard, N., Tucker, G. S., Weiland, J. L., Wollack, E., and Wright, E. L.: 2011, *ApJS* **192**, 18

Kormendy, J.: 1985, *ApJ* **295**, 73

Kotulla, R., Fritze, U., Weilbacher, P., and Anders, P.: 2009, *MNRAS* **396**, 462

Kron, R. G.: 1980, *ApJS* **43**, 305

Kroupa, P.: 2001, *MNRAS* **322**, 231

Kroupa, P., Tout, C. A., and Gilmore, G.: 1993, *MNRAS* **262**, 545

Larson, R. B.: 1974, *MNRAS* **169**, 229

Larson, R. B.: 1976, *MNRAS* **176**, 31

Larson, R. B., Tinsley, B. M., and Caldwell, C. N.: 1980, *ApJ* **237**, 692

Lauer, T. R., Faber, S. M., Richstone, D., Gebhardt, K., Tremaine, S., Postman, M., Dressler, A., Aller, M. C., Filippenko, A. V., Green, R., Ho, L. C., Kormendy, J., Magorrian, J., and Pinkney, J.: 2007, *ApJ* **662**, 808

Le Borgne, J., Bruzual, G., Pelló, R., Lançon, A., Rocca-Volmerange, B., Sanahuja, B., Schaerer, D., Soubiran, C., and Vílchez-Gómez, R.: 2003, *A&A* **402**, 433

Lee, J. C., Kennicutt, R. C., José G. Funes, S. J., Sakai, S., and Akiyama, S.: 2009, *ApJ* **692**, 1305

Leitherer, C., Schaerer, D., Goldader, J. D., González Delgado, R. M., Robert, C., Kune, D. F., de Mello, D. F., Devost, D., and Heckman, T. M.: 1999, *ApJS* **123**, 3

Lejeune, T., Cuisinier, F., and Buser, R.: 1997, *A&AS* **125**, 229

Lemaître, G.: 1927, *Annales de la Societe Scietifique de Bruxelles* **47**, 49

Lin, L., Cooper, M. C., Jian, H.-Y., Koo, D. C., Patton, D. R., Yan, R., Willmer, C. N. A., Coil, A. L., Chiueh, T., Croton, D. J., Gerke, B. F., Lotz, J., Guhathakurta, P., and Newman, J. A.: 2010, *ApJ* **718**, 1158

Lintott, C., Schawinski, K., Bamford, S., Slosar, A., Land, K., Thomas, D., Edmondson, E., Masters, K., Nichol, R. C., Raddick, M. J., Szalay, A., Andreescu, D., Murray, P., and Vandenberg, J.: 2011, *MNRAS* **410**, 166

Lintott, C. J., Schawinski, K., Slosar, A., Land, K., Bamford, S., Thomas, D., Raddick, M. J., Nichol, R. C., Szalay, A., Andreescu, D., Murray, P., and Vandenberg, J.: 2008, *MNRAS* **389**, 1179

Lisker, T., Glatt, K., Westera, P., and Grebel, E. K.: 2006, *AJ* **132**, 2432

Lisker, T., Grebel, E. K., and Binggeli, B.: 2008, *AJ* **135**, 380

Lisker, T., Grebel, E. K., Binggeli, B., and Glatt, K.: 2007, *ApJ* **660**, 1186

Lisker, T., Janz, J., Hensler, G., Kim, S., Rey, S.-C., Weinmann, S., Mastropietro, C., Hielscher, O., Paudel, S., and Kotulla, R.: 2009, *ApJ* **706**, L124

Lotz, J. M., Jonsson, P., Cox, T. J., and Primack, J. R.: 2010, *MNRAS* **404**, 575

Makarov, D. and Karachentsev, I.: 2011, *MNRAS* **412**, 2498

Makino, J. and Hut, P.: 1997, *ApJ* **481**, 83

Malin, D. F. and Carter, D.: 1983, *ApJ* **274**, 534

Maraston, C.: 2005, *MNRAS* **362**, 799

Marconi, M., Musella, I., and Fiorentino, G.: 2005, *ApJ* **632**, 590

Marigo, P. and Girardi, L.: 2007, *A&A* **469**, 239

Marigo, P., Girardi, L., Bressan, A., Groenewegen, M. A. T., Silva, L., and Granato, G. L.: 2008, *A&A* **482**, 883

Martig, M., Bournaud, F., Teyssier, R., and Dekel, A.: 2009, *ApJ* **707**, 250

Martínez-Delgado, D., Gabany, R. J., Crawford, K., Zibetti, S., Majewski, S. R., Rix, H.-W., Fliri, J., Carballo-Bello, J. A., Bardalez-Gagliuffi, D. C., and Peñarrubia, J. e. a.: 2010, *AJ* **140**, 962

Masters, K. L., Nichol, R., Bamford, S., Mosleh, M., Lintott, C. J., Andreescu, D., Edmondson, E. M., Keel, W. C., Murray, P., Raddick, M. J., Schawinski, K., Slosar, A., Szalay, A. S., Thomas, D., and Vandenberg, J.: 2010, *MNRAS* pp 459–+

Mastropietro, C., Moore, B., Mayer, L., Debattista, V. P., Piffaretti, R., and Stadel, J.: 2005, *MNRAS* **364**, 607

Mayer, L., Governato, F., Colpi, M., Moore, B., Quinn, T., Wadsley, J., Stadel, J., and Lake, G.: 2001, *ApJ* **559**, 754

Mieske, S., Hilker, M., Infante, L., and Mendes de Oliveira, C.: 2007, *A&A* **463**, 503

Misgeld, I. and Hilker, M.: 2011, *MNRAS* **414**, 3699

Misgeld, I., Hilker, M., and Mieske, S.: 2009, *A&A* **496**, 683

Misgeld, I., Mieske, S., and Hilker, M.: 2008, *A&A* **486**, 697

Monet, D.: 1998, *USNO-A2.0*, Monet, D.

Monet, D., Canzian, B., Harris, H., Reid, N., Rhodes, A., and Sell, S.: 1998, *VizieR Online Data Catalog* **1243**, 0

Montero-Dorta, A. D. and Prada, F.: 2009, *MNRAS* **399**, 1106

Moore, B., Katz, N., Lake, G., Dressler, A., and Oemler, A.: 1996, *Nature* **379**, 613

Moore, B., Lake, G., and Katz, N.: 1998, *ApJ* **495**, 139

Moster, B. P., Somerville, R. S., Maulbetsch, C., van den Bosch, F. C., Macciò, A. V., Naab, T., and Oser, L.: 2010, *ApJ* **710**, 903

Nagashima, M., Yahagi, H., Enoki, M., Yoshii, Y., and Gouda, N.: 2005, *ApJ* **634**, 26

Nelan, J. E., Smith, R. J., Hudson, M. J., Wegner, G. A., Lucey, J. R., Moore, S. A. W., Quinney, S. J., and Suntzeff, N. B.: 2005, *ApJ* **632**, 137

Padilla, N. D. and Strauss, M. A.: 2008, *MNRAS* **388**, 1321

Panter, B., Jimenez, R., Heavens, A. F., and Charlot, S.: 2007, *MNRAS* **378**, 1550

Panter, B., Jimenez, R., Heavens, A. F., and Charlot, S.: 2008, *MNRAS* **391**, 1117

Park, C., Choi, Y.-Y., Vogeley, M. S., Gott, III, J. R., and Blanton, M. R.: 2007, *ApJ* **658**, 898

Paturel, G., Petit, C., Prugniel, P., Theureau, G., Rousseau, J., Brouty, M., Dubois, P., and Cambrésy, L.: 2003, *A&A* **412**, 45

Penny, S. J. and Conselice, C. J.: 2008, *MNRAS* **383**, 247

Penny, S. J., Conselice, C. J., de Rijcke, S., and Held, E. V.: 2009, *MNRAS* **393**, 1054

Petrosian, V.: 1976, *ApJ* **209**, L1

Popescu, C. C., Tuffs, R. J., Dopita, M. A., Fischera, J., Kylafis, N. D., and Madore, B. F.: 2011, *A&A* **527**, A109+

Rines, K. and Geller, M. J.: 2008, *AJ* **135**, 1837

Roediger, E. and Hensler, G.: 2005, *A&A* **433**, 875

Rudnick, G., Rix, H.-W., and Kennicutt, Jr., R. C.: 2000, *ApJ* **538**, 569

Salim, S., Rich, R. M., Charlot, S., Brinchmann, J., Johnson, B. D., Schiminovich, D., Seibert, M., Mallery, R., Heckman, T. M., and Forster, K. e. a.: 2007, *ApJS* **173**, 267

Salpeter, E. E.: 1955, *ApJ* **121**, 161

Sánchez-Janssen, R., Méndez-Abreu, J., and Aguerri, J. A. L.: 2010, *MNRAS* **406**, L65

Sandage, A.: 1986, *A&A* **161**, 89

Schäfer, B. M.: 2009, *International Journal of Modern Physics D* **18**, 173

Schaller, G., Schaerer, D., Meynet, G., and Maeder, A.: 1992, *A&AS* **96**, 269

Schechter, P.: 1976, *ApJ* **203**, 297

Schlegel, D. J., Finkbeiner, D. P., and Davis, M.: 1998, *ApJ* **500**, 525

Searle, L., Sargent, W. L. W., and Bagnuolo, W. G.: 1973, *ApJ* **179**, 427

Sersic, J. L.: 1968, *Atlas de galaxias australes*, Sersic, J. L.

Smith, R., Davies, J. I., and Nelson, A. H.: 2010a, *MNRAS* **405**, 1723

Smith, R. J., Lucey, J. R., Hammer, D., Hornschemeier, A. E., Carter, D., Hudson, M. J., Marzke, R. O., Mouhcine, M., Eftekharzadeh, S., James, P., Khosroshahi, H., Kourkchi, E., and Karick, A.: 2010b, *MNRAS* **408**, 1417

Smith, R. J., Lucey, J. R., Price, J., Hudson, M. J., and Phillipps, S.: 2011, *ArXiv e-prints*

Smolčić, V., Schinnerer, E., Finoguenov, A., Sakelliou, I., Carilli, C. L., Botzler, C. S., Brusa, M., Scoville, N., Ajiki, M., Capak, P., Guzzo, L., Hasinger, G., Impey, C., Jahnke, K., Kartaltepe, J. S., McCracken, H. J., Mobasher, B., Murayama, T., Sasaki, S. S., Shioya, Y., Taniguchi, Y., and Trump, J. R.: 2007, *ApJS* **172**, 295

Snaith, O. N., Gibson, B. K., Brook, C. B., Courty, S., Sánchez-Blázquez, P., Kawata, D., Knebe, A., and Sales, L. V.: 2011, *MNRAS* **415**, 2798

Spergel, D. N., Verde, L., Peiris, H. V., Komatsu, E., Nolta, M. R., Bennett, C. L., Halpern, M., Hinshaw, G., Jarosik, N., Kogut, A., Limon, M., Meyer, S. S., Page, L., Tucker, G. S., Weiland, J. L., Wollack, E., and Wright, E. L.: 2003, *ApJS* **148**, 175

Spiniello, C., Koopmans, L. V. E., Trager, S. C., Czoske, O., and Treu, T.: 2011, *arXive:1103.4773*

Springel, V., White, S. D. M., Jenkins, A., Frenk, C. S., Yoshida, N., Gao, L., Navarro, J., Thacker, R., Croton, D., Helly, J., Peacock, J. A., Cole, S., Thomas, P., Couchman, H., Evrard, A., Colberg, J., and Pearce, F.: 2005, *Nature* **435**, 629

Stoughton, C., Lupton, R. H., Bernardi, M., Blanton, M. R., Burles, S., Castander, F. J., Connolly, A. J., Eisenstein, D. J., Frieman, J. A., Hennessy, G. S., Hindsley, R. B., Ivezić, Ž., Kent, S., Kunszt, P. Z., Lee, B. C., Meiksin, A., Munn, J. A., and Newberg, H. J.: 2002, *AJ* **123**, 485

Strauss, M. A., Weinberg, D. H., Lupton, R. H., Narayanan, V. K., Annis, J., Bernardi, M., Blanton, M., Burles, S., Connolly, A. J., Dalcanton, J., Doi, M., Eisenstein, D., Frieman, J. A., Fukugita, M., Gunn, J. E., Ivezić, Ž., Kent, S., Kim, R. S. J., Knapp, G. R., Kron, R. G., Munn, J. A., Newberg, H. J., Nichol, R. C., Okamura, S., Quinn, T. R., Richmond, M. W., Schlegel, D. J., Shimasaku, K., SubbaRao, M., Szalay, A. S., Vanden Berk, D., Vogeley, M. S., Yanny, B., Yasuda, N., York, D. G., and Zehavi, I.: 2002, *AJ* **124**, 1810

Struble, M. F. and Rood, H. J.: 1999, *ApJS* **125**, 35

Sun, M., Donahue, M., and Voit, G. M.: 2007, *ApJ* **671**, 190

Szalay, A. S., Gray, J., Thakar, A. R., Kunszt, P. Z., Malik, T., Raddick, J., Stoughton, C., and vandenBerg, J.: 2002, *eprint arXiv:cs/0202013*

Tal, T., van Dokkum, P. G., Nelan, J., and Bezanson, R.: 2009, *AJ* **138**, 1417

Thomas, D., Maraston, C., and Bender, R.: 2003, *MNRAS* **339**, 897

Tinsley, B. M.: 1968, *ApJ* **151**, 547

Tovmassian, H. M. and Plionis, M.: 2009, *ApJ* **696**, 1441

Tremonti, C. A., Heckman, T. M., Kauffmann, G., Brinchmann, J., Charlot, S., White, S. D. M., Seibert, M., Peng, E. W., Schlegel, D. J., Uomoto, A., Fukugita, M., and Brinkmann, J.: 2004, *ApJ* **613**, 898

Trentham, N. and Tully, R. B.: 2002, *MNRAS* **335**, 712

Trentham, N. and Tully, R. B.: 2009, *MNRAS* **398**, 722

Trentham, N., Tully, R. B., and Mahdavi, A.: 2006, *MNRAS* **369**, 1375

Trentham, N., Tully, R. B., and Verheijen, M. A. W.: 2001, *MNRAS* **325**, 385

Tuffs, R. J., Popescu, C. C., Völk, H. J., Kylafis, N. D., and Dopita, M. A.: 2004, *A&A* **419**, 821

Tully, R. B.: 1987, *ApJ* **321**, 280

Tully, R. B. and Fisher, J. R.: 1977, *A&A* **54**, 661

Tully, R. B., Shaya, E. J., Karachentsev, I. D., Courtois, H. M., Kocevski, D. D., Rizzi, L., and Peel, A.: 2008, *ApJ* **676**, 184

Tully, R. B., Somerville, R. S., Trentham, N., and Verheijen, M. A. W.: 2002, *ApJ* **569**, 573

Tully, R. B. and Trentham, N.: 2008, *AJ* **135**, 1488

van Dokkum, P. G.: 2005, *AJ* **130**, 2647

van Dokkum, P. G. and Conroy, C.: 2010, *Nature* **468**, 940

van Dokkum, P. G. and Conroy, C.: 2011, *ApJ* **735**, L13+

van Dokkum, P. G., Franx, M., Fabricant, D., Kelson, D. D., and Illingworth, G. D.: 1999, *ApJ* **520**, L95

Vázquez, G. A. and Leitherer, C.: 2005, *ApJ* **621**, 695

Visvanathan, N. and Sandage, A.: 1977, *ApJ* **216**, 214

Walter, F., Brinks, E., de Blok, W. J. G., Bigiel, F., Kennicutt, Jr., R. C., Thornley, M. D., and Leroy, A.: 2008, *AJ* **136**, 2563

Weinmann, S. M., Lisker, T., Guo, Q., Meyer, H. T., and Janz, J.: 2011, *MNRAS* **416**, 1197

Weinmann, S. M., van den Bosch, F. C., Yang, X., and Mo, H. J.: 2006, *MNRAS* **366**, 2

Willman, B., Dalcanton, J. J., Martinez-Delgado, D., West, A. A., Blanton, M. R., Hogg, D. W., Barentine, J. C., Brewington, H. J., Harvanek, M., Kleinman, S. J., Krzesinski, J., Long, D., Neilsen, Jr., E. H., Nitta, A., and Snedden, S. A.: 2005, *ApJ* **626**, L85

Worthey, G.: 1994, *ApJS* **95**, 107

Wright, E. L.: 2006, *PASP* **118**, 1711

Yang, X., Mo, H. J., and van den Bosch, F. C.: 2009, *ApJ* **695**, 900

Yang, X., Mo, H. J., van den Bosch, F. C., Pasquali, A., Li, C., and Barden, M.: 2007, *ApJ* **671**, 153

Yates, R. M., Kauffmann, G., and Guo, Q.: 2011, *ArXiv e-prints*

York, D. G., Adelman, J., Anderson, Jr., J. E., Anderson, S. F., Annis, J., Bahcall, N. A., Bakken, J. A., Barkhouser, R., Bastian, S., Berman, E., Boroski, W. N., Bracker, S., Briegel, C., Briggs, J. W., Brinkmann, J., Brunner, R., Burles, S., Carey, L., Carr, M. A., Castander, F. J., Chen, B., Colestock, P. L., Connolly, A. J., Crocker, J. H., Csabai, I., Czarapata, P. C., Davis, J. E., Doi, M., Dombeck, T., Eisenstein, D., Ellman, N., Elms, B. R., Evans, M. L., Fan, X., Federwitz, G. R., Fiscelli, L., Friedman, S., Frieman, J. A., Fukugita, M., Gillespie, B., Gunn, J. E., Gurbani, V. K., de Haas, E., Haldeman, M., Harris, F. H., Hayes, J., Heckman, T. M., Hennessy, G. S., Hindsley, R. B., Holm, S., Holmgren, D. J., Huang, C.-h., Hull, C., Husby, D., Ichikawa, S.-I., Ichikawa, T., Ivezić, Ž., Kent, S., Kim, R. S. J., Kinney, E., Klaene, M., Kleinman, A. N., Kleinman, S.,

Knapp, G. R., Korienek, J., Kron, R. G., Kunszt, P. Z., Lamb, D. Q., Lee, B., Leger, R. F., Limmongkol, S., Lindenmeyer, C., Long, D. C., Loomis, C., Loveday, J., Lucinio, R., Lupton, R. H., MacKinnon, B., Mannery, E. J., Mantsch, P. M., Margon, B., McGehee, P., McKay, T. A., Meiksin, A., Merelli, A., Monet, D. G., Munn, J. A., Narayanan, V. K., Nash, T., Neilsen, E., Neswold, R., Newberg, H. J., Nichol, R. C., Nicinski, T., Nonino, M., Okada, N., Okamura, S., Ostriker, J. P., Owen, R., Pauls, A. G., Peoples, J., Peterson, R. L., Petravick, D., Pier, J. R., Pope, A., Pordes, R., Prosapio, A., Rechenmacher, R., Quinn, T. R., Richards, G. T., Richmond, M. W., Rivetta, C. H., Rockosi, C. M., Ruthmansdorfer, K., Sandford, D., Schlegel, D. J., Schneider, D. P., Sekiguchi, M., Sergey, G., Shimasaku, K., Siegmund, W. A., Smee, S., Smith, J. A., Snedden, S., Stone, R., Stoughton, C., Strauss, M. A., Stubbs, C., SubbaRao, M., Szalay, A. S., Szapudi, I., Szokoly, G. P., Thakar, A. R., Tremonti, C., Tucker, D. L., Uomoto, A., Vanden Berk, D., Vogeley, M. S., Waddell, P., Wang, S.-i., Watanabe, M., Weinberg, D. H., Yanny, B., and Yasuda, N.: 2000, *AJ* **120**, 1579

Zhang, W., Li, C., Kauffmann, G., Zou, H., Catinella, B., Shen, S., Guo, Q., and Chang, R.: 2009, *MNRAS* **397**, 1243

Zibetti, S., Charlot, S., and Rix, H.: 2009, *MNRAS* **400**, 1181